

# Review of single vector boson production in pp collisions at $\sqrt{s} = 7$ TeV

Matthias Schott<sup>1</sup>, Monica Dunford<sup>2</sup>

<sup>1</sup>Institut für Physik, Johannes Gutenberg Universität Mainz

<sup>2</sup>Kirchhoff Institut für Physik, Ruprecht-Karls-Universität Heidelberg

Submitted to Eur. Phys. J. C

**Abstract** This review summarises the main results on the production of single vector bosons in the Standard Model, both inclusively and in association with light- and heavy-flavour jets, at the Large Hadron Collider in proton-proton collisions at a center-of-mass energy of 7 TeV.

The general purpose detectors at this collider, ATLAS and CMS, each recorded an integrated luminosity of  $\approx 40\text{pb}^{-1}$  and  $5\text{fb}^{-1}$  in the years 2010 and 2011, respectively. The corresponding data offer the unique possibility to precisely study the properties of the production of heavy vector bosons in a new energy regime. The accurate understanding of the Standard Model is not only crucial for searches of unknown particles and phenomena but also to test predictions of perturbative Quantum-Chromodynamics calculations and for precision measurements of observables in the electroweak sector.

Results from a variety of measurements in which single  $W$  or  $Z$  bosons are identified are reviewed. Special emphasis in this review is given to interpretations of the experimental results in the context of state-of-the-art predictions.

## Contents

1	Introduction . . . . .	1
2	Vector Boson Production in the Standard Model . . . . .	3
3	Detectors and Data . . . . .	15
4	Production Cross Section Measurements at the LHC . . . . .	21
5	Event Selection and Background Estimates . . . . .	22
6	Inclusive and Differential Cross-Section Measurements . . . . .	27
7	Vector Boson Production in Association with Jets . . . . .	41
8	Summary and Outlook . . . . .	53

<sup>a</sup>e-mail: Matthias.Schott@cern.ch

<sup>b</sup>e-mail: Monica.Dunford@cern.ch

## 1 Introduction

The  $W$  and  $Z$  bosons, since their discovery at UA1 [1, 2] and UA2 [3, 4] in the early 1980s, have been the subject of detailed measurements at both electron-positron and hadron colliders. The ALEPH, DELPHI, L3 and OPAL experiments at the large electron-positron collider, LEP, performed many precision studies of these vector bosons, including measurements of the branching ratios [5], the magnetic dipole moment and the electric quadrupole moment [6], all of which were measured with a precision of better than 1%. At hadron colliders, single vector boson production has been explored at  $\sqrt{s} = 0.63$  TeV at the CERN  $S\bar{p}pS$  by UA1 and UA2, and at both  $\sqrt{s} = 1.8$  TeV and  $\sqrt{s} = 1.96$  TeV at the Tevatron by CDF [7, 8] and D0 [9, 10]. The distinct advantage of  $W$  and  $Z$  production measurements at the hadron colliders is that the number of single vector boson events is large, roughly 138,000  $Z \rightarrow ee$  and 470,000  $W \rightarrow e\nu$  candidates using 2.2  $\text{fb}^{-1}$  of data at CDF [11, 12] with relatively low background rates, roughly 0.5% of  $Z$  candidates and 1% of  $W$  candidates at CDF. The major disadvantage is that the parton center-of-mass energy can not be determined for each event because of the uncertainties in the structure of the proton. Despite these challenges, the CDF and D0 experiments have reported measurements of the mass of the  $W$  [12, 13] with a precision comparable to the measurements at LEP. In addition with the large data samples, measurements of  $W$  and  $Z$  production in association with jets [14–19] and the production of  $W$  and  $Z$  production in association with heavy flavour quarks [20–25] were performed. Measurements of single vector boson production at the  $S\bar{p}pS$  and the Tevatron have been especially important for the development of leading-order and next-to-leading order theoretical predictions, most of which are used today for comparisons to data at the Large Hadron Collider (LHC). Finally  $W$  and  $Z$  production has also been observed at heavy-ion colliders at RHIC at  $\sqrt{s} = 0.5$  TeV [26,

27] and the LHC at  $\sqrt{s} = 2.76$  TeV [28–30]. For a detailed review of the measurements performed at LEP and  $S\bar{p}pS$  see [31] and [32] respectively.

Today, the focus of measurements of  $W$  and  $Z$  production at the LHC is to test the theory of perturbative Quantum-Chromodynamics (QCD) in a new energy regime, to provide better constraints on the parton distribution functions, and to improve electroweak precision measurements, such as the mass of the  $W$  and  $\sin^2\theta$ . As  $W$  and  $Z$  production are dominant backgrounds to Higgs boson measurements and searches for physics beyond the Standard Model, these new measurements also provide insight to these studies.

For tests of the predictions of perturbative QCD, the benefit of the increase in energy at the LHC can readily be seen in Figure 1, where the Bjorken  $x$ -values of the interacting partons for a given process, e.g. the production of a  $Z$  boson, is shown. The reach in the low- $x$  region has been increased by more than two orders of magnitude compared to that of the SPS and the Tevatron. As a matter of fact, these new measurements not only benefit from the higher center-of-mass energy but also from improved statistical and systematic uncertainties. At the LHC, copious amounts of  $W$  and  $Z$  boson events, more than a million  $Z \rightarrow ee$  events at each of the ATLAS and CMS experiments during the 2011  $\sqrt{s} = 7$  TeV run, were detected, with an improved experimental precision. For example, the uncertainty on the jet energy scale is almost a factor of three better [33, 34] compared to that at the Tevatron experiments. Furthermore, the detectors have been designed to have an increased rapidity acceptance and can measure electrons for some measurements to  $|\eta| < 4.9$  and jets to  $|\eta| < 4.4$ . As a result, a large fraction of these low- $x$  events shown in Figure 1 can be reconstructed by the LHC detectors.

The theoretical predictions used for comparison to these measurements have been extended and improved. For inclusive  $W$  and  $Z$  production, theoretical predictions at next-to-next-to-leading order in perturbation theory are available. For measurements of single vector boson production in association with jets predictions at next-to-leading order for up to five additional partons in the final state exist. The magnitude of the theoretical uncertainties in these calculations are comparable to those of the experimental uncertainties. In addition several advanced leading-order predictions exist which simulate the entire event process from the hard scatter to the parton showering and the fragmentation. Although many of these predictions have been vetted by measurements at previous hadron colliders, the LHC measurements will test these predictions in previously unexplored regions of the phase space.

The structure functions of the proton, which are a dominant source of uncertainties in electroweak precision measurements at hadron colliders, can also be constrained through studies of the differential cross-sections of  $W$  or  $Z$  bosons

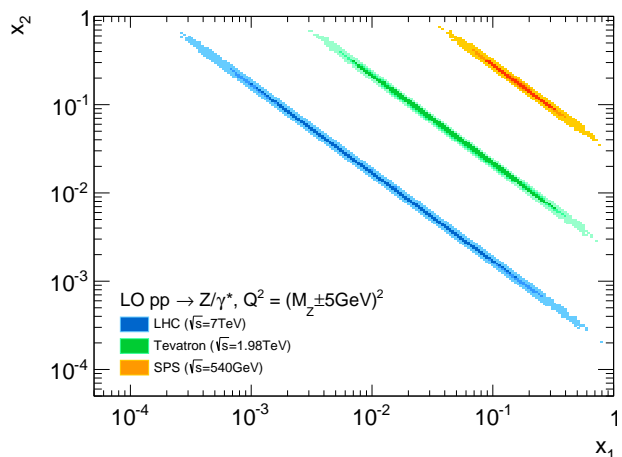


**Fig. 1** Correlation for different hadron colliders between the Bjorken  $x$  values of the two interacting partons at leading order in the reaction  $pp \rightarrow Z/\gamma^*$  for LHC and SPS and  $p\bar{p} \rightarrow Z/\gamma^*$  for Tevatron, respectively.

production. This is illustrated in Figure 2, where the kinematic plane as a function of the Bjorken  $x$  and  $Q^2$  for Drell-Yan scattering at the Tevatron, the LHC and the corresponding deep inelastic scattering experiments are compared. Similarly, measurements of the  $W$  production in association with a charm quark test the contributions in the proton from the strange quarks at  $x \approx 0.01$  as well as any  $s - \bar{s}$  asymmetries.

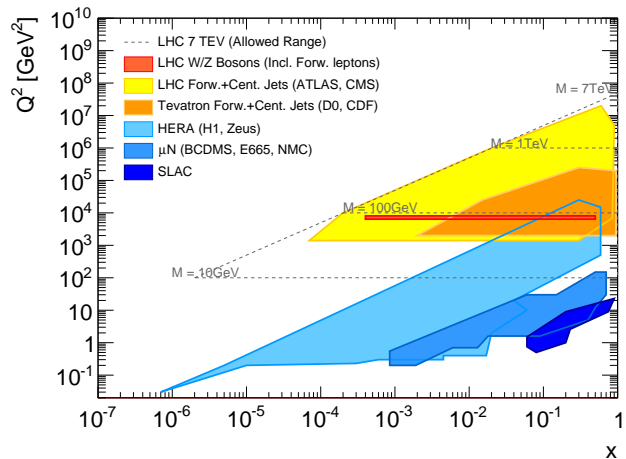


**Fig. 2** Illustration of kinematic plane in bins of Bjorken  $x$  and  $Q^2$  for Drell-Yan scattering at the Tevatron and the LHC and the corresponding deep inelastic scattering experiments.

This review article summarises the major results of the single  $W$  and  $Z$  production in the proton-proton collision data at  $\sqrt{s} = 7$  TeV recorded in the years 2010 and 2011 at the LHC by the two general purpose experiments, ATLAS and CMS. The article is organised as follows. First, in Section 2, we review the basic theory behind single vector

boson production. In this section, we pay special attention to some of the basic elements of cross-section calculations such as the matrix element calculations, the parton shower modelling and parton distribution functions. We also summarise here the theoretical predictions used in this review. In Section 3, we describe the ATLAS and CMS detectors at the LHC and discuss in a general manner the basic principles of lepton and jet reconstruction. Section 4 delineates how cross-sections are measured at the LHC, while Section 5 highlights the event selection and the background estimates for the measurements presented here. Finally we present the results for inclusive single vector boson production in Section 6 as well as the production in association with jets in Section 7. In Section 8, we conclude and provide thoughts on future measurements.

## 2 Vector Boson Production in the Standard Model

The electroweak Lagrangian of the Standard Model after electroweak symmetry breaking, i.e. after the Higgs Boson has acquired a vacuum expectation value, can be written as [35]

$$\mathcal{L}_{EW} = \mathcal{L}_K + \mathcal{L}_N + \mathcal{L}_C + \mathcal{L}_{WWV} + \mathcal{L}_{WWVV} + \mathcal{L}_H + \mathcal{L}_{HV} + \mathcal{L}_Y. \quad (1)$$

where the terms in Equation 1 are schematically illustrated as tree level Feynman graphs in Figure 3. The kinetic term,  $\mathcal{L}_K$ , describes the free movement all fermions and bosons. It involves quadratic terms and the respective masses. The term  $\mathcal{L}_N$  describes the interaction of the photon and the Z boson to fermions, while  $\mathcal{L}_C$  describes the interaction of the W-Boson to left-handed particles or right-handed anti-particles. The self interaction of gauge bosons is a direct consequence of the  $SU(2)_L$  group structure and is described by  $\mathcal{L}_{WWV}$  and  $\mathcal{L}_{WWVV}$ , representing three-point and four-point interactions, respectively. The three- and four-point self-interaction of the Higgs boson is described by  $\mathcal{L}_H$ , while the interaction of the Higgs boson to the gauge bosons is represented in  $\mathcal{L}_{HV}$ . The last term in Equation 1,  $\mathcal{L}_Y$  characterises the Yukawa couplings between the massive fermions of the Standard Model and the Higgs field.

For the single Z boson production at hadron colliders,  $\mathcal{L}_N$  is

$$\mathcal{L}_N = e J_\mu^{em} A^\mu + \frac{g}{\cos \theta_W} (J_\mu^3 - \sin^2 \theta_W J_\mu^{em}) Z^\mu, \quad (2)$$

where  $J_\mu^{em}$  describes the electromagnetic current, i.e. the sum over all fermion fields weighted by their electromagnetic charges, and  $J_\mu^3$  represents the weak current, involving only left-handed particles and right-handed anti-particles with their

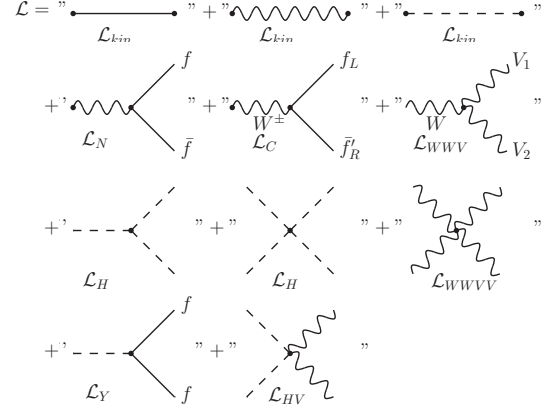


**Fig. 3** Schematic illustration of the Lagrangian describing the electroweak sector of the Standard Model (See Equation 1).

respective weak isospins. The weak mixing angle,  $\theta_W$ , describes the relative contribution of the weak and electromagnetic part of the interaction. The production of the single W bosons is described by

$$\mathcal{L}_C = -\frac{g}{\sqrt{2}} \left[ \bar{u}_i \gamma^\mu \frac{1-\gamma^5}{2} V_{ij}^{CKM} d_j + \bar{\nu}_i \gamma^\mu \frac{1-\gamma^5}{2} e_i \right] W_\mu^+ + h.c., \quad (3)$$

where only the terms for first generation are explicitly shown. The quark and lepton spinor fields are denoted by  $u_i, d_j$  and  $\nu_i, e_i$ . The term  $(1-\gamma^5)$  acts as a projector for the left-handed components of the spinors, meaning that the charge current acts exclusively on left-handed particles and right-handed anti-particles, while for the neutral current all spinor components play a role due to the electromagnetic part of the interaction term. The Cabbibo-Kobayashi-Maskawa (CKM) matrix is denoted as  $V_{ij}^{CKM}$  [36]. In this review article, we will concentrate on the terms of the Electroweak Lagrangian represented in Equation 2 and 3, as they describe the single vector boson production within the Standard Model.

Before discussing the experimental results, we first review the central parts of the theoretical predictions of the gauge boson production cross-sections at the LHC. In Section 2.1 the calculation of the cross-section is defined, which is shown to consist of two main parts; the matrix-element term describing the parton interactions and the parton distribution functions describing the proton. As the lowest-order matrix-element term for W and Z production is a frequent example in many particle physics textbooks, we extend the formalism in Section 2.2 by discussing higher-order corrections from the QCD and Electroweak theories and emphasise why these are important to the experimental measurements. The hard scatter process, which at high energy scales

can be connected to the lower energies scales via parton showering models is discussed in Section 2.3. Finally, the second part of the cross-section calculation, the parton distribution functions, is briefly reviewed in Section 2.4. In addition, we discuss some critical inputs which are needed to perform these calculations. This includes the available models for hadronisation of final state particles (section 2.5) and the description of multiple particle interactions (section 2.6). A discussion of the available computing codes, which are used to compare the latest LHC measurements with the predictions of the Standard Model, can be found in Section 2.7. Our discussion ends with an overview of the definition and interpretation of some observables which are important for understanding QCD dynamics (section 2.8).

Several introductory articles on the production of vector bosons in hadron collisions are available. We summarise here the essential aspects along the lines of [37], [38]. Related overview articles on parton density functions at next-to-leading order at hadron colliders and subsequently jet physics in electron-proton can be found in [39] and [40], respectively.

## 2.1 Cross-section calculations

The calculation of production cross-sections in proton-proton collisions at the LHC is, in general, a combination of two energy regimes: the short-distance or high-energy regime and the long-distance or low-energy regime. By the factorisation theorem, the production cross-section can therefore be expressed as a product of two terms: one describing the parton-parton cross-section,  $\hat{\sigma}_{q\bar{q}\rightarrow n}$  at short-distances and another describing the complicated internal structure of protons at long distances. For large momentum transfers of the interacting partons in the short-distance term, the parton-parton interaction can be evaluated using perturbative QCD calculations. However, in the long-distance term, where perturbative calculations are no longer applicable, parton density functions (PDFs) are used to describe the proton structure in a phenomenological way. These functions are written as  $f_{a/A}(x, Q^2)$  for the parton  $a$  in the proton A where  $x = \frac{p_a}{p_A}$  is the relative momentum of the parton in direction of the proton's momentum and  $Q^2$  is this energy scale of the scattering process. The scale at which the long-distance physics of the PDF description and the short-distance physics of parton-parton interaction separate is called the factorisation scale and is defined as  $\mu_F = Q$ . For the production of a vector boson via quark-fusion, the energy scale is set to the mass of the vector boson, which in turn can be expressed by the invariant mass of final state fermions  $f$ , i.e.  $Q^2 = m_V^2 = m_{f\bar{f}}$ .

The proton-proton cross-section is thereby expressed as

$$\sigma_{p_A p_B \rightarrow n} = \sum_q \int dx_a dx_b f_{a/A}(x_a, Q^2) f_{b/B}(x_b, Q^2) \hat{\sigma}_{ab \rightarrow n} \quad (4)$$

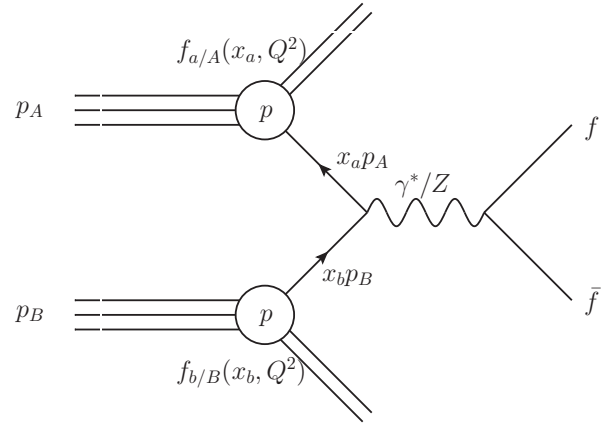


**Fig. 4** Illustration of cross-section calculation in a proton-proton collision at the LHC.

and shown graphically for  $Z$  production in Figure 4. The functions  $f_{a/A}$  and  $f_{b/B}$  denote the PDFs for the partons  $a$  and  $b$  in protons  $A$  and  $B$ . All quark flavours are accounted for in the sum and the integration is performed over  $x_a$  and  $x_b$ , describing the respective momentum fractions of the interacting partons. The subset of perturbative corrections from real and virtual gluon emissions, which are emitted collinearly to the incoming partons, lead to large logarithms that can be absorbed in the PDFs.

Inclusive hard-scattering processes can be described using the factorisation theorem [41], [42]. This approach is also applicable when including the higher order perturbative QCD corrections, which are discussed in more detail in Section 2.2.2. When expanding the parton-parton cross-section in terms of  $\alpha_s$ , the formula for the cross-section becomes:

$$\sigma_{p_A p_B \rightarrow n} = \sum_q \int dx_a dx_b \int f_{a/A}(x_a, Q^2) f_{b/B}(x_b, Q^2) \times [\hat{\sigma}_0 + \alpha_s(\mu_R^2) \hat{\sigma}_1 + \dots]_{ab \rightarrow n}, \quad (5)$$

where  $\hat{\sigma}_0$  is the tree-level parton-parton cross-section and  $\hat{\sigma}_1$  is the first order QCD correction to the parton-parton cross-section, etc. The renormalisation scale,  $\mu_R$  is the reference scale for the running of  $\alpha_s(\mu_R^2)$ , caused by ultraviolet divergences in finite-order calculations.

Writing this equation in terms of the matrix elements yields

$$\sigma_{p_A p_B \rightarrow n} = \sum_q \int dx_a dx_b \int d\phi_n \times f_{a/A}(x_a, Q^2) f_{b/B}(x_b, Q^2) \frac{1}{2\hat{s}} |m_{q\bar{q}\rightarrow n}|^2(\phi_n), \quad (6)$$

where  $1/(2\hat{s})$  is the parton flux,  $\phi_n$  is the phase space of the final state and  $|m_{q\bar{q}\rightarrow n}|$  is the corresponding matrix element for a final state  $n$ , which is produced via the initial state  $q\bar{q}$ . The matrix element can then be evaluated according to perturbation theory as a sum of Feynman diagrams,  $m_{q\bar{q}\rightarrow n} = \sum_i F_{q\bar{q}n}^{(i)}$ . The evaluation of these integrals over the full phase space is typically achieved via Monte Carlo sampling methods.

## 2.2 Matrix-element calculations

### 2.2.1 Leading-order calculations

The calculation of the electron-positron annihilation cross-section in pure Quantum Electrodynamics (QED), i.e.  $e^+e^- \rightarrow \mu^+\mu^-$ , is straightforward and can easily be extended to the quark-antiquark annihilation cross-section by including the colour factor of  $1/3$  and accounting for the charge  $Q_q$  of the involved quarks  $q$ :

$$\hat{\sigma}_{q\bar{q}\rightarrow l\bar{l}} = \frac{4\pi}{9\hat{s}} \cdot \alpha_{em}^2 \cdot Q_q^2, \quad (7)$$

where  $\hat{s} = (x_A P_A + x_B P_B)^2 = x_A x_B s$  and  $\sqrt{\hat{s}}$  denotes the center-of-mass energy of the proton-proton collision. In an electroweak unified theory, the cross-section must also include the exchange of a  $Z$  boson for larger energies ( $\sqrt{\hat{s}} > 40$  GeV) and is therefore extended by

$$\hat{\sigma}_{q\bar{q}\rightarrow l\bar{l}} = \frac{4\pi}{9\hat{s}} \left\{ Q_q^2 - Q_q \frac{\sqrt{2}G_F m_Z^2}{4\pi\alpha} g_V^l g_V^q \text{Re}(K(\hat{s})) + \frac{G_F^2 m_Z^4}{8\pi^2 \alpha_{em}^2} \cdot ((g_V^l)^2 + (g_A^l)^2) \cdot ((g_V^q)^2 + (g_A^q)^2) |K(\hat{s})|^2 \right\}.$$

The vector and axial couplings of the  $Z$  bosons to the leptons and quarks are denoted as  $g_V = g_L + g_R$  and  $g_A = g_L - g_R$  which can be expressed as combinations of left- and right-handed chiral states for the quarks  $q$  and leptons  $l$ . The  $Z$  boson propagator  $K(\hat{s})$  can be written as

$$K(\hat{s}) = \frac{\hat{s}}{\hat{s} - m_Z^2 + im_Z \Gamma_Z}. \quad (8)$$

In the narrow-width approximation, the  $Z$  boson is assumed to be a stable particle and the propagator reduces to a  $\delta$ -function. This approximation is based on the fact that the width of the  $Z$  boson ( $\Gamma_Z \approx 2.5$  GeV) is small compared to its mass ( $m_Z \approx 91$  GeV). Hence the parton-parton cross-section can be expressed as

$$\hat{\sigma}_{q\bar{q}\rightarrow Z} = \frac{\sqrt{2}\pi}{3} G_F m_Z^2 ((g_V^q)^2 + (g_A^q)^2) \delta(\hat{s} - m_Z^2), \quad (9)$$

when omitting the interference with the photon-exchange in the s-channel<sup>1</sup>.

The decay of the  $Z$  boson into fermion pairs is described by the branching ratio  $Br(Z \rightarrow f\bar{f}) = \Gamma(Z \rightarrow f\bar{f})/\Gamma_Z$ , where the partial width  $\Gamma(Z \rightarrow f\bar{f})$  is given in lowest order by

$$\Gamma(Z \rightarrow f\bar{f}) = N_C \frac{G_F m_Z^3}{6\sqrt{2}\pi} ((g_V^f)^2 + (g_A^f)^2), \quad (10)$$

where the factors  $g_V^f$  and  $g_A^f$  are again the vector- and axial couplings for the respective fermions  $f$  to the  $Z$  boson. The colour factor  $N_C$  is 1 for leptons and 3 for quarks. This leads to a prediction of  $\approx 70\%$  decays into quark and antiquarks, but only  $\approx 3.4\%$  for the decay into a single generation of charged leptons.

The lowest-order cross-section for the  $W$  boson production via quark-antiquark fusion can be derived in a similar manner. In contrast to the  $Z$  boson production, quarks from different generations can couple to the  $W$  boson, while the interference with the electromagnetic sector is not present. The cross-section in the narrow width approximation is given by

$$\hat{\sigma}_{q\bar{q}'\rightarrow W} = \frac{\sqrt{2}\pi}{3} G_F m_W^2 |V_{qq'}^{CKM}|^2 \delta(\hat{s} - m_W^2), \quad (11)$$

where the CKM matrix element accounts for the quark-generation mixing. The partial decay width of the  $W$  boson at lowest order is

$$\Gamma(W \rightarrow f\bar{f}') = N_C \frac{G_F m_W^3}{6\sqrt{2}\pi}, \quad (12)$$

leading to  $1/3$  probability for leptonic decays and  $2/3$  for decays into quark/antiquark pairs.

### 2.2.2 Perturbative QCD corrections and jets

The leading-order calculations of the  $W$  and  $Z$  boson production, as shown in Section 2.2.1, suggest that the momentum of the boson in the transverse plane is zero. Yet it is well known from collider experiments that the transverse momentum ( $p_T$ ) of  $W$  and  $Z$  bosons peaks at few GeV, with a pronounced tail to high values, i.e.  $p_T \gg m_V$  [43], [44], [45], [46]. To understand the physical origin of this, two different effects have to be taken into account. First, the interacting partons are believed to have an intrinsic transverse momentum ( $k_T$ ) relative to the direction of the proton, leading to an exponentially decreasing  $p_T$  distribution of the vector boson. The experimentally determined value of the average intrinsic momentum is  $\langle k_T \rangle = 0.76$  GeV, measured in proton-neutron collisions [47] and is not large enough to explain

<sup>1</sup>The interference at  $\hat{s} = m_Z^2$  is at per mille level

the observed  $p_T$  distribution of vector bosons in hadron collisions. The second, larger effect arises from higher order QCD corrections to the vector boson production, which can lead to the radiation of additional quarks and gluons in the final state in the transverse plane. The vector sum of these emissions has to be balanced by the transverse momentum of the produced vector boson, which in turn acquires a transverse momentum. In the regime where  $\alpha_s$  is small, these perturbative QCD corrections may be calculated. The two contributing classes of next-to-leading-order (NLO) corrections, i.e. the virtual loop corrections and the real emissions of gluons/quarks, are illustrated in Figure 5. The correction terms with virtual loops do not affect the transverse momentum spectrum of the vector boson directly. The real corrections however, imply the existence of  $2 \rightarrow 2$  processes, leading to an additional parton in the final state which boosts the  $W$  or  $Z$  boson in the transverse plane.

The generic form of the production cross-section for the processes  $q\bar{q} \rightarrow Vg$  and  $qg \rightarrow Vq'$ , where  $V$  stands for a vector boson, can be expressed by the Madelstam variables, describing the Lorentz invariant kinematics of a  $2 \rightarrow 2$  scattering process. The resulting cross-section at NLO is proportional to

$$\sigma \sim \frac{2 \cdot m_V^2 \cdot s + t^2 + u^2}{tu}, \quad (13)$$

As  $t, u \rightarrow 0$ , divergencies in Equation 13 occur. This can be interpreted as final state quarks or gluons with a vanishing transverse momentum, i.e. those which are collinear to the incoming parton. Therefore, a minimal  $p_T$  requirement of the additional quark or gluon in the final state needs to be applied to obtain a finite production cross-section prediction. In the calculation of the fully inclusive production cross-section, the divergencies are compensated by the virtual loop corrections.

Two main energy regimes of the transverse momentum spectrum of the vector boson production are considered here: A high energy regime, where  $p_T \gg m_V$  and an intermediate

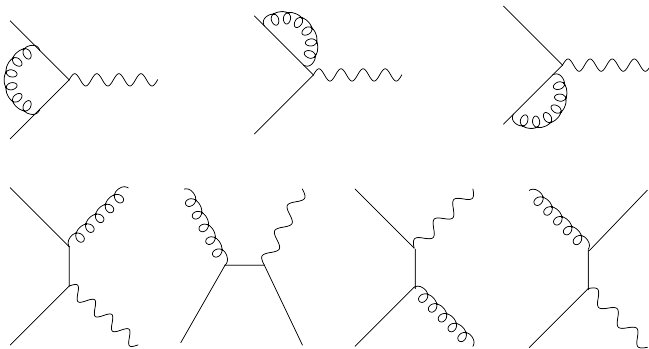


Fig. 5 Perturbative QCD corrections

regime, where  $k_T < p_T(V) < m_V/2$ . For very large transverse momenta of the vector bosons ( $p_T \gg m_V$ ), the real NLO corrections lead to an expected transverse momentum distribution of

$$\frac{d^2\sigma}{d^2p_T} \sim \frac{\alpha_s(p_T^2)}{p_T^4}. \quad (14)$$

The linear dependence of  $\alpha_s$  is a consequence of the NLO QCD corrections, leading to one additional parton in the final state ( $V+1$  jet production).

Each additional parton in the final state requires one additional higher order QCD correction and therefore an additional order of  $\alpha_s$ . Examples of leading-order Feynman diagrams for the  $Z+2$  jet production are shown in Figure 6. For QCD corrections with multiple jets, the probability that an additional parton is a radiated gluon is governed by a Poisson distribution. This implies that the leading-order term for a  $V+n$ -jet final state, called *Poisson scaling*, has the form of

$$\sigma_{V+n-jet}^{LO} \sim \frac{\bar{n}e^{-\bar{n}}}{n!} \sigma_{tot}, \quad (15)$$

where  $\sigma_{tot}$  is the total cross-section,  $\bar{n}$  is an expectation value of the Poisson. This is the expected behaviour at  $e^+e^-$  colliders [48], where PDFs do not play a role. However, at hadron colliders, the experimentally observed  $V+n$ -jet final state, called *staircase scaling*, has the form of

$$\sigma_{V+n-jet}^{LO} \sim \sigma_0 e^{-an}, \quad (16)$$

where the coefficients  $a$  depend on the exact definition of a jet and  $\sigma_0$  is the zero-jet exclusive cross-section. The ratio of the  $n$ -jet and  $(n+1)$ -jet cross-sections is then a constant value,  $\frac{\sigma_{n+1}}{\sigma_n} = e^{-a}$ , where  $e^{-a}$  is a phenomenological parameter which is measurement dependent. The reason for observed staircase scaling at hadron colliders is two-fold. At small numbers of additional partons, the emission of an additional parton is suppressed in the parton density function. At larger numbers of additional partons, the probability of gluon radiation no longer follows a Poisson distribution due to the non-abelian nature of QCD theory, which states that a gluon can radiate from another gluon. For large jet multiplicities a deviation from the staircase scaling behaviour is expected, as the available phase space for each additional jet in the final state decreases.

Today, several leading-order calculations, such as [49] and [50], are available that describe more than six partons in the final state. The inclusive production cross-section and the associated rapidity distribution for vector bosons is known today to next-to-next-to-leading order (NNLO) [51], [52], [53].

The intermediate momentum range of  $k_T < p_T(V) < m_V/2$  can also be assessed with perturbative calculations.

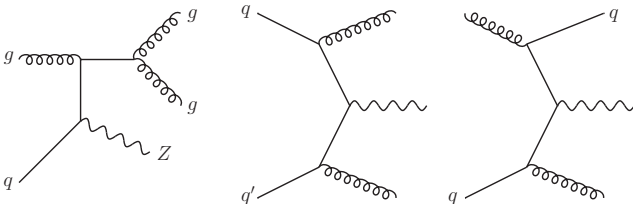


**Fig. 6** Leading-order Feynman diagram for Z + 2-jet Production

However, higher-order corrections, manifested as low energetic gluons emitted off the incoming partons at intermediate energies, must be included for a correct description of the experimental data. This can be most easily seen in the limit of  $t \rightarrow 0$  and  $u \rightarrow 0$ ; then the final state gluon in the  $q\bar{q}' \rightarrow Vg$  process becomes collinear to the incoming parton. The corresponding Feynman diagram can be redrawn as initial state radiation (ISR) as shown in Figure 7.

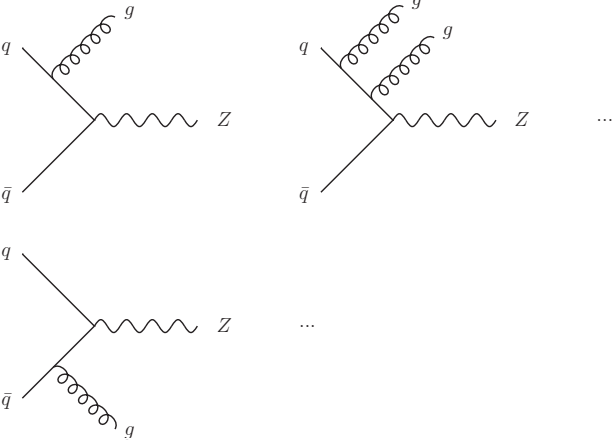


**Fig. 7** Example Feynman diagrams illustrating initial state radiation of gluons in the leading-order Drell-Yan process.

The main contributions of these collinear gluon emissions to the cross-section at the  $n$ -th order are given by

$$\frac{1}{\sigma} \frac{d\sigma}{dp_{\perp}^2} \sim \frac{1}{p_{\perp}^2} \alpha_s^n \ln^{2n-1} \frac{m_V^2}{p_{\perp}^2}. \quad (17)$$

Such collinear gluon emissions are also the basis for parton showers, which will be discussed in Section 2.3. Summing up the gluon emissions to all orders leads to

$$\frac{1}{\sigma} \frac{d\sigma}{dp_{\perp}^2} \approx \frac{d}{dp_{\perp}^2} e^{\left(-\frac{\alpha_s}{2\pi} C_F \ln^2 \frac{m_V^2}{p_{\perp}^2}\right)}, \quad (18)$$

where  $C_F = 4/3$  is the QCD colour factor for gluons. This approach, known as *Resummation* [54], has been significantly improved and extended in recent years and provides currently the most precise predictions for the transverse momentum distribution of vector bosons in the low energy regime.

### 2.2.3 Electroweak corrections

So far, only QCD corrections to  $W$  and  $Z$  boson production have been discussed. The virtual one loop QED corrections and the real photon radiation corrections are illustrated via Feynman diagrams in Figure 8. The NLO corrections to the charged and neutral currents are well known [55], [56]. In particular, the full  $\mathcal{O}(\alpha_{em})$  corrections to the  $pp \rightarrow \gamma/Z \rightarrow l^+l^-$  process with  $\mathcal{O}(g^4 m_{\perp}^2/m_W^2)$  corrections to the effective mixing angle  $\sin^2\theta_{eff}^2$  and  $m_W$  are available [57–61].

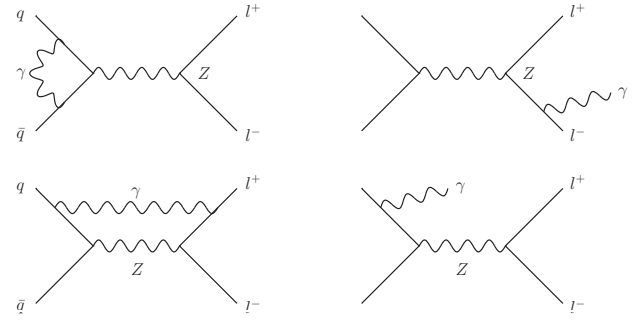


**Fig. 8** Examples of leading-order QED corrections

Even though the electroweak corrections to the vector boson production cross-section are small compared to the higher-order QCD corrections, they lead to a significant distortion of the line shape of the invariant mass and subsequently to the transverse momentum spectrum of the decay leptons. The comparison between the corresponding distributions with and without electroweak corrections is illustrated in Figure 9.

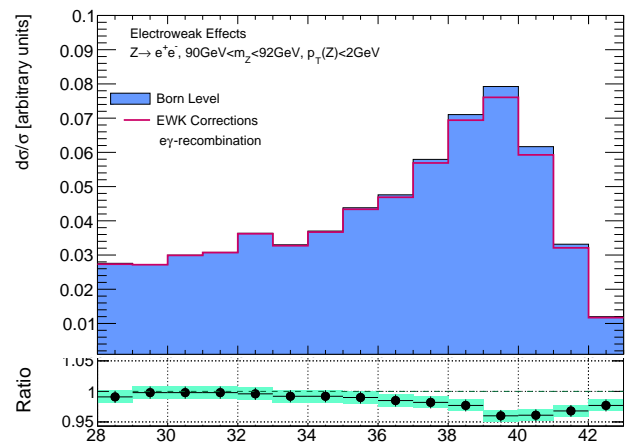


**Fig. 9** Electroweak (EWK) corrections to the lepton transverse momentum for the neutral current Drell-Yan process at the LHC [62]. Results are presented for bare electrons and electrons employing electron-photon recombination, respectively.

In general, electroweak corrections at moderate energies are dominated by final-state radiations (FSR) of photons, which is indicated by the upper right diagram in Figure 8. Certain measurements, like the determination of the  $W$  boson mass from the decay lepton  $p_T$  distribution, are sensitive to these corrections. For this measurement, this effect can induce a shift of up to 10 MeV on  $m_W$  in the muon decay channel. In contrast, the electron decay channel is less effected due to the nature of electron reconstruction in the detector, where the FSR photons are usually reconstructed together with the decay electron. Therefore the relative magnitude of the electroweak corrections with respect to the QCD corrections must be considered individually for each measurement. It should be noted that there are also diagrams with photons in the initial state and hence the parton density functions evolve with combined QCD and QED evolution equations. That can lead to sizable corrections in the high and low mass Drell-Yan production [63].

### 2.3 Parton shower models

As discussed in the previous section, matrix-element calculations at fixed-order provide cross-sections assuming that the final state partons have large momenta and are well separated from each other. Parton shower models provide a relation between the partons from the hard interaction ( $Q^2 \gg \Lambda_{QCD}$ ) to partons near the energy scale of  $\Lambda_{QCD}$ . Here  $\Lambda_{QCD}$  is defined as the transition energy between the high-energy and low-energy regions. A commonly used approach for parton shower models is the leading-log approximation, where showers are modelled as a sequence of splittings of a parton  $a$  to two partons  $b$  and  $c$ . QCD theory allows for three types of possible branchings,  $q \rightarrow qg$ ,  $g \rightarrow gg$  and  $g \rightarrow q\bar{q}$ , while only two branchings exist in QED theory, namely  $q \rightarrow q\gamma$  and  $l \rightarrow l\gamma$ .

The differential probability  $dP_a$  for a branching for QCD emissions is given by the Dokshitzer-Gribov-Lipatov-Altarelli-Parisi (DGLAP) evolution equations [64–66]

$$dP_a = \sum_{b,c} \frac{\alpha_s(t)}{2\pi} P_{a \rightarrow b,c}(z) dt dz, \quad (19)$$

with the evolution time  $t$  defined as  $t = \ln(Q^2/\Lambda_{QCD}^2)$ .  $Q^2$  denotes the momentum scale at the branching and  $z$  the momentum fraction of the parton  $b$  compared to parton  $a$ . The sum runs over all possible branchings and  $P_{a \rightarrow b,c}$  denotes the corresponding DGLAP splitting kernel.

This relation also holds for the QED branchings, where the coupling constant in Equation 19 is replaced with  $\alpha_{em}$ . For final state radiation, the emission of particles due to subsequent branchings of a mother parton is evolved from  $t = Q_{hard}^2$  at the hard interaction to the non-perturbative regime

$t \approx \Lambda_{QCD}$ . Initial-state radiation can be ordered by an increasing time, i.e. going from a low energy scale to the hard interaction. This can be interpreted as a probabilistic evolution process connection two different scales: the initial scale  $Q_0^2$  of the interaction to the scale of the hard interaction scale  $Q_{hard}^2$ . During this evolution, all possible configurations of branchings, leading to a defined set of partons taking part in the hard interaction, are considered.

The implementation of parton showers is achieved with Monte Carlo techniques. They are used to calculate the step-length  $t_0$  to  $t$  where the virtuality of the parton decreases with no emissions. At the evolution time  $t$ , a branching into two partons occurs where the resulting sub-partons have smaller virtuality than the initial parton. This procedure is then repeated for the sub-partons, starting at the new evolution time  $t_0 = t$ .

Therefore the probability for the parton  $a$  at the scale  $t_0$  not to have branched when it is found at the scale  $t$  has to be determined. This probability  $P_{no-branching}(t_0, t)$  is given by the Sudakov form factor [67], which can be expressed as

$$S_a(t) = \exp\left(-\int_{t_0}^t dt' \sum_{b,c} I_{a \rightarrow b,c}(t')\right), \quad (20)$$

where

$$I_{a \rightarrow b,c}(t) = \int_{z_-(t)}^{z_+(t)} dz \frac{\alpha_s(t)}{2} \cdot P_{a \rightarrow b,c}(z) \quad (21)$$

is the differential branching probability for a given evolution time  $t$  with respect to the differential range  $dt'$ . The latter relation follows directly from Equation 19, by integrating over the allowed momentum distributions  $z$ . The probability for a branching of a given parton  $a$  at scale  $t$  can then be expressed by the derivative of the Sudakov form factor  $S_a(t)$ :

$$\frac{dP_a(t)}{dt} = \left(\sum_{b,c} I_{a \rightarrow b,c}\right) S_a(t). \quad (22)$$

This relation describes the effect known as Sudakov suppression: The first factor  $I_{a \rightarrow b,c}$ , which describes the branching probability at a given time  $t$ , is suppressed by the Sudakov form factor  $S_a(t)$ , i.e. by taking into account the possibility of branchings before reaching the actual scale  $t$ .

The branching of the initial-state partons during the parton shower therefore leads to the emission of gluons or quarks, which in turn may add an additional jet to the event. The final-state partons predicted within the leading-log approximation are dominated by soft and collinear radiations and hence large momentum jets that are not expected to be described correctly within this approximation. The kinematics of the missing hard scatter components are predicted by the



corresponding higher-order diagrams, which have been discussed in Section 2.2.2.

The main advantage of the parton shower approach is its simplicity compared to matrix-element calculations which increase in complexity when considering more independent partons in the initial and final states. However, there is an important difference between the soft-gluon emission described by parton shower and the emission of a gluon calculated by NLO matrix element. While the full matrix-element calculation includes the spin-1 nature of the gluon and hence induced polarisation effects on the intermediate gauge boson, the parton shower algorithm does not take into account spin effects.

#### 2.4 Parton distribution functions and scale dependencies

The PDFs play a central role not only in the calculation of the cross-section in Equation 5, but also in the modelling of parton showers and hadronisation effects. A generic PDF  $f_i(x, \mu_F, \mu_R)$  describes at lowest order the probability of finding a parton of type  $i$  with a momentum fraction  $x$  when a proton is probed at the scale  $\mu_F$ . The factorisation and renormalisation scale parameters  $\mu_F$  and  $\mu_R$  in the PDF definition act as cut-off parameters to prohibit infrared and ultraviolet divergences. If a cross-section could be calculated to all orders in perturbation theory, the calculation would be independent from the choice of the scale parameters, since the additional terms would lead to an exact cancellation of the explicit scale dependence of the coupling constant and the PDFs. Both scales are usually chosen to be on the order of the typical momentum scales of the hard scattering process, to avoid terms with large logarithms appearing in the perturbative corrections. For the Drell-Yan process at leading order this implies  $\mu_F = \mu_R = m_Z$ . It should be noted that both scales are usually assumed to be equal, even though there is no reason from first principles for this choice. The dependence of the predicted cross-section on  $\mu_F$  and  $\mu_R$  is thus a consequence of the missing/unknown higher-order corrections. The dependence is therefore reduced when including higher orders in the perturbation series. The uncertainty on the cross-section prediction due to scale uncertainties is usually estimated by varying both scales simultaneously within  $0.5 \cdot Q < \mu_F, \mu_R < 2 \cdot Q$ , where  $Q$  is the typical momentum scale of the hard process studied. However, this evaluation procedure sometimes provides results that are too optimistic and the differences between the leading-order and NLO calculations are not always covered by the above procedure.

As the actual form of  $f_i(x, \mu_F)$  cannot be predicted with perturbative QCD theory, a parameterised functional form has to be fitted to experimental data. The available data for the PDF determination comes mainly from deep inelastic scattering experiments at HERA, neutrino data, as well as

Drell-Yan and jet production at the Tevatron and LHC colliders. Note that the scale dependence of  $f_i$  is predicted by the DGLAP evolution equations.

In order to fit PDFs to data, a starting scale, where perturbative QCD predictions can be made, has to be chosen and a certain functional form of the PDFs has to be assumed. A typical parametrisation of  $f_i(x, \mu_F)$  takes the form

$$f_i(x, \mu_F) = a_0 x^{a_1} (1-x)^{a_2} P(x, a_3, a_4, \dots), \quad (23)$$

where  $P$  is a polynomial function and  $a_j$  are free fit parameters which cannot be predicted from perturbative QCD calculations, but can only be determined by experiment. In a second step, a factorisation scheme, i.e. a model for the handling of heavy quarks, and an order of perturbation theory has to be chosen. The DGLAP evolution equations can then be solved in order to evolve the chosen PDF parametrisation to the scale of the data. The measured observables can then be computed and fitted to the data. The PDF fits are currently performed and published for leading-order, NLO and NNLO calculations. Even though most matrix elements are known to NLO order in QCD theory, some parton shower models are still based on leading-order considerations and therefore leading-order PDF sets are still widely used.

PDF fitting is performed by several groups. The CTEQ-TEA [68], MSTW [69], ABKM [70], GJR [71] and NNPDF [72] collaborations include all available data for their fits, but face the problem of possible incompatibilities of the input data, caused by inconsistent measurement results from different experiments. These results differ in the treatment of the parametrisation assumptions of  $f_i$ . The HERAPDF [73] group bases their PDF fits on a subset of the available data, where only the HERA measurements have been chosen as input and therefore possible inconsistencies in the fit are reduced.

It should be highlighted that the PDF approach and fitting is subject to several assumptions and model uncertainties. The actual form of the input distributions is arbitrary and hence the choice of the analytical function implies a model uncertainty. The approach of the NNPDF group is an exception as the parametrisation is chosen to be handled by a flexible neural network approach. In addition it is commonly assumed that the strange-quark content follows  $s = \bar{s} = (\bar{u} + \bar{d})/4$ . The suppression of  $s$  and  $\bar{s}$ -quark content is due to their larger masses compared to the  $\bar{u}$  and  $\bar{d}$  quarks, but a rigorous argument of the chosen suppression factor cannot be derived from first principles. Similar is the situation for heavy-flavour ( $c, b, t$ -quarks) contributions to the proton structure. Their contribution is 0 below the  $Q^2$ -threshold and is evolved according to the DGLAP-equations above.

The results presented in this paper rely mainly on the CTEQ-10 and MRST PDF sets [68], [69]. The PDF set for

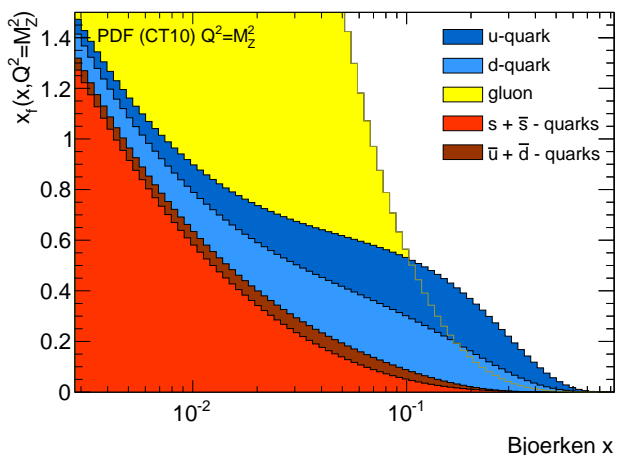


**Fig. 10** PDF distribution of the CT10 PDF set at  $Q^2 = m_Z^2$ .

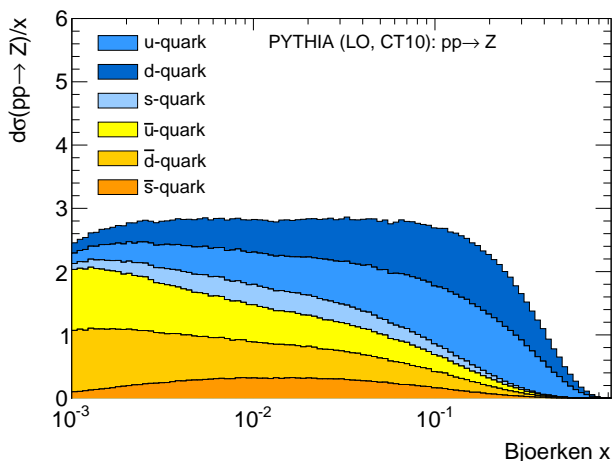


**Fig. 11** Distribution of Bjorken  $x$ -values of partons that are involved in the leading-order production of  $Z$  bosons at 7 TeV pp collisions as a stacked histogram. It should be noted that each participating valence-quark has to be matched with a corresponding sea-quark.

$Q^2 = m_Z^2$  from the CTEQ collaboration are illustrated in Figure 10. The Bjorken  $x$ -values of partons, which are involved in the leading-order production of  $Z$  bosons at 7 TeV pp collisions, are illustrated in Figure 11, where the  $x$ -values of both interacting quarks per events have been used.

The associated uncertainties of a given PDF set are based on the Hessian method [74], where a diagonal error matrix with corresponding PDF eigenvectors is calculated. The matrix and the PDF eigenvectors are functions of the fit-parameters  $a_i$ . Non-symmetric dependencies are accounted for by using two PDF errors for each eigenvector in each direction. The PDF uncertainties on a cross-section is then given by

$$\Delta\sigma = \frac{1}{2} \sqrt{\sum_{k=1}^n [\sigma(a_i^+) - \sigma(a_i^-)]^2}, \quad (24)$$

where  $a_i^\pm$  labels the corresponding eigenvectors of a chosen PDF error set. This approach assesses only the PDF fit uncertainties within a certain framework, i.e. for a chosen parametrisation and various base assumption. Hence, usually also the difference between two different PDF sets from two independent groups, e.g. CTEQ and MRST, are taken as an additional uncertainty. The same procedure for the impact of PDF related uncertainties can be applied for any observable and is not restricted to inclusive cross-sections.

## 2.5 Hadronisation

The process of how hadrons are formed from the final state partons is called hadronisation. The scale at which the hadronisation is modelled is  $Q^2 = \Lambda_{QCD}^2$ . Since this process is complex, phenomenological models must be used. A detailed discussion can be found elsewhere [75].

The first models of hadronisation were proposed in the 70s [76] and today, two models are widely in use. The so-called *string model* [77] is based on the assumption of a linear confinement and provides a direct transformation from a parton to hadron description. It accurately predicts the energy and momentum distributions of primary produced hadrons, but requires numerous parameters for the description of flavour properties, which have been tuned using data. The second approach for the description of hadronisation is known as *cluster model* [78], [79], which is based on the pre-confinement property of parton showers [80]. It involves an additional step before the actual hadronisation, where colour-singlet subsystems of partons (denoted as *clusters*) are formed. The mass spectrum of these clusters depend only on a given scale  $Q_0$  and  $\Lambda_{QCD}$ , but not on a starting scale  $Q$ , with  $Q \gg Q_0 > \Lambda_{QCD}$ . The cluster model has therefore fewer parameters than the string model, however, the description of data is in general less accurate.

The subsequent decay of primary hadrons is either directly implemented in the computing codes for hadronisation, or in more sophisticated libraries such as EVTGEN[81]. Special software libraries can be used for the description of the  $\tau$ -lepton decay, e.g. TAUOLA [82], correctly taking into account all branching ratios and spin correlations. Since hadronisation effects usually have only a small impact on the relevant observables discussed in this article, we refer to [75] for a detailed discussion.

## 2.6 Multiple-parton interactions

Equation 5 describes only a single parton-parton interaction within a proton-proton collision. However, in reality, several parton-parton interactions can occur within the same collision event. This phenomenon is known as multiple-parton interactions (MPI). Most of the MPI lead to soft additional

jets in the event which cannot be reconstructed in the detector due to their small energies. Hence they contribute only as additional energy deposits in the calorimeters. However, a hard perturbative tail of the MPI, following  $\sim dp_T^2/p_T^4$ , where  $p_T$  is the transverse momentum of the additional jets, can lead to additional jets in the experimental data. These effects must be taken into account for the study of vector boson production in association with jets. Further information about the current available models for MPI can be found in [83]. Dedicated studies of MPI have been done at the LHC using  $W$  events with two associated jets [84]. The fraction of events arising from MPI is  $0.08 \pm 0.01(\text{stat.}) \pm 0.02(\text{sys.})$  for jets with a  $p_T > 20$  GeV and a rapidity  $|y| < 2.5$ . This fraction decreases when the  $p_T$  requirements on the jets increases.

## 2.7 Available computing codes

### 2.7.1 Multiple purpose event generators

Multiple purpose event generators include all aspects of the proton-proton collisions: the description of the proton via an interface to PDF sets, initial-state shower models, the hard scattering process and the subsequent resonance decays, the simulation of final-state showering, MPI, the hadronisation modelling and further particle decays. Some frequently used generator in the following analyses are PYTHIA6 [85], PYTHIA8 [86], HERWIG [87], HERWIG++ [88] and SHERPA [89]. All of these generators contain an extensive list of Standard Model and new physics processes, calculated with fixed-order tree-level matrix elements. Some important processes, such as the vector boson production are also matched to NLO cross-sections.

The PYTHIA generator family is a long established set of multiple purpose event generators. While PYTHIA6, developed in Fortran in 1982 is still in use, the new PYTHIA8 generator was coded afresh in C++. The showering in PYTHIA6 used in this review is implemented with a  $p_T$ -ordered showering scheme, whereas the new version used here is based on a dipole showering approach. The hadronisation modelling in both versions is realised via the Lund string model. MPI are internally simulated in addition.

Similar to PYTHIA, the HERWIG generator was originally developed in Fortran and is now superseded by HERWIG++, written in C++. Both versions use an angular-ordered parton shower model and the cluster model for hadronisation. The JIMMY library [90] is used for the simulation of MPI.

The SHERPA generator was developed in C++ from the beginning and uses the dipole approach for the parton showering. The hadronisation is realised with the cluster model. The MPI are described with a model that is similar to the one

used in PYTHIA. For the analyses described here, SHERPA is generated with up to five additional partons in the final state.

### 2.7.2 Leading-order and NLO matrix-element calculations

Several programs such as ALPGEN [49] and MADGRAPH [91] calculate matrix elements for leading-order and some NLO processes, but do not provide a full event generation including parton shower or hadronisation modelling. These generators as well as SHERPA are important because they contain matrix-element calculations for the production of vector bosons in association with additional partons. ALPGEN is a leading-order matrix-element generator and includes predictions up to six additional partons in the final state. This is achieved by adding real emissions to the leading-order diagrams before the parton shower modelling. In this way, although the process is calculated at leading-order, tree-level diagrams corresponding to higher jet multiplicities can be included. Some of the virtual corrections are then added when a parton shower model is used. MADGRAPH for the analyses presented here follows a similar method and produces predictions up to four additional partons. The subsequent event generation, starting from the final parton configuration, is then performed by PYTHIA or HERWIG for ALPGEN and PYTHIA for MADGRAPH.

### 2.7.3 Parton shower matching

There is significant overlap between the phase space of NLO or n-parton final-state QCD matrix-element calculations and the application to parton showers with respect to their initial- and final-state partons, as both lead to associated jets. To avoid a potential double counting, matching schemes have been developed that allow matrix-element calculations for different parton multiplicities in the initial state and final state to be combined with parton shower models. The main strategies are based on re-weighting methods and veto-algorithms. The Catani-Krauss-Kuler-Webber (CKKW) matching scheme [92], [93] and the Mangano (MLM) scheme [94] are widely used for tree-level generators. For example, the ALPGEN generator uses the MLM scheme, whereas SHERPA uses CKKW matching for leading-order matrix-element calculation. A detailed discussion can be found in the references given.

An alternative, less generalised approach to matching schemes are merging strategies. Here the parton showers are reweighted by weights calculated by matrix-element calculations. In the PYTHIA generator only the first branching is corrected, while HERWIG modifies all emissions which could be in principle the hardest. These approaches model correctly one additional jet, but fail for higher jet multiplicities.

### 2.7.4 NLO generators

While matrix-element calculations give both a good description for the hard emission of jets in the final states and handle inferences of initial and final states correctly, they are not NLO calculations. A combined NLO calculation with parton shower models therefore is much desired. However, the above described methods work only for leading-order matrix-element calculations. For the matching between NLO matrix element and parton shower models more sophisticated methods have to be used. The MC@NLO approach [95] was the first available prescriptions to match NLO QCD matrix elements to the parton shower framework of the HERWIG generator. The basic idea is to remove all terms of the NLO matrix-element expression which are generated by the subsequent parton shower. Due to this removal approach, negative event weights occur during the event generation. The aMC@NLO generator follows a similar approach for NLO calculations. The second approach is the POWHEG procedure [96], which is currently implemented in the POWHEG-BOX framework [97]. This framework allows for an automated matching of a generic NLO matrix element to the parton shower. The POWHEG procedure foresees that the hardest emission is generated first. The subsequent softer radiations are passed to the showering generator. In contrast to the MC@NLO approach, only positive weights appear and in addition the procedure can be interfaced to other event generators apart from HERWIG. PYTHIA8 also includes possibilities to match to NLO matrix element using the POWHEG scheme.

### 2.7.5 NLO calculations and non-perturbative corrections

MCFM [98] and BLACKHAT-SHERPA [99] provide NLO calculations up to two and five additional partons respectively. These calculations differ from NLO generators as they do not provide any modelling of the parton shower. These calculations compute both the virtual and real emission corrections for higher jet multiplicities. For the virtual corrections, the calculation is achieved by evaluating one-loop corrections to the tree-level diagrams, while the real emission corrections are obtained by matrix-element calculations which include an additional emitted parton. Several different techniques are used for these calculations, see for example [99].

Since MCFM and BLACKHAT-SHERPA are not matched to a parton shower model, they can not be directly compared to data or simulations which have parton showering and hadronisation applied to the final-state particles. To mimic the effects of both the parton shower and the hadronisation, *non-perturbative corrections* are estimated using a multiple purpose generator such as PYTHIA. These corrections are derived by comparing PYTHIA with and without the parton shower and hadronisation models and applied directly to

prediction cross-sections. The non-perturbative corrections are on the order of 7% for jets of  $p_T < 50$  GeV and reduce to zero at higher  $p_T$  values.

Finally, the inclusive  $W$  and  $Z$  boson production cross-sections in proton-proton collisions are also known to NNLO precision in  $\alpha_s$  and can be calculated with the FEWZ generator [100]. This generator allows also the prediction of several observables of the final-state objects, such as the rapidity distribution of the produced vector bosons.

### 2.7.6 Calculations based on resummation

There are specific programs available, such as RESBOS [101], which are based on resummed calculations and therefore are suited to describe the transverse momentum spectrum of vector boson production. RESBOS provides a fully differential cross-section versus the rapidity, the invariant mass and the transverse momentum of the vector boson as intermediate state of a proton-proton collision. The resummation is performed to NNLL approximation and matched to NNLO perturbative QCD calculations at large boson momenta.

### 2.7.7 Overview and predicted inclusive cross-sections

A summary of all Monte Carlo (MC) generators used to describe the relevant signal processes in this work is shown in Table 1. The order of perturbation theory, the parton shower matching algorithms and the corresponding physics processes are also stated.

Table 2 summarises several predictions for different generators and PDF sets for production cross-sections of selected final states in proton-proton collisions at  $\sqrt{s} = 7$  TeV. Uncertainties due to scale and PDF variations are shown in addition. As indicated in the table, the increase of the cross-section from leading-order to NNLO predictions is more than 15%. The difference between different PDF sets is in the order of 1.5% and covered by the associated PDF uncertainties.

## 2.8 QCD dynamics and angular coefficients

To leading order, the angular distribution of the decay products in the process  $e^+e^- \rightarrow \mu^+\mu^-$  can easily be calculated and exhibits a  $(1 + \cos^2 \theta)$  dependence, where  $\theta$  is the angle between the incoming electron and the outgoing positive charged muon. A similar angular dependence is derived for the quark/antiquark annihilation including a  $Z$  boson exchange in the corresponding s-channel diagram. However, the coupling and gauge structure of the weak interaction as well as higher-order corrections leads to new angular-dependent terms in the differential production cross-sections. The measurement of these terms therefore provides not only

**Table 1** Monte Carlo programs which are used for the analyses described in this review article. The information on the order of  $\mathcal{O}(\alpha_s)$  in the matrix-element calculation, the generator functionality, the possibility to match matrix-element calculations with parton showers and the functionality within the analyses are given. The structure of the table is based on [37].

Program	Matrix-Element $\mathcal{O}(\alpha_s)$	Full Event Generator	Merging/Matching	Functionality w.r.t. W / Z Production
PYTHIA	LO	yes	matrix-element correction for first branching	inclusive production
HERWIG	LO	yes	matrix-element correction for hardest branching	inclusive production
MC@NLO	NLO	yes (interface to HERWIG)	PS matching	inclusive production
aMC@NLO	NLO	yes (interface to HERWIG)	PS matching	inclusive production
POWHEGBOX	NLO	yes (interface to PYTHIA or HERWIG)	PS matching	inclusive production
ALPGEN	LO	no (but interface to PYTHIA/HERWIG)	MLM (all parton multiplicities)	W / Z +Jets (incl. large. multipl.)
MADGRAPH	LO	no (but interface to PYTHIA)	n.a. (all parton multiplicities)	W / Z +Jets (incl. large multipl.)
SHERPA	LO	yes	CKKW (all parton multiplicities)	W / Z +Jets (incl. large multipl.)
BLACKHAT-SHERPA	NLO	no (only parton level)	n.a.	W / Z +Jets (incl. large multipl.)
RESBOS	Resummation	no (only boson kinematics)	n.a.	$p_T$ spectrum of W / Z bosons
MCFM	NLO	no (only parton level)	n.a.	NLO corrections to integral rates and shapes
FEWZ	NNLO	no (only boson kinematics)	n.a.	NNLO corrections to integral rates and shapes

**Table 2** Prediction of the cross-sections of W and Z boson ( $66 \text{ GeV} < m_{ll} < 116 \text{ GeV}$ ) production in  $\sqrt{s} = 7 \text{ TeV}$  pp-collisions at leading order, NLO and NNLO in  $\alpha_s$  calculated by the FEWZ generator. The given uncertainty is calculated for the NNLO cross-section and includes PDF- and scale-uncertainties.

Process PDF-Set	LO in $\mathcal{O}(\alpha_s)$ MSTW2008LO	NLO in $\mathcal{O}(\alpha_s)$ MSTW2008NLO	NNLO in $\mathcal{O}(\alpha_s)$ MSTW2008NNLO	NNLO in $\mathcal{O}(\alpha_s)$ CT10	Uncertainty
$\sigma(pp \rightarrow Z + X) \times BR(Z \rightarrow l^+ l^-)$ [nb]	0.753	0.931	0.960	0.991	0.05
$\sigma(pp \rightarrow W^+ + X) \times BR(W^+ \rightarrow l^+ \nu)$ [nb]	4.80	5.80	5.98	6.16	0.3
$\sigma(pp \rightarrow W^- + X) \times BR(W^- \rightarrow l^- \nu)$ [nb]	3.27	4.06	4.20	4.30	0.2
$\sigma(pp \rightarrow W^\pm + X) \times BR(W^\pm \rightarrow l^\pm \nu)$ [nb]	8.11	9.86	10.18	10.46	0.3

an important test of perturbative QCD but also of the fundamental properties of the electroweak sector, as described in more detail in the following paragraphs. The discussion starts with two definitions of rest frames that allow for the definition of the angle  $\theta$  in proton-proton collisions (Section 2.8.1). Then the general form of the differential Drell-Yan cross-section is introduced in Section 2.8.2, while the interpretation of the corresponding angular coefficients is discussed in Section 2.8.3.

### 2.8.1 Collins-Soper and helicity frame

The direction of the incoming particles and anti-particles is known in an  $e^+e^-$  collider and hence the reference axis for the definition of the angle  $\theta$  can be defined in a straightforward way. The situation is very different at a proton-proton

collider such as the LHC. Since the vector boson originates from a  $q\bar{q}$  annihilation, a natural choice would be the direction the incoming quark but this can not be done for two reasons. First, the direction of the incoming quark is not known at the LHC. Second, the incoming partons are subject to initial-state radiation, which leads to a non-negligible transverse momenta,  $p_T$ , of the vector boson when annihilating that can not be determined for the two interacting partons.

To overcome these problems, the rest frame of the vector boson is typically chosen as rest frame in which the angular distributions of the decay leptons is measured. However, the definition of the axes in this rest frame is still ambiguous. To minimise the effect due to the lack of information about the kinematics of the incoming partons, the polar axis can be

defined in the rest frame of the vector boson, such that it is bisecting the angle between the momentum of the incoming protons. The y-axis can then be defined as the normal vector to the plane spanned by the two incoming protons and the x-axis is chosen such that a right-handed Cartesian coordinate system is defined (Figure 12). The resulting reference frame is called Collins-Soper (CS) frame [102].

When measuring  $\theta$  in an analogous way as in an  $e^+e^-$  collision, the direction of the incoming quark and antiquark must also be known but cannot be inferred on an event-by-event basis. However, this can be addressed on a statistical basis. Vector bosons with a longitudinal momentum  $p_z(V)$  have been produced by partons which have significantly different Bjorken- $x$  values. Figure 10 illustrates that large  $x$ -values enhance the probability for having valence quarks in the interaction and therefore the corresponding antiquark can be associated to the smaller  $x$ -values. Hence the measurement of  $p_z(V)$  allows us to assign the longitudinal quark and antiquark directions on a statistical basis. It should be noted that large  $p_z(Z)$  values also imply large rapidities and therefore the statistical precision for the correct quark/antiquark assignment is enhanced for  $Z$  bosons in the forward region.

In summary, the angle  $\theta$  can be expressed in the CS frames as

$$\cos \theta_{CS}^* = \frac{p_z(V)}{|p_z(V)|} \cdot \frac{2(p_1^+ p_2^- - p_1^- p_2^+)}{m_{ll} \sqrt{m_{ll}^2 + p_T(ll)^2}}, \quad (25)$$

with  $p_{1/2}^\pm = 1/\sqrt{2} \cdot (E_{1/2} \pm p_{z,1/2})$ , where  $E$  and  $p_z$  are the energy and longitudinal momenta of the first and second lepton. The first term of this equation defines the sign and hence the direction of the incoming quark. As previously discussed, large rapidities enhance the probability for a correction assignment of the direction. The second term of the equation corrects for the measured boost due to the hadronic recoil of the event and defines an average angle between the decay leptons and the quarks.

While angular measurements of the  $Z$  boson decays are usually done in the CS frame, measurements of the  $W$  boson are traditionally performed in the so-called helicity frame. The helicity frame is also chosen to be the rest frame of the vector boson. The z-axis is defined along the  $W$  laboratory direction of flight and the x-axis is defined orthogonal in the event plane, defined by the two protons, in the hemisphere opposite to the recoil system. The y-axis is then chosen to form a right-handed Cartesian coordinate system as shown in Figure 12.

## 2.8.2 Differential cross-section of the Drell-Yan process

The general form of the differential cross-section of the Drell-Yan process  $pp \rightarrow Z(W) + X \rightarrow l^+ l^- (l\nu) + X$  can be decomposed as [103], [104]

$$\begin{aligned} \frac{d\sigma}{dp_T^2 dy d\cos\theta d\phi} = & \frac{d\sigma_{unpol}}{dp_T^2 dy} \cdot ((1 + \cos^2\theta) \\ & + A_0 \frac{1}{2} (1 - 3\cos^2(\theta)) \\ & + A_1 \sin(2\theta) \cos(\phi) \\ & + A_2 \frac{1}{2} \sin^2(\theta) \cos(2\phi) \\ & + A_3 \sin(\theta) \cos(\phi) \\ & + A_4 (\cos\theta) \\ & + A_5 \sin^2(\theta) \sin(2\phi) \\ & + A_6 \sin(2\theta) \sin(\phi) \\ & + A_7 \sin(\theta) \sin(\phi)), \end{aligned} \quad (26)$$

where  $\theta$  and  $\phi$  are the polar and azimuthal angles of the charged lepton in the final state<sup>2</sup> in the CS frame to the direction of the incoming quark/antiquark. This decomposition is valid in the limit of massless leptons in a 2-body phase space and helicity conservation in the decay.

While the functional dependence of Equation 26 on  $\theta$  and  $\phi$  is independent on the reference frame chosen, the parameters  $A_i$  are frame dependent. When no cuts on the final-state kinematics are applied, the parameters  $A_i$  can be transformed from one reference frame to another. Due to the limited detector coverage and additional analysis requirements on the kinematics, the coefficients exhibit an experiment-dependent kinematic behaviour. Hence the optimal choice of the reference frame will differ for each analysis.

The angular coefficients  $A_i$  are functions of the vector boson kinematics, i.e. its transverse momentum,  $p_T(V)$ , its rapidity,  $Y_V$ , and  $m_V$  and contain information about the underlying QCD dynamics. They are subject to modifications from higher-order perturbative and non-perturbative corrections, structure functions and renormalisation and factorisation scale uncertainties. Since the PDFs of the proton impact the vector boson kinematics, the coefficients  $A_i$  also depend indirectly on the PDFs themselves. The 1-dimensional angular distributions can be obtained by integrating either over  $\cos\theta$  or  $\phi$ , leading to

$$\frac{d\sigma}{\cos\theta} \sim (1 + \cos^2\theta) + \frac{1}{2} A_0 (1 - 3\cos^2\theta) + A_4 \cos\theta \quad (27)$$

$$\begin{aligned} \frac{d\sigma}{\cos\phi} \sim & 1 + \frac{2\pi}{16} A_3 (\cos^2\phi) + \frac{1}{4} A_2 (\cos(2\phi)) + \\ & + \frac{3\pi}{16} A_7 \sin\phi + \frac{1}{4} A_5 \sin(2\phi) \end{aligned} \quad (28)$$

<sup>2</sup>For measurements of the  $Z$  the negative lepton is used.

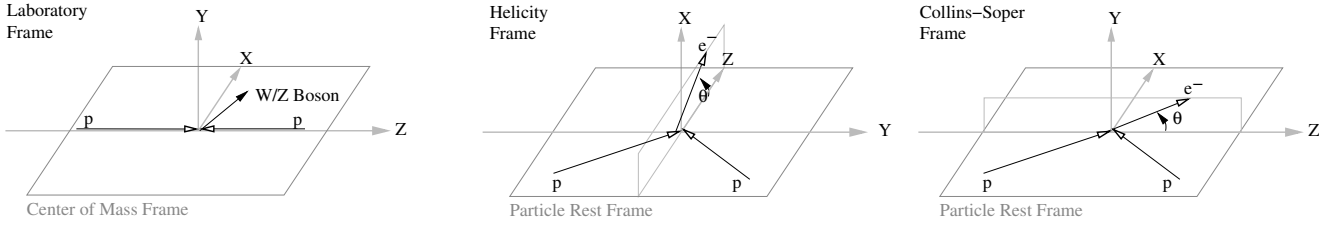


**Fig. 12** Center-of-mass frame (left), helicity frame (middle) and Collins-Soper frame (right)

which can be used to extract several coefficients independently in the case of small data samples.

### 2.8.3 Interpretation of coefficients

The  $(1 + \cos^2 \theta)$  term in Equation 26 comes from the pure leading-order calculation of the vector boson production and decay. The terms corresponding to the coefficients  $A_0, A_1, A_2$  are parity conserving, while the terms  $A_3$  to  $A_7$  are parity violating. The  $A_0$  to  $A_4$  coefficients receive contributions from the QCD theory at leading and all higher orders, while the parameters  $A_5, A_6$  and  $A_7$  appear only in NLO QCD calculations and are typically small. Several studies have been published which discuss and predict these coefficients for hadron colliders [105].

It should be noted that all terms except of  $A_4$  are symmetric in  $\cos \theta$ . In the case of the  $Z/\gamma^*$  exchange,  $A_4$  appears also in leading-order calculations as it is directly connected to the forward backward asymmetry  $A_{fb}$  via

$$A_{fb} = \frac{3}{8} A_4 \quad (29)$$

which will be discussed in more detail in Section 6.5.

The  $A_4$  parameter also plays a special role in the case of  $W$  boson polarisation measurements. As discussed in the previous section, vector bosons tend to be boosted in the direction of the initial quark. In the massless quark approximation, the quark must be left-handed in the case of the  $W$  boson production and as a result  $W$  bosons with large rapidities are expected to be purely left-handed. For more centrally produced  $W$  bosons, there is an increasing probability that the antiquark carries a larger momentum fraction and hence the helicity state of the  $W$  bosons becomes a mixture of left- and right-handed states. The respective proportionals are labelled with  $f_L$  and  $f_R$ . For  $W$  bosons with a larger transverse momenta, the production via a gluon in the initial or final state becomes relevant, e.g. via  $u\bar{d} \rightarrow W^+ g$ . Hence the vector nature of the gluon has to be taken into account in the prediction of the production mechanisms. For high transverse momenta, also polarisations in the longitudinal state of the  $W$  bosons can appear. This fraction is denoted by  $f_0$  and is directly connected to the massive character of the gauge bosons. The helicity fractions  $f_L, f_R$  and  $f_0$  can be directly connected to the coefficients  $A_0$  and  $A_4$  via

$$f_L(Y_W, p_T^W) = \frac{1}{4}(2 - A_0(Y_W, p_T^W)) \mp A_4(Y_W, p_T^W) \quad (30)$$

$$f_R(Y_W, p_T^W) = \frac{1}{4}(2 - A_0(Y_W, p_T^W)) \pm A_4(Y_W, p_T^W) \quad (31)$$

$$f_0(Y_W, p_T^W) = \frac{1}{2} A_0(Y_W, p_T^W), \quad (32)$$

where the upper (lower) signs correspond to  $W^+$  ( $W^-$ ). In particular, the difference of  $f_L$  and  $f_R$  depends only on  $A_4$  as

$$f_R - f_L = \pm \frac{1}{2} A_4. \quad (33)$$

The coefficients  $A_0$  and  $A_2$  also play a particular role in the angular decay distributions, as they are related via the Lam-Tung relation [106]. This relation states that  $A_0(p_T)$  and  $A_2(p_T)$  are identical for all  $p_T$  if the spin of the gluon is one. In case of a scalar gluon, this relation would be broken. It should be noted that the test of this relation is therefore not a test of QCD theory, but a consequence of the rotational invariance of decay angles and the properties of the quark-coupling to  $Z/\gamma^*$  and the  $W$  boson. At the  $Z$ -pole, the leading-order predictions of the  $p_T$  dependence of  $A_{0/2}$  for a gluon of spin one are given by [107–109]

$$A_{0,2} = \frac{p_T^2}{p_T^2 + m_Z^2} \quad (34)$$

for the process  $q\bar{q} \rightarrow Z g$  and by

$$A_{0,2} = \frac{5 \cdot p_T^2}{5 \cdot p_T^2 + m_Z^2} \quad (35)$$

for the process  $qg \rightarrow Z q$ . NLO order corrections do not impact  $A_0$  significantly, while  $A_2$  receives contributions up to 20%.

## 3 Detectors and Data

### 3.1 The LHC and the data collected at $\sqrt{s} = 7$ TeV

From March 2010 to October 2011, the Large Hadron Collider [110] delivered proton-proton collisions at a center-of-mass energy of  $\sqrt{s} = 7$  TeV to its four main experiments

**Table 3** Parameters of the LHC at the end of 2010 and the end of 2011 including an estimate of the average number of interactions per bunch-crossing [115].

Parameter	2010	2011
$\sqrt{s}$	7 TeV	7 TeV
$N(10^{11} p/b)$	1.2	1.5
$k(n_{bunches})$	368	1380
Bunch Spacing (ns)	150	50
$L (cm^{-2}s^{-1})$	$2 \cdot 10^{32}$	$3.6 \cdot 10^{33}$
Average pp-interactions per bunch-crossing	$\approx 1.2$	$\approx 10 - 15$

**Table 4** Overview of recorded integrated luminosity in 2010 and 2011 by the ATLAS and CMS experiments. Also shown is the integrated luminosity which is used for physics analyses.

Experiment	$\int \mathcal{L} dt$ (2010)		$\int \mathcal{L} dt$ (2010)	
	recorded	used	recorded	used
ATLAS	$45 pb^{-1}$	$35 pb^{-1}$	$5.08 fb^{-1}$	$4.6 fb^{-1}$
CMS	$40.8 pb^{-1}$	$36 pb^{-1}$	$5.55 fb^{-1}$	$4.5-4.8 fb^{-1}$

ATLAS [111], CMS [112], LHCb [113] and ALICE [114]. The primary LHC machine parameters at the end of the data taking in 2010 and 2011 are given in Table 3. From 2010 to 2011, the number of circulating proton bunches was increased by a factor of 3.8, the spacing between two bunches was decreased from 150 ns to 50 ns and the beam-focus parameter  $\beta^*$  was reduced by a factor of 3.5. This resulted in a significant increase of instantaneous luminosity from  $L = 2 \times 10^{32} cm^{-2}s^{-1}$  in 2010 to  $L = 3.7 \times 10^{33} cm^{-2}s^{-1}$  in 2011 [115].

The total integrated luminosity delivered to the experiments was  $L \approx 44 pb^{-1}$  in 2010 and  $L \approx 6.1 fb^{-1}$  in 2011. The data taking efficiency of ATLAS and CMS, when the detector and data-acquisition systems were fully operational, was above 90% for both years. The recorded integrated luminosity, which was used as the data samples for the published physics analyses for ATLAS and CMS in 2010 and 2011, is shown in Table 4 together with their respective relative uncertainties.

The precise knowledge of the recorded integrated luminosity is a crucial aspect for all cross-section measurements. The Van der Meer methods [116], [117] was applied in total three times in 2010 and 2011 to determine the luminosity for ATLAS and CMS, leading to relative uncertainties below 2%. It should be noted that the luminosity determination is highly correlated between ATLAS and CMS, leading to correlated uncertainties in the corresponding cross-section measurements.

The change in the machine settings from 2010 to 2011 leads to an increase of *pile-up* noise, which is the occurrence of several independent, inelastic proton-proton collisions during one or more subsequent proton-proton bunch

crossings. These additional collisions can lead to a significant performance degradation of some observables which are used in physics analysis. The *in-time* pile-up, i.e. the additional collisions occurring within the same bunch crossing, can be described by the number of reconstructed collision vertices  $N_{vtx}$  in one event. The *out-of-time* pile-up is due to additional collisions from previous bunch crossings, that can still affect the response of the detector, in particular calorimeters, whose response time is larger than two subsequent bunch crossings. The number of interactions per crossing is denoted as  $\mu$  and can be used to quantify the overall pile-up conditions. On average, there is roughly a linear relationship between  $\mu$  and  $N_{vtx}$ , i.e.  $\langle N_{vtx} \rangle \approx 0.6 \langle \mu \rangle$ . In 2010, the average number of interactions per collision was  $\mu = 2$ . The first  $\int \mathcal{L} dt \approx 1 fb^{-1}$  in 2011 had  $\langle \mu \rangle \approx 6$ , while  $\langle \mu \rangle$  of greater than 15 was reached by the end of 2011. This affects several systematic uncertainties related to precision measurements at the LHC.

### 3.2 Coordinate system

The coordinate system of the ATLAS and CMS detectors are orientated such that the z-axis is in the beam direction, the x-axis points to the center of the LHC ring and the y-axis points vertically upwards (Figure 13). The radial coordinate in the x-y plane is denoted by  $r$ , the azimuthal angle  $\phi$  is measured from the x-axis. The pseudorapidity  $\eta$  for particles coming from the primary vertex is defined as  $\eta = -\log \frac{\theta}{2}$ , where  $\theta$  is the polar angle of the particle direction measured from the positive z-axis. The transverse momentum  $p_T$  is defined as the transverse momentum component to the beam direction, i.e. in the x-y-plane. The transverse energy is defined as  $E_T = E \sin \theta$ .

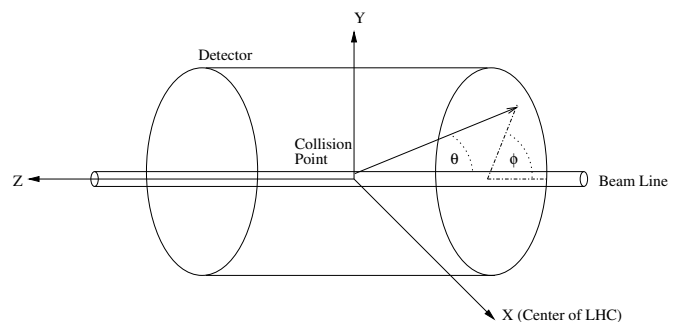


**Fig. 13** Illustration of the ATLAS and CMS coordinate system.

### 3.3 The ATLAS detector

The "A Toroidal LHC ApparatuS" (ATLAS) detector is one of the two general purpose detector at the LHC. It has a symmetric cylinder shape with nearly  $4\pi$  coverage (Figure 14).



ATLAS has a length of 45m, a diameter of 25m and weighs about 7,000 tons. It can be grouped into three regions: the barrel region in the center of the detector and two end-cap regions which provide coverage in the forward and backward direction with respect to the beam-pipe. ATLAS consists of one tracking, two calorimeter and one muon system, which are briefly described below. A detailed review can be found in [111].

The tracking detector is the closest to the LHC beam pipe and extends from an inner radius of 5cm to an outer radius of 1.2m. It measures tracking information of charged particles in a 2T axial magnetic field provided by a superconducting solenoid magnet system. In addition, the tracking detector provides vertex information, which can be used to identify the interaction point of proton-proton collision and the decay of short-lived particles. Three technologies are used. The innermost part of the tracking detector consists of three silicon pixel detector layers. Each pixel has a size of  $50 \times 400 \mu\text{m}$ , leading in total to 80 million readout channels. The pixel detector provides tracking information up to a pseudorapidity of  $|\eta| = 2.5$ . The same region is also covered by the semi-conductor tracker, which surrounds the pixel detector. It consists of narrow silicon strips in the size of  $80 \mu\text{m} \times 12 \text{cm}$ , which are ordered in four double layers. The outermost part of the tracking detector is the transition radiation tracker which uses straw detectors and covers an area up to  $|\eta| = 2.0$ . It provides up to 36 additional measurement points of charged particles with a spatial resolution of  $200 \mu\text{m}$ . In addition, the produced transition radiation can be used for electron identification.

In the electromagnetic (EM) calorimeter of ATLAS, the energy of incoming electrons and photons is fully deposited to the detector materials and can be precisely determined. Moreover, the ATLAS calorimeter can measure the location of the deposited energy to a precision of 0.025rad. Liquid argon is used as active material, while lead plates act as absorbers. The absorbers are arranged in an accordion shape which ensures a fast and uniform response of the calorimeter. The barrel region covers a range up to  $|\eta| < 1.475$ , the two endcaps provide coverage for  $1.375 < |\eta| < 3.2$ . A pre-sampler detector is installed in the region up to  $|\eta| < 1.8$ , which is used to correct the energy loss of electrons and photons in front of the calorimeter.

The hadronic calorimeter ranges from  $r = 2.28 \text{m}$  to  $r = 4.23 \text{m}$  and measures the full energy deposition of all remaining hadrons. The barrel part is the so-called tile calorimeter and covers a region up to  $|\eta| < 1.0$ . An extended barrel detector is used for the region  $0.8 < |\eta| < 1.7$ . Scintillating plastic tiles are used as active medium. Iron plates act not only as absorber material, but also as the return yoke for the solenoid magnetic field of the tracking detector. The granularity of  $\Delta\phi \times \Delta\eta = 0.1 \times 0.1$  determines the position information of the measured energy deposits, which is roughly

0.1 rad. The hadronic endcap calorimeter covers a pseudorapidity range from  $1.5 < |\eta| < 3.5$ , where liquid argon is used as the ionisation material and copper as the absorber. The very forward region from  $3.1 < |\eta| < 4.5$  is covered by the forward calorimeters, which also uses liquid argon with copper and tungsten as absorbers. Electrons and photons are also detected in the forward calorimeters, as no dedicated electromagnetic calorimeter is present in that region.

The muon spectrometer is not only the largest part of the ATLAS Experiment, ranging from  $r = 4.25 \text{m}$  to  $r = 11.0 \text{m}$ , but also its namesake. Three air-core toroidal magnets provide a toroidal magnetic field with an average field strength of 0.5T. Muons with an energy above  $\approx 6 \text{GeV}$  that enter the toroidal magnetic field will be deflected. This deflection is measured in three layers of tracking chambers. In the barrel-region ( $|\eta| < 1.0$ ) and partly in the endcaps up to  $|\eta| < 2.0$ . Monitored drift-tube chambers provide the precise tracking information of incoming muons. For  $2.0 < |\eta| < 2.7$ , cathode strip chambers with a higher granularity are used. The trigger-system of the muon spectrometer is based on resistive plate chambers in the barrel region and by thin gap chambers in the endcap. Since the ATLAS muon system is filled with air, effects from multiple scattering are minimised. In addition, the long bending path of the muons provides an accurate measurement of their momentum.

The trigger system of the ATLAS detector has three levels. The first level is a hardware based trigger, which uses a reduced granularity information of the calorimeters and the muon system. It defines so-called regions-of-interest, in which possible interesting objects have been detected, and reduces the event rate to  $\approx 75 \text{kHz}$ . The second level trigger is software based and has the full granularity information within the region-of-interest and the inner detector information. By this system, the rates are reduced to 1kHz. The last trigger level has access to the full event information with full granularity and uses reconstruction algorithms that are the same or similar to those used in the offline reconstruction. The final output rate is  $\approx 400 \text{Hz}$ .

### 3.4 The CMS detector

The Compact Muon Solenoid (CMS) detector is the second general purpose detector at the LHC with a similar design as the ATLAS detector. It offers also a nearly full  $4\pi$  coverage which is achieved via one barrel and two endcap sections (Figure 15). CMS is 25 m long, has a diameter of 15 m and weighs 12500 tons. Most of its weight is due to its name-giving solenoid magnet, which provides a 3.8 T magnetic field. The magnet is 12.5 m long with a diameter of 6 m and consists of four layers of superconducting niobium-titanium at an operating temperature of 4.6 K. The CMS tracking system as well as the calorimeters are within the solenoid, while the muon system is placed within the iron return yoke. We

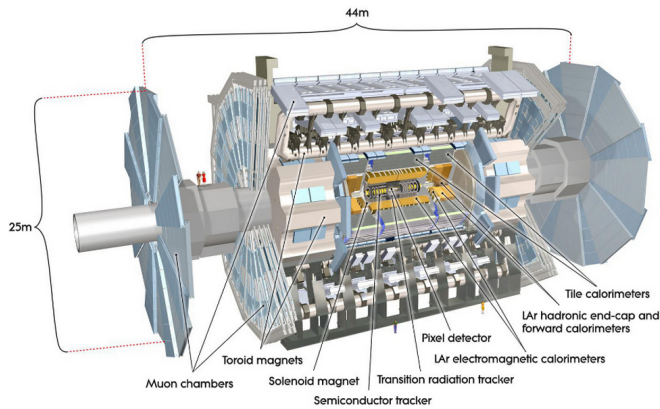


Fig. 14 ATLAS Experiment

briefly discuss the four main detector systems of CMS below; a detailed description can be found in [112].

The inner tracking system of CMS is used for the reconstruction of charged particle tracks and is fully based on silicon semi-conductor technology. The detector layout is arranged in 13 layers in the central region and 14 layers in each endcap. The first three layers up to a radius of 11cm consist of pixel-detectors with a size of  $100\mu\text{m} \times 150\mu\text{m}$ . The remaining layers up to a radius of 1.1 m consist of silicon strips with dimensions  $100\mu\text{m} \times 10\text{cm}$  and  $100\mu\text{m} \times 25\text{cm}$ . In total, the CMS inner detector consists of 66 million readout-channels of pixels and 96 million readout channels of strips, covering an  $\eta$ -range of up to 2.5.

The CMS electromagnetic calorimeter is constructed from crystals of lead tungstate ( $\text{PbWO}_4$ ). The crystalline form together with oxygen components in  $\text{PbWO}_4$  provide a highly transparent material which acts as a scintillator. The readout of the crystals is achieved by silicon avalanche photodiodes. The barrel part of the EM calorimeter extends to  $r = 1.29\text{m}$  and consists of 61200 crystals (360 in  $\phi$  and 170 in  $\eta$ ), covering a range of  $|\eta| < 1.479$ . The EM calorimeter endcaps are placed at  $z = \pm 3.154\text{m}$  and cover an  $\eta$ -range up to 3.0 with 7324 crystals on each side. A pre-shower detector is installed in order to discriminate between pions and photons.

The hadronic calorimeter of the CMS detector is a sampling calorimeter which consists of layers of brass or steel as passive material, interleaved with tiles of plastic scintillator. It is split in four parts. The barrel part ( $|\eta| < 1.3$ ) consists of 14 brass absorbers and two stainless steel absorbers as the innermost and outermost plates. The granularity is  $0.087 \times 0.087$  in the  $\eta, \phi$ -plane. Due to the space limitations from the solenoid, an outer calorimeter has been installed. It consists of two scintillators at  $r = 3.82\text{m}$  and  $r = 4.07\text{m}$  with 12.5 cm steel in between. The endcap calorimeters cover  $1.3 < |\eta| < 3.0$  and are made of 18 layers of 77 mm brass plates interleaved by 9 mm scintillators. The  $\eta$ -

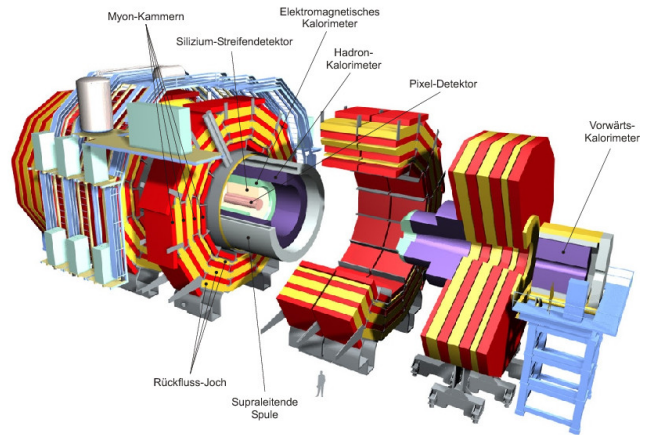


Fig. 15 CMS Experiment

region from  $3.0 < |\eta| < 5.0$  is covered by forward calorimeters, positioned at  $z = \pm 11\text{m}$ . They will also register the energy deposits of electrons and photons in this rapidity range.

The barrel and endcap parts of the CMS muon system consist of four layers of precision tracking chambers. The barrel part covers a range up to  $|\eta| = 1.3$  and drift-tube chambers are used for the tracking. The tracking information in both endcaps ( $0.9 < |\eta| < 2.4$ ) is provided by cathode strip chambers. The muon triggers are based on resistive plate chambers, similar to the ATLAS experiment [118].

The CMS trigger system has two levels. The first level trigger is hardware based and uses coarsely segmented information from the calorimeters and the muon system. It reduces the rate to 100 kHz. The second level trigger, called the high-level trigger, is a software-based trigger system which is based on fast reconstruction algorithms. It reduces the final rate for data-recording down to 400 Hz.

### 3.5 Reconstructed objects

Measurements of single vector boson production using ATLAS and CMS data involve in general five primary physics *objects*. These objects are electrons, photons, muons, neutrinos, whose energy can only be inferred, and particle jets, which originate from hadronised quarks and gluons. An overview of the ATLAS and CMS detector performance for several physics objects is summarised in Table 5.

#### 3.5.1 Electron, photon and muon reconstruction

Electrons candidates are identified by requiring that significant energy deposits in the EM calorimeter, which are grouped to so-called electromagnetic clusters, exist and that there is an associated track in the tracking detector. The transverse momenta of the electrons are calculated from the energy measurement in the EM calorimeter and the track-direction

information is taken from the tracking detector. A series of *quality cuts* are defined to select electron candidates. These cuts include cuts on the shower-shape distributions in the calorimeter, track-quality requirements and the track-matching quality to the clusters. Stringent cuts on these quantities ensure a good rejection of non-electron objects, such as particle jets faking electron signatures in the detector. ATLAS has three different quality definitions for electrons, named *loose*, *medium* and *tight* [119] and CMS analyses use two definitions, called *loose* and *tight* [120].

For some analyses in both ATLAS and CMS, electron clusters in the transition region between the barrel and end-cap sections are rejected, as cables and services in this detector region lead to a lower quality of reconstructed clusters. These regions are defined as  $1.37 < |\eta| < 1.52$  and  $1.44 < |\eta| < 1.57$  in ATLAS and CMS respectively. Electron candidates in the forward region from  $2.5 < |\eta| < 4.9$  (used by some ATLAS analyses) have no associated track information and therefore their identification is based solely on the shower-shape information.

Photons candidates are reconstructed by clustered energy deposits on the EM calorimeter in a range of  $|\eta| < 2.37$  and  $|\eta| < 2.5$  for ATLAS [119] and CMS [120], respectively, as well as specific shower shape cuts. If no reconstructed track in the tracking detector can be associated to the electromagnetic cluster, then the photon candidate is marked as an *unconverted photon candidate*. If the EM cluster can be associated to two tracks, which are consistent with a reconstructed conversion vertex, the candidate is defined as a *converted photon candidate*.

Muon candidates are identified by one reconstructed track in the muon spectrometer. *Combined muons* are required to have in addition an associated track in the tracking detector. The measured 4-momenta, in particular the transverse momenta, of combined muons are based on a statistical combination of the independent measurements within the tracking and muon detectors or a complete refit of all available parameters. For the measurements presented here, the momentum resolution for muons is dominated by the information from the tracking detector for both experiments. CMS can reconstruct muons within  $|\eta| < 2.4$  [121], while the ATLAS muon spectrometer reaches  $|\eta| < 2.7$  [122]. However, muons that are reconstructed beyond  $|\eta| > 2.5$ , have no associated information from the tracking detector available and therefore only kinematic information from the muon spectrometer can be used. ATLAS analyses therefore often restrict the muon range to  $|\eta| < 2.4$ .

In many single vector boson measurements, the leptons are required to be isolated meaning that there is no significant energy deposited around the lepton itself. Requiring isolation greatly reduces the number of particle jets which are misreconstructed as electron, photons or muons.

Isolation can be defined in several ways. First, a tracking-based isolation can be used that is defined as

$$p_T^{iso} = \sum_i^{\Delta R(\eta,\phi) < 0.3} p_T^i / p_T^{lepton}, \quad (36)$$

where  $i$  indicates the sum over all reconstructed tracks in the tracking detector with an energy above a given threshold and within a cone-radius of 0.3 in the  $(\eta, \phi)$ -plane. The track from the lepton candidate itself is not considered. This quantity can be normalised by the transverse momentum of the lepton candidate, which ensures a more stable isolation definition for larger transverse momenta. A similar definition can be made using the EM calorimeter, i.e.

$$E_T^{iso} = \sum_i^{\Delta R(\eta,\phi) < 0.3} E_T^i / E_T^{lepton}, \quad (37)$$

where  $i$  runs over all EM clusters within  $\Delta R < 0.3$  that are not associated to the reconstructed lepton. ATLAS uses both, tracking- and calorimeter-based isolation criteria as defined above. CMS uses similar isolation variables, but in addition applies non-normalised isolation definitions based on tracks or energies in the hadronic calorimeter.

### 3.5.2 Hadronic jets and missing energy reconstruction

Hadronised partons are detected as particle jets in the EM and hadronic calorimeters. To reconstruct particle jets in ATLAS, the energy deposits are merged to topological clusters in a pseudorapidity range of  $|\eta| < 4.9$ . Clusters are seeded by calorimeter cell deposits with a four sigma deviation from the noise level. An anti- $k_T$  algorithm [123] is then used to reconstruct the clusters into jets. The typical ATLAS distance parameter of the jet definition is  $R = 0.4$ . In addition it is often required that the distance between leptons and jets in the  $(\eta, \phi)$ -plane of the detector satisfies the condition  $\Delta R(l, jet) > 0.3$  to avoid double counting [124]. The jet energy and direction is corrected for effects like additional dead material in the detector, the difference in energy response in the calorimeter to hadronic versus EM interactions, the loss of energy outside the jet radius and the presence of energy from pile-up interactions [124]. For CMS analyses, where the detector features a superior tracking system but offers a less precise calorimetry system, the so-called particle flow technique [125] is used. This method combines information from all detector systems, in particular the calorimeter and the tracking detector and aims to identify all particles in mutual exclusive categories: muons, electrons, including the identification of bremsstrahlung photons, converted and unconverted photons, charged and uncharged hadrons. Thus, a full event description of each particle is attempted. This event description is used as input to an anti- $k_T$  algorithm with a typical distance parameter of

$R = 0.5$ . The jet energy and direction is also corrected for effects like the presence of pile-up and the non-compensation of the calorimeter [126].

Both experiments have dedicated algorithms to identify particle jets originating from  $b$ - and  $c$ -quarks. These algorithms combine information about the impact parameter significance of tracks with the expected topology of semileptonic  $b$ - or  $c$ -decays [127].

The energy of neutrinos, which leave the detector unseen, must be inferred through *missing energy*. While the initial collision energy in beam direction of the partons that are involved in the hard scattering process is not known at hadron colliders, the vector sum of all transverse momenta and energies in the initial state must be zero. Due to energy and momentum conservation, this must also hold for all final state objects in the transverse plane, defined as

$$\mathbf{0} = \sum_i \mathbf{E}_{T,i}^{calo} + \sum_i \mathbf{p}_{T,i}^\mu + \sum_i \mathbf{p}_{T,i}^\nu, \quad (38)$$

where the first term corresponds to the vector sum of all transverse energy deposits in the calorimetric system, the second term corresponds to the transverse momenta of the muons reconstructed by the muon systems and the last term corresponds to the transverse momentum sum of all neutrinos in the final state. The latter term is called the missing energy,  $\mathbf{E}_T^{\text{miss}} = -\sum_i \mathbf{E}_{T,i}^{calo} - \sum_i \mathbf{p}_{T,i}^\mu$  and its absolute value is called missing transverse energy  $E_T^{\text{miss}}$ .

The ATLAS measurement of  $E_T^{\text{miss}}$  uses all electromagnetic and hadronic energy clusters up to  $|\eta| = 4.9$ . Cells which are associated with a particle jet are calibrated with a hadronic energy scale correction, while cells associated to electromagnetic showers are calibrated via the electromagnetic energy scale [124]. The CMS measurement of  $E_T^{\text{miss}}$  follows similar lines, but again uses the information provided by the particle flow algorithms to improve the measurement [125].

### 3.6 Detector simulation and calibration

A detailed simulation of the ATLAS and CMS detector response has been developed over recent years. Both simulations are based on the GEANT4 package [129], which offers the possibility to describe the interaction of all final-state particles with the detectors at a microscopic level. In a second step, the digitisation of the simulated detector interactions is performed and the nominal data reconstruction algorithms are applied.

Several methods are used to calibrate the detector and to compare data to the simulated events. One important calibration for lepton and jet reconstruction is based on the study of the leptonic decays of the  $Z$  boson, which will be briefly summarised in the following. More details on lepton and jet calibration can be found in [126], [124].

The lepton reconstruction and identification efficiencies can be determined in data via the *tag-and-probe method*. This method makes use of well known decay properties of a resonance, e.g. the  $Z$  boson, into two well identified particles. One particle is selected with a strict selection (the *tag*) to obtain a low background rate. The second particle (the *probe*) is required to only pass loose selection cuts and can then be used to determine the selection efficiency for tighter requirements.

A simple example is the reconstruction efficiency of muons in the muon spectrometer. The  $Z$  boson decays into two muons, resulting in two oppositely charged tracks in the tracking and muon detectors. The tag object is required to have a track in both detector systems. The probe object is required to have only a track in the tracking detector which forms an invariant mass close to the  $Z$  boson mass. This ensures a rather clean sample of  $Z$  boson events in the muon decay channel. The corresponding reconstruction efficiency can be determined by testing if a matching track to the probe can be found.

Since the  $Z$  boson mass and width is precisely known from the LEP experiments, it can also be used to calibrate the energy scale and resolution of leptons. Here, the invariant mass spectra of the leptonic  $Z$  boson decays are compared in data and simulations. The peak of the mass distribution is sensitive to the lepton energy/momentum scale, while the width of the distributions gives a handle on the energy and momentum resolutions.

The production of the  $Z$  boson also offers the possibility to calibrate the energy scale of particle jets and the hadronic activity in the calorimeters.  $Z$  bosons which are produced with large transverse momenta must balance this momenta with additional partons in the final state. The transverse momenta of the  $Z$  boson can be reconstructed rather precisely by the 4-momentum measurements of its decay leptons. This transverse momentum must be balanced by reconstructed particle jets, or to be more general, by the total measured hadronic activity. Hence the energy scale and the resolution of particle jets can be calibrated in data.

It should be noted that these methods rely on the available statistics of the corresponding control samples, e.g. on the available number of recorded  $Z$  boson events in the leptonic decay channel. While the uncertainties on the detector calibration are usually treated as systematic uncertainties in the physics analyses, they have a significant statistical component which can be reduced by studying more data. Analyses which are based on the 2010 data have therefore significant larger uncertainties due to the limited statistics of the calibration samples.

**Table 5** Reconstruction performance of electrons, muons and particle jets of the ATLAS and CMS experiment. The reconstruction efficiency and momentum/energy resolutions are shown for the kinematic ranges defined. Further details can be found in the references given.

ATLAS					
Object	definition and algorithm	kinematic range	reconstruction efficiency	$p_T$ -resolution	Reference
Electron	medium quality definition	$ \eta  < 2.4$ $20 \text{ GeV} < E_T < 40 \text{ GeV}$	94% – 98%	$\approx 2\%$	[119]
Muon	combined tracking+muon	$ \eta  < 2.5$ $20 \text{ GeV} < p_T < 40 \text{ GeV}$	$\approx 95\%$	$\approx 2\%$	[122]
Jet	anti- $k_T$ ( $\Delta R = 0.4$ )	$ \eta  < 0.8, E_T = 100 \text{ GeV}$	100%	$\approx 10$	[124]
CMS					
Object	definition and algorithm	kinematic range	reconstruction efficiency	$p_T$ -resolution	Reference
Electron	medium, multivariate	$ \eta  < 1.479$ $20 \text{ GeV} < E_T < 40 \text{ GeV}$	75 – 85%	$\approx 3 - 4\%$	[128]
Muon	combined tracking+muon	$ \eta  < 1.2$ $20 \text{ GeV} < p_T < 40 \text{ GeV}$	$\approx 95\%$	$\approx 2\%$	[121]
Jet	anti- $k_T$ ( $\Delta R = 0.5$ )	$ \eta  < 0.5, E_T = 100 \text{ GeV}$	100%	$\approx 10$	[125]

#### 4 Production Cross Section Measurements at the LHC

For experimental measurements, the production cross-section is calculated via the following equation

$$\sigma_V^{incl} = \frac{N_{signal}}{\varepsilon \cdot BR \cdot \int \mathcal{L} dt} \quad (39)$$

The number of signal events is determined as  $N_{signal} = N_{data} - N_{bkg}$ , where  $N_{data}$  is the number selected events in data and  $N_{bkg}$  is the number of background events surviving the signal selection. The factor  $\varepsilon$  is the efficiency of the signal events passing the signal selection criteria. To correct the cross-section for the choice of a specific decay channel, a branching ratio factor,  $BR$  is applied. These ratios are known to a high accuracy for the gauge bosons from LEP experiments [35]. Finally,  $\int \mathcal{L} dt$  is the integrated luminosity, which is a measure of the size of the data sample used.

The efficiency correction factor  $\varepsilon$  is usually estimated with simulations of the signal process. These simulations include both a detailed description of the object reconstruction in the detector, called the *reconstruction level*, and the final-state particle information of the generator calculations, called the *generator level*. The same signal selection cuts as applied to the data can be applied to the simulated events at reconstruction level. However, the simulation do not model the data perfectly and these differences are corrected in the estimation of  $\varepsilon$ , following the methods described in Section 3.6. In addition, basic signal selection cuts, such as minimal  $p_T$  cut, can also be applied to the final-state particles at the generator level. The object value for the final-state particles though differs from the reconstructed quantity. Following these definitions,  $\varepsilon$  can be defined as the ratio of all events which pass the signal selection on reconstruction level  $N_{reco}^{selected}$  over the number of all generated events  $N_{gen}^{all}$ .

The efficiency correction  $\varepsilon$  can further be decomposed as the product of a fiducial acceptance,  $A$ , and a detector

induced- correction factor,  $C$ , i.e.  $\varepsilon = A \cdot C$ . The fiducial acceptance is the ratio of the number of events that pass the geometrical and kinematic cuts in the analysis on generator level ( $N_{gen}^{selected}$ ) over the total number of generated events in a simulated sample of signal process ( $N_{gen}^{all}$ ). These selection cuts on generator level usually require geometrical and kinematic constraints close to the cuts applied on the reconstructed objects, e.g. leptons in the final state should fulfil  $p_T > 20 \text{ GeV}$  and  $|\eta| < 2.5$ . The dominant uncertainties on the fiducial acceptance are the scale and PDF uncertainties.

The detector correction factor  $C$  is defined as the number of selected events in simulated sample ( $N_{reco}^{selected}$ ), which now includes a detailed simulation of the detector response, over the number of events in the fiducial phase space at generator level ( $N_{gen}^{selected}$ ). Hence the product of  $A \cdot C$  can be written as

$$\varepsilon = C \cdot A = \frac{N_{reco}^{selected}}{N_{gen}^{selected}} \cdot \frac{N_{gen}^{selected}}{N_{gen}^{all}} = \frac{N_{reco}^{selected}}{N_{gen}^{all}} \quad (40)$$

The uncertainties associated with the detector correction factor are dominated by experimental sources, such as limited knowledge of reconstruction or cut efficiencies and the accuracy of the energy/momentum measurements. This factor can be larger than unity due to migration effects from outside the fiducial region into the reconstructed sample. However, in practice this is rarely the case, as detector inefficiencies and the selection criteria on reconstructed objects reduce the number of events.

Defining  $\varepsilon$  as  $A \cdot C$  is convenient because if the definition of the fiducial volume used for  $N_{gen}^{selected}$  is close to the cuts applied to the data, this factorisation allows for a separation of theoretical and experimental uncertainties. The fiducial acceptance,  $A$ , is completely independent of the detector response whereas the detector correction factor,  $C$ , is largely independent of theoretical modelling uncertainties.

In many experimental measurements, the fiducial cross-section, defined as

$$\sigma_V^{fid.} = \frac{N_{data} - N_{bkg}}{C \cdot BR \cdot \int \mathcal{L} dt} = \sigma_V^{incl.} \cdot A, \quad (41)$$

is therefore used, as this definition is only affected to a small extent by theoretical uncertainties. Using fiducial cross-sections has the added benefit that experimental data can be more easily compared to future theory predictions with improved theoretical uncertainties. On the other hand, it should be noted that the theoretical predictions for fiducial cross-sections are also subject to sizeable PDF and scale uncertainties.

In addition to measurements of the inclusive cross-section, measurements of the cross-section as a function of one or more observables can also be made. For a given range of a single observable, this is expressed as

$$\frac{d\sigma_V^{fid.}}{dx} = \frac{N(\Delta x)_{data} - N(\Delta x)_{bkg}}{C(\Delta x) \cdot BR \cdot \int \mathcal{L} dt} \quad (42)$$

where  $x$  is the observable being measured,  $N(\Delta x)_{data}$ ,  $N(\Delta x)_{bkg}$  and  $C(\Delta x)$  are the same as defined above but for a specific range of  $x$ . Differential cross-section measurements allow for a comparison of distributions of the theoretical predictions to the data.

The challenge of measuring the differential cross-section is the transformation of the measured distribution, which is distorted by the limited resolution and efficiencies of the detector, to the underlying or true distribution. One possibility to infer the true distribution from the measurement is to directly use Equation 42, which is known as *bin-by-bin unfolding*. However, this method is only a valid approach if the *purity*, defined as the ratio of events which fall in the same range of  $\Delta x$  in both the reconstructed- and generator-level selections over the total number of events that have been generated in the range  $\Delta x$ , of the underlying distribution is high, typically above 90%. When the purity is low,  $C(\Delta x)$  can have large theoretical uncertainties, since simulations are the only means to estimate this migration between bins. To reduce these uncertainties, advanced unfolding methods have to be used. One widely used approach is Bayesian unfolding [130]. Here, the experimental detector effects are represented in a response matrix, whose elements are the probability of an event in the  $i$ -th bin at generator level to be reconstructed in the  $j$ -th bin at reconstruction level. The bin size is chosen to be wider than the detector resolution effects, aiming at a purity of  $> 60\%$ . In the first iteration, the response matrix is derived from simulations. It is then multiplied to the measured spectrum, resulting in a first unfolded spectrum of the data. For the  $n$ -th iteration, the response matrix is reweighted to the unfolded spectrum of step  $n - 1$  in order to minimise the bias of the initial prediction. Thus the unfolded spectrum becomes insensitive to the original prior. Other unfolding techniques, such as matrix inversion or single value decomposition [131], are also used.

## 5 Event Selection and Background Estimates

The event selection of vector bosons is similar for all studies that are discussed in this article. Hence we introduce a general approach for the signal selection and background estimation for  $W$  and  $Z$  bosons. The discussion is mainly based on the published inclusive cross-section analyses based on the 2010 data sample [132], [133]. However, important differences in the signal selection for other analyses, such as the production of vector bosons in association with jets, are also highlighted. As the event selection is rather technical matter in nature, this section should be understood as an introduction to the basic concepts. Experienced readers might find the relevant information summarised in Tables 6, 7 and 8.

### 5.1 Signal selection and background estimations of $Z/\gamma^*$ events

The experimental signature of  $Z$  bosons in the leptonic decay channel are two oppositely charged, isolated and energetic leptons. These leptons stem from the same vertex and form an invariant mass close to the  $Z$  boson mass of  $m_Z = 91.2$  GeV. An event display of the typical  $Z \rightarrow \mu\mu$  event candidate, recorded by the ATLAS detector, is shown in Figure 16. It should be noted that the di-lepton final state contains contributions from both  $Z$  boson and virtual photons ( $\gamma^*$ ) exchange as well as interference. Therefore, the measured production cross-sections are usually given in terms of a combined  $Z/\gamma^*$  exchange.

In most ATLAS analyses, the generic  $Z/\gamma^* \rightarrow l^+l^-$  selection requires two oppositely charged leptons with an invariant mass between  $66 \text{ GeV} < m_{ll} < 116 \text{ GeV}$ . Muons are required to have a reconstructed track in both the tracking and muon detectors within  $|\eta| < 2.4$  and a minimal transverse momentum of  $p_T > 20 \text{ GeV}$ . In addition, the muons are required to pass a relative tracking-based isolation requirement based on a cone radius of  $\Delta R = 0.2$ . Electrons are required to fulfil  $|\eta| < 1.37$  or  $1.52 < |\eta| < 2.4$  with a minimum transverse energy of  $E_T > 20 \text{ GeV}$ . In addition, the medium identification criteria have to be satisfied. ATLAS also uses forward electrons for some analyses, i.e electrons within  $2.4 < |\eta| < 4.9$  which have no associated track in the tracking system. For those electrons tight identification criteria have to be fulfilled and at least one of the two signal electrons must be within  $|\eta| < 2.5$  and have a corresponding track in the tracking detector.

CMS selects  $Z \rightarrow \mu\mu$  events by requiring two reconstructed, oppositely charged muons within  $|\eta| < 2.1$  coming from the same vertex and a transverse momenta requirement of  $p_T > 20 \text{ GeV}$ . Both muons have to fulfil a relative tracking-based isolation requirement within a cone radius of  $\Delta R = 0.3$  and must match to the corresponding di-lepton

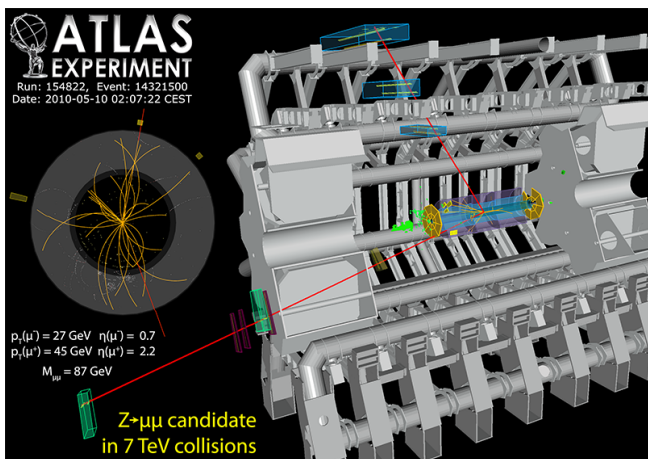


**Fig. 16** Event display of a typical  $Z \rightarrow \mu\mu$  event candidate, recorded by the ATLAS detector. The reconstructed muon tracks in the barrel and endcap region are indicated as red lines.

trigger objects. Later CMS analyses, extend the  $|\eta|$ -requirement to 2.4 and lower the cuts on the muon transverse momenta: the leading and subleading muon have to fulfil  $p_T > 14$  GeV and  $p_T > 9$  GeV, respectively. For the electron decay channel of  $Z \rightarrow ee$ , at least two reconstructed electrons within  $|\eta| < 1.44$  or  $1.57 < |\eta| < 2.5$  and  $E_T > 20$  GeV are required. In later CMS analyses, this was relaxed to require the leading electron to have  $p_T > 20$  GeV, while the subleading electron must fulfil  $p_T > 10$  GeV. While it is not required that both electrons have oppositely reconstructed charge, they must be matched to the corresponding trigger objects. The electrons must also satisfy a relative tracking-based isolation requirements within a cone radius of  $\Delta R < 0.3$ . The  $Z$  boson mass range for both channels is defined as  $60 \text{ GeV} < m_{ll} < 120 \text{ GeV}$ . The chosen mass range of the CMS experiment is larger compared to the ATLAS definition. This leads to an increase of the available phase space by a factor of 1.015 for CMS. The signal selection cuts are summarised in Table 6.

For measurements of  $Z/\gamma^*$  production in association with jets, the jets are required to have  $p_T > 30$  GeV. For ATLAS measurements, the jets at high rapidities are used,  $|y| < 4.4$ , whereas CMS uses jets within the acceptance of the tracker,  $|\eta| < 2.4$ . Since ATLAS and CMS use jet algorithms with different size parameters (see Section 3.5) the jet energies can not be directly compared. Jets within an  $\Delta R < 0.3$  or  $\Delta R < 0.5$  of an electron or muon are not counted for CMS and ATLAS analyses, respectively.

For  $Z/\gamma^* \rightarrow l^+l^-$  events, the main background contributions stem from  $Z \rightarrow \tau\tau$  events, di-boson events,  $t\bar{t}$  decays and QCD multi-jet events.  $Z \rightarrow \tau\tau$  events can pass the signal selection when the  $\tau$ -leptons decay into electrons or muons. Di-boson production such as  $WZ \rightarrow l^\pm \nu l^+l^-$  and top-quark pair production such as  $(t\bar{t} \rightarrow W^+bW^-\bar{b} \rightarrow l^+ \nu bl^-\nu)$  both have signatures with two energetic and isolated leptons. With

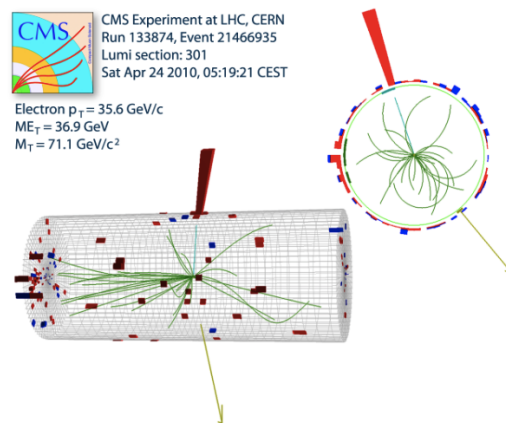


**Fig. 17** Event display of a typical  $W \rightarrow e\nu$  event candidate, recorded by the CMS detector. The reconstructed cluster in the electromagnetic calorimeter is shown in red, the missing transverse energy in yellow.

the exception of the  $WZ$  di-boson process, these processes though do not peak at  $m_Z$  and are largely removed by the mass cut. The QCD multi-jet events do not necessarily have a lepton in the final state and are discussed in more detail below.

To estimate the backgrounds, CMS often uses a data-driven approach, which exploits the fact that most of the mentioned background processes have an  $e\mu$  decay channel, while the signal has two same flavour leptons in the final state. By requiring opposite flavour leptons, the background can be directly estimated after correcting for differences in the lepton reconstruction. For most ATLAS analyses, simulations are used for these estimates, since these processes are theoretical well understood in both the absolute background contribution as well as the predictions of the kinematic distributions. In  $Z/\gamma^*$  production in association with jets, the background from  $t\bar{t}$  production becomes more significant for larger jet multiplicities. In this case, ATLAS analyses use a data-driven approach similar to the CMS method.

The QCD multi-jet background cannot be predicted precisely and must be estimated with data-driven methods. QCD multi-jet events pass the signal selection cuts in one of two ways: a jet is misreconstructed in the calorimeter and *fakes* an electron signature or the jet contains a heavy-flavour quark or kaon which decays into an electron or muon. In the first case, jets can fake an electron signal without a real electron in the jet itself whereas in the second case a real lepton is present. The main difference between the lepton signatures for QCD multi-jets versus those from  $Z/\gamma^*$  events is the isolation properties and - in the case of electrons - the calorimeter shower-shapes. While the leptons in signal events appear very isolated in the detector, jets contain a significant number of adjacent particles. Similarly  $W$  boson production in association with jets can also mimic this signature, where one lepton comes from the leptonic  $W$  boson decay, and the

**Table 6** Summary of the kinematic cuts used by the ATLAS [132] and CMS analysis [133] on leptons and their invariant quantities for the electron and muon decay channel of  $Z$  and  $W$  Bosons respectively.

	ATLAS		CMS	
	$Z \rightarrow l^+l^-$	$W^\pm \rightarrow l^\pm \nu$	$Z \rightarrow l^+l^-$	$W^\pm \rightarrow l^\pm \nu$
Electron-Channel	$E_T(e^+) > 20$ GeV $E_T(e^-) > 20$ GeV $ \eta_{e^\pm}  < 1.37$ or $1.47 <  \eta_{e^\pm}  < 2.47$ $66 \text{ GeV} < m_{ee} < 116 \text{ GeV}$	$p_T(e^\pm) > 20$ GeV $p_T(\nu) > 25$ GeV $ \eta_{e^\pm}  < 1.37$ or $1.47 <  \eta_{e^\pm}  < 2.47$ $m_T > 40$ GeV	$E_T(e^+) > 25$ GeV $E_T(e^-) > 25$ GeV $ \eta_{e^\pm}  < 1.44$ or $1.57 <  \eta_{e^\pm}  < 2.5$ $60 \text{ GeV} < m_{ee} < 120 \text{ GeV}$	one $e^\pm$ with $E_T > 25$ GeV $ \eta_{e^\pm}  < 1.44$ or $1.57 <  \eta_{e^\pm}  < 2.5$
Muon-Channel	$p_T(\mu^+) > 20$ GeV $p_T(\mu^-) > 20$ GeV $ \eta_{\mu^\pm}  < 2.4$ $66 \text{ GeV} < m_{\mu\mu} < 116 \text{ GeV}$	$p_T(\mu^\pm) > 20$ GeV $p_T(\nu) > 25$ GeV $ \eta_{\mu^\pm}  < 2.4$ $m_T > 40$ GeV	$p_T(\mu^+) > 25$ GeV $p_T(\mu^-) > 25$ GeV $ \eta_{\mu^\pm}  < 2.1$ $60 \text{ GeV} < m_{\mu\mu} < 120 \text{ GeV}$	one $e^\pm$ with $p_T > 25$ GeV $ \eta_{\mu^\pm}  < 2.1$

second lepton originates from or is faked by the accompanying jet.

To estimate these backgrounds, both experiments use similar data-driven approaches. A control region in data dominated by the QCD multi-jet events is used to define the kinematic distributions of the background. For the muon decay channel, this is achieved by inverting the isolation cut of one of the muons. The control region for the electron channel is obtained by requiring a non-isolated electron which only passes the loose electron identification cuts. The uncertainties of the predicted background distributions can be cross-checked by comparing the spectra to same-sign, isolated dilepton events, which is also expected to be dominated by QCD multi-jet background. The absolute normalisation of the QCD multi-jet background is then achieved by adjusting the sum of the expected signal and other background template to the data as a function of the invariant mass. For  $Z/\gamma^*$  production in association with jets, the normalisation of the QCD multi-jet background is determined for each jet multiplicity separately.

Some CMS analyses extract the signal yield together with the lepton trigger and reconstruction efficiencies by using a simultaneous fit to the measured invariant mass spectra in several di-lepton candidate categories, e.g. two combined muons or one combined muon and one inner detector track. The shapes of the signal and background distributions are taken from MC predictions or data-driven approaches as described above.

For measurements of a  $Z$  boson in association with  $b$ -jets, backgrounds from  $Z$  events in association with light ( $u$ ,  $d$ , and gluon) jets and  $c$ -quark jets dominate. To determine the number of  $Z+b$ -jet events, first di-boson, single-top,  $t\bar{t}$ , and  $W \rightarrow \tau\nu$  or  $Z \rightarrow \tau\nu$  backgrounds are removed. For CMS analyses, the dominant background of  $t\bar{t}$  is normalised to the data at large values of the  $Z$  boson mass peak, whereas for the ATLAS analysis, simulations are used to subtract the background. To extract the number of  $Z+b$ -jets events from the light- and  $c$ -jet events, both ATLAS and CMS use a similar approach; a maximum likelihood fit is performed using a

$b$ -tagging observable. For the CMS analysis, this observable used is the invariant mass of the secondary vertex, estimated from the  $b$ -tagging algorithm. For ATLAS measurements, the observable used is one of the outputs of the  $b$ -tagging algorithm's neural network. In both cases, these observables are chosen because they give good separation between light-,  $c$ - and  $b$ -jet events. The number of  $Z+b$ -jets is then determined from the fit.

The selected data for the inclusive  $Z$  boson production measurements based on the 2010 data sample for ATLAS and CMS together with their expected signal and background contributions, as well as the respective uncertainties, are summarised in Table 7. Similar background contaminations and associated uncertainties are seen in the analyses which are based on the 2011 data. The invariant mass distributions and the  $p_T$  spectra of the decay leptons for the selected data samples and the signal MC predictions are shown for ATLAS and CMS in Figure 18 and 19, respectively. All detector correction effects have been applied. The background contribution is a few percent, making the leptonic  $Z$  boson decay channel one of the cleanest signatures at the LHC. Hence it is an ideal channel for precision measurements of the Standard Model as well as for the detector calibration. Overall, excellent agreement between data and the predictions can be seen.

## 5.2 Signal selection and background estimations of $W$ boson events

The leptonic decay of the  $W$  bosons ( $W^\pm \rightarrow l^\pm \nu$ ) leads to an isolated and energetic lepton and missing transverse energy. An event display of the typical  $W \rightarrow e\nu$  event candidate, recorded by the CMS detector, is shown in Figure 17. Since no information on the  $z$ -component of the missing energy is available, the mass of the  $W$ -boson cannot be reconstructed. However, the invariant mass projection to the transverse plane, defined as

$$m_T = \sqrt{2 \cdot p_T^l \cdot p_T^\nu \cdot (1 - \cos(\phi^l - \phi^\nu))}, \quad (43)$$



**Table 7** Data sample and background estimations of the ATLAS and CMS inclusive analyses for the process  $Z \rightarrow l^+l^-$ , based on the 2010 data sample.

	ATLAS		CMS	
	$Z \rightarrow e^+e^-$	$Z \rightarrow \mu^+\mu^-$	$Z \rightarrow e^+e^-$	$Z \rightarrow \mu^+\mu^-$
Data (2010)	9725	11709	8452	13 728
Total Background	$206 \pm 64$	$86 \pm 32$	$35 \pm 11$	$60 \pm 21$
Percentage of each background compared to the total number of backgrounds				
$WW, WZ, ZZ$	10%	26%	37%	47%
$t\bar{t}, Z \rightarrow \tau\tau$	14%	22%	47%	50%
QCD multi-jets	76%	52%	16%	3%

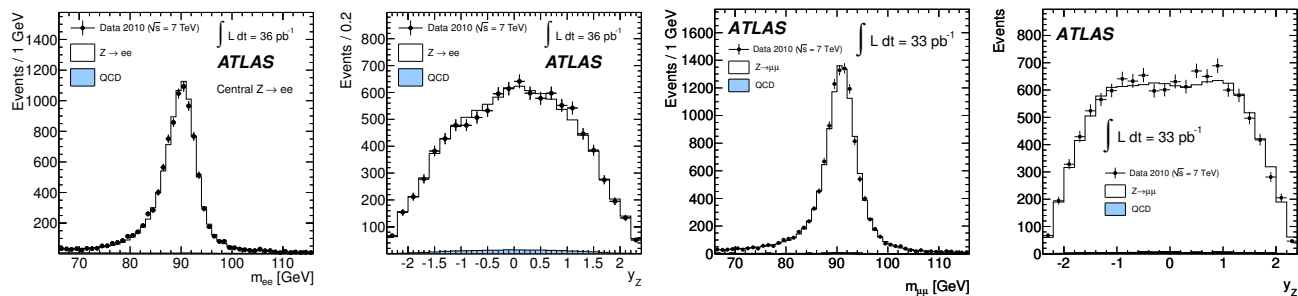


**Fig. 18** ATLAS [132]: Di-lepton invariant mass and rapidity  $y_Z$ -distribution for the central electrons and muons. The simulation is normalised to the data. The QCD multi-jet background shapes have been estimated by data-driven methods.

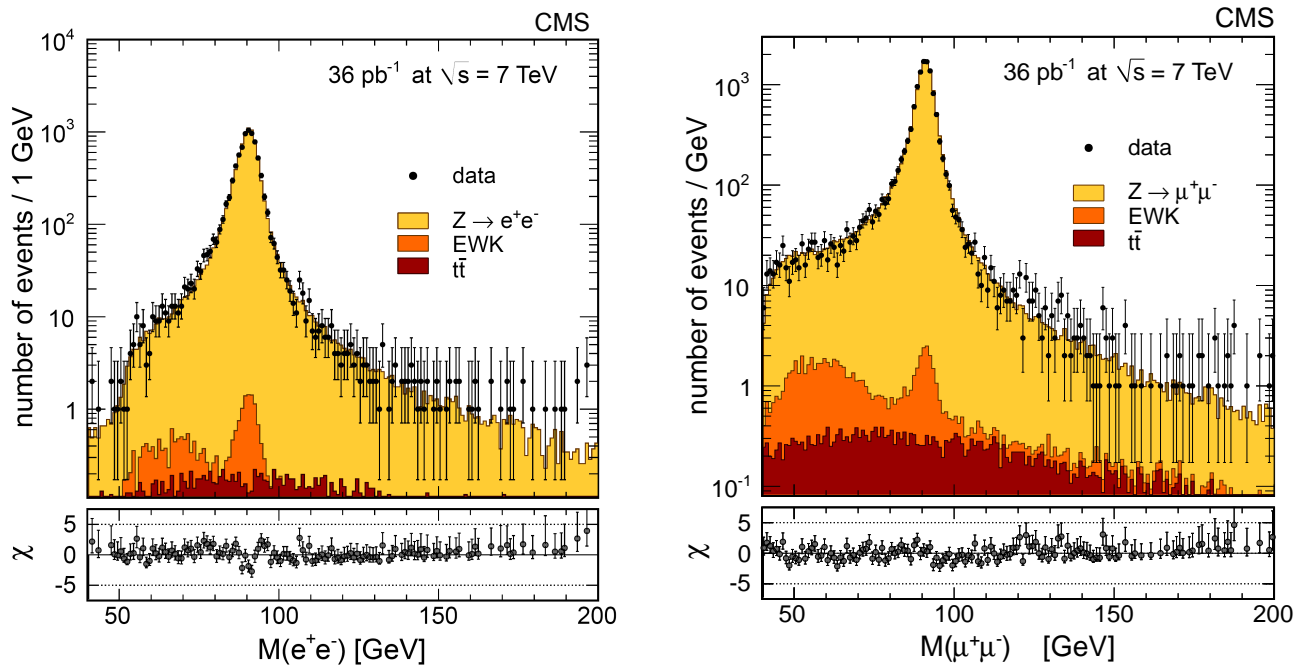


**Fig. 19** CMS [133]: Di-lepton invariant mass spectra of selected Z boson events, where all detector corrections have been applied. The points with the error bars represent the data. Superimposed are the expected distributions from simulations, normalised to an integrated luminosity of  $36 \text{ pb}^{-1}$ . The expected distributions are the Z signal (yellow, light histogram), other EWK processes (orange, medium histogram), and  $t\bar{t}$  background (red, dark histogram).

can be reconstructed, since the  $(x, y)$  components of the neutrino momentum are inferred from the  $E_T^{\text{miss}}$ . This observable is identical to the  $W$  boson mass when the decay happens purely in the  $x$ - $y$ -plane.

The ATLAS analyses select  $W$  boson events by requiring one reconstructed, isolated lepton, a minimal  $E_T^{\text{miss}}$  of 25 GeV and a minimal transverse mass of  $m_T > 40$  GeV. For the muon decay channel, one combined reconstructed muon with  $p_T > 20$  GeV within  $|\eta| < 2.4$  is required. In the electron decay channel, electrons are required to fulfil  $|\eta| < 1.37$  or  $1.52 < |\eta| < 2.4$  with a minimum transverse energy of  $E_T > 20$  GeV and medium identification criteria.

The signal selection in the corresponding CMS analysis is significantly different.  $W$  boson candidate events are selected by only requiring one reconstructed electron with  $E_T > 25$  GeV and  $|\eta| < 2.5$  or one reconstructed muon with  $p_T > 25$  GeV and  $|\eta| < 2.1$ . In later analyses, the  $\eta$  requirement has been relaxed to  $|\eta| < 2.4$  for muons but the threshold for electrons raised to  $E_T > 35$  GeV. Events with a second reconstructed lepton with  $p_T > 15$  GeV are vetoed. No additional cuts on  $E_T^{\text{miss}}$  and  $m_T$  are imposed. For the CMS measurement of  $W$  events in association with jets, the selection is slightly modified. The cut on the reconstructed lepton is  $p_T > 20$  GeV with no additional leptons above  $p_T > 10$  GeV. A cut of  $m_T > 20$  GeV is applied.

Both experiments use the signed curvature of the lepton tracks in the inner detector to determine its charge and hence also the charge of the  $W$  boson. While the charge misidentification is rare in muon events, a significant fraction of electron charges are mismeasured. Due to substantial material in the tracking detector, a large fraction of electrons radiate photons which in turn may convert to electron-positron pairs close to the original electrons, leading to charge misidentifications during the track reconstruction. In addition to the tracking information, CMS also uses the vertex and cluster position of the calorimeter for the charge identification.

For  $W$  production in association with jets, the jet selection is the same as described in Section 5.1.

For both experiments, the major sources of backgrounds for the signal selection are  $Z/\gamma^*$  production, the  $\tau$ -lepton decay channel of the  $W$ -boson, di-boson production, QCD multi-jet events and top-pair production.

The  $Z/\gamma^*$  process can pass the signal signature when one lepton is not reconstructed, e.g. by being outside of the detector acceptance, thereby creating significant amounts of  $E_T^{\text{miss}}$ . This background is theoretically understood to high precision and therefore the kinematic distributions can be predicted directly from simulations. The normalisation is either taken from a control sample (by requiring two reconstructed leptons), or also from simulations. Similarly the  $W \rightarrow \tau\nu$  background, where the  $\tau$  lepton decays further into electrons or muons and di-boson production, where one or both of the bosons decays to leptons, is also theoretically

well understood and modelled to a sufficient precision by simulations.

As discussed in Section 5.1, the QCD multi-jet background must be estimated using data-driven techniques. In ATLAS analyses, the QCD multi-jet control region in the muon channel is defined by reversing the isolation and removing the cut on  $E_T^{\text{miss}}$ . For the electron channel, the control sample is defined by inverting some electron identification criteria and not applying an  $E_T^{\text{miss}}$  requirement. The normalisation of the QCD multi-jet background is determined from data using a fit of the  $E_T^{\text{miss}}$  distribution, the results of which can be seen in Figures 20 and 21. For  $W$  production in association with jets, the normalisation is determined separately for each jet multiplicity.

For measurements of the inclusive  $W$  production, CMS extracts the number of  $W$  signal events with a binned, extended maximum likelihood fit to the  $E_T^{\text{miss}}$  distributions. The  $E_T^{\text{miss}}$  distributions for the signal and for the  $Z/\gamma^*$ ,  $t\bar{t}$  and  $W \rightarrow \tau\nu$  backgrounds are based on simulations. The shape of the QCD multi-jet background  $E_T^{\text{miss}}$  template is determined in a control region, defined by inverting a subset of the electron identification criteria or the muon isolation requirement for the  $W \rightarrow e\nu$  and  $W \rightarrow \mu\nu$ -channel, respectively. The fit is performed separately for  $W^+$  and  $W^-$  signal events.

Similar to  $Z/\gamma^*$  and di-boson production, top-pair production is also theoretically well understood but this background is large for  $W$  production in association with jets. For inclusive measurements of  $W$  production where the top-pair production is a small contribution, simulations are used for the background estimates. For  $W$  events with jets, CMS uses a data-driven approach to determine simultaneously the number of both the top-pair events as well as the QCD multi-jet events. This method exploits two features about  $t\bar{t}$  and QCD multi-jet events. First, since  $t\bar{t}$  events contain a semileptonic decay of the  $W$ , these events also peak in  $m_T$  at the  $W$  mass. In contrast, QCD multi-jet events do not peak and have a falling  $m_T$  spectra. Second,  $t\bar{t}$  events also contain jets from  $b$ -quarks which can be selected via  $b$ -tagging. To determine the normalisation for  $t\bar{t}$  and QCD multi-jet events, a 2-dimensional fit in  $m_T$  and the number of  $b$ -tagged jets is performed in each jet multiplicity bin. For the ATLAS measurements, the number of  $t\bar{t}$  events is determined using a 1-dimensional fit in the rapidity of the lepton as well as the mass of the  $W$ -jet system for each jet multiplicity. The fitted number of  $t\bar{t}$  events is consistent with those from the simulations but has a large statistical uncertainty. For this reason, the ATLAS measurements use  $t\bar{t}$  simulations for the background estimates.

For the measurement of  $W + b$ -jets from ATLAS where the  $t\bar{t}$  background is kinematically very similar to the signal events, control regions with four jets are used to constrain the normalisation for the  $t\bar{t}$  events. In addition the normalisa-

tion of single-top events is constrained by fitting the invariant mass of the  $W$  boson and  $b$ -jet system. The extraction of the  $b$ -quark events from the light- and  $c$ -jet background uses a similar approach as outline in Section 5.1.

Again, the 2010 analyses for ATLAS [132] and for CMS [133] are chosen as an example of the expected background contributions. The resulting number of selected events of ATLAS and CMS together with their expected signal and background contributions and their uncertainties are summarised in Table 8. The corresponding  $E_T^{\text{miss}}$  and  $m_T$  distributions of selected  $W$ -boson events is shown for the ATLAS and CMS experiments in Figure 20 and 21 respectively.

## 6 Inclusive and Differential Cross-Section Measurements

The Standard Model predictions of the Drell-Yan processes  $pp \rightarrow W^\pm + X$  and  $pp \rightarrow Z/\gamma^* + X$  can be tested in a completely new energy regime at the LHC: the study of the Drell-Yan processes provides a unique opportunity to test perturbative QCD predictions and improve the knowledge of the proton's PDFs (Section 6.1, 6.2). The measurement of the transverse momentum distribution of vector bosons can be used to test resummation techniques in addition to higher-order corrections in QCD calculation. The corresponding measurements are presented in Section 6.3. Moreover, the measurement of the forward-backward production asymmetry can constrain the vector and axial-vector couplings of the  $Z$  boson to the quarks, where the latest results are presented in Section 6.5 and the measurement of  $W$  boson polarisation can test the electroweak properties of the underlying production mechanism, discussed in Section 6.6. Finally, the precise understanding of the Drell-Yan processes is a key-element for the search of beyond the Standard Model signatures at the LHC. Very similar decay signatures of  $W$  and  $Z$  bosons are for example predicted by models of large extra dimensions [134], additional  $U(1)$  gauge groups [135] or quark-lepton compositeness models [136]. Hence, deviations from the predicted production properties could open the window to new physics.

### 6.1 Inclusive cross-section measurements

The inclusive production cross-sections for the Drell-Yan processes for the  $W$  boson and  $Z/\gamma^*$  exchange are known to NNLO precision in the strong coupling constant to a precision of  $\approx 2\%$  (Section 2.7.7). The dominating uncertainties are due to the limited knowledge of PDFs, while scale uncertainties play only a minor role.

At tree level,  $Z$  bosons are produced by the annihilation of quarks and antiquark pairs, i.e.  $u\bar{u}$ ,  $d\bar{d}$  and to some extent  $s\bar{s}$ . While the  $u$  and  $d$  quarks are mainly the valence quarks of

the proton, their respective antiquarks are always sea-quarks in proton-proton collisions. The situation is different for the production of  $W^\pm$  bosons, since their production mechanism depends on their charge. The dominant processes for  $W^+$  and  $W^-$  are  $u\bar{d} \rightarrow W^+$  and  $d\bar{u} \rightarrow W^-$ , respectively. Since two  $u$ -valence quarks are available in the proton, but only one  $d$ -valence quark, more  $W^+$  bosons are expected to be produced. The ratio of the  $W^+$  and  $W^-$  production therefore allows for a precise test of QCD predictions, as many theoretical and experimental uncertainties cancel in their ratio (Table 10).

As one of the first measurements performed at the LHC, the cross-sections times leptonic branching ratios  $\sigma_{W^\pm} \cdot BR(W \rightarrow l^\pm \nu)$  and  $\sigma_Z \cdot BR(Z \rightarrow l^+ l^-)$  of inclusive  $W$  and  $Z$  production for electron and muon final states were published by both experiments. These measurements, based on the 2010 data sample with  $\int \mathcal{L} dt = 35 \text{ pb}^{-1}$ , are not limited by their statistical precision [132], [133], but by the knowledge of the integrated luminosity. Hence, the inclusive results, which are discussed in the following, are based solely on the 2010 data sample.

The measurement strategy is based on Equation 39, which was discussed in detail in Section 4: The number of selected signal events is first corrected for the expected background contribution and then for detector effects via a factor  $C$  within a fiducial volume. The division by the integrated luminosity corresponding to the analysed data sample results in the fiducial cross-section. This can be extrapolated in a second step to the full inclusive cross-section via the acceptance factor  $A$ . The detector efficiency factors  $C$  and the acceptance factors  $A$  with their respective uncertainties are shown for both experiments and both decay channels in Table 9. The dominating experimental uncertainties are due to lepton scales and efficiencies.

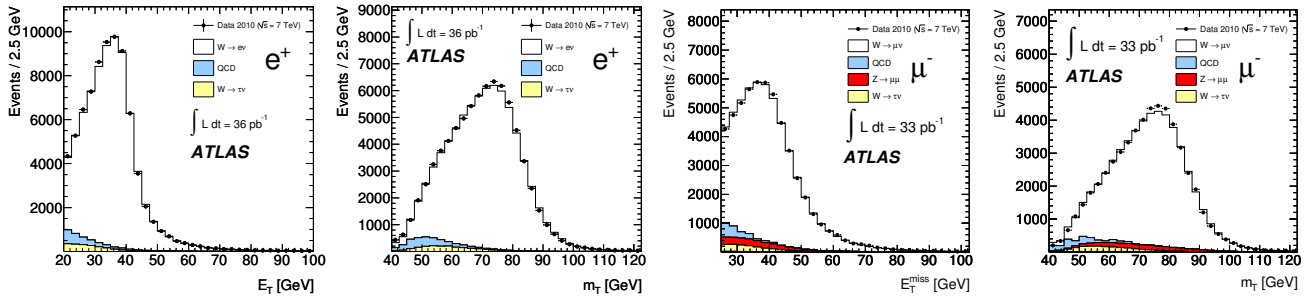
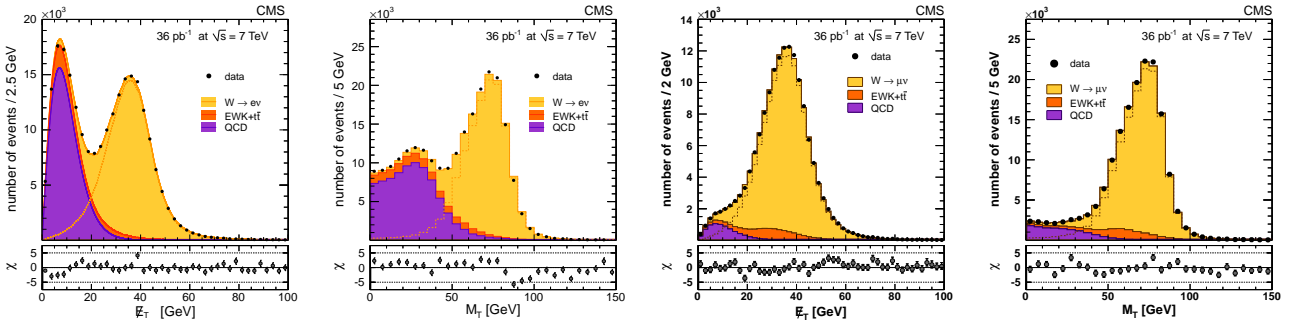
The combined results for the inclusive cross-sections for  $W^\pm$  and  $Z/\gamma^*$  for both experiments are also shown in Table 9. The dominating experimental uncertainties are due to the limited knowledge on the integrated luminosity. In fact, by using the theoretical predicted cross-section, the integrated luminosity of a data sample can be estimated.

The luminosity uncertainty on the cross-section measurement cancel in cross-section ratios, as well as some of the experimental and theoretical uncertainties. Hence, also cross-section ratios have been published for ATLAS and CMS. Special focus will be drawn to the  $\frac{\sigma(W^+) + \sigma(W^-)}{\sigma(Z)}$  ratio, shown in Table 10, where all correlated uncertainties have been taken into account. The NNLO prediction of the ratio is also given.

A simple leading-order calculation for the expected cross-section ratio for  $(W^+ + W^-)/Z$  highlights the dependence on the quark-distribution functions. Ignoring heavy quark and the  $\gamma^*$  contributions, as well as Cabibbo suppressed parts of the cross-section, leads to

**Table 8** Data sample and background estimations of the ATLAS and CMS inclusive analyses for the process  $W^\pm \rightarrow l^\pm \nu$ , based on the 2010 data sample.

	ATLAS		CMS	
	$W^\pm \rightarrow e^\pm \nu$	$W^\pm \rightarrow \mu^\pm \nu$	$W^\pm \rightarrow e^\pm \nu$	$W^\pm \rightarrow \mu^\pm \nu$
Data (2010)	130741	139748	235687	166457
Total Background	$9610 \pm 590$	$12300 \pm 1100$	$99684 \pm 388$	$25700 \pm 383$
Percentage of each background compared to the total number of backgrounds				
$W \rightarrow \tau \nu$	34%	34%	4%	16%
Top	5%	4%	1%	2%
$Z \rightarrow l^+ l^-$ , $WW$ , $WZ$ , $ZZ$	7%	23%	11%	26%
QCD multi-jet	54%	38%	85%	56%

**Fig. 20** ATLAS [132]: Distribution of the  $E_T^{\text{miss}}$  (left) and  $m_T$  (right) in the selected  $W^+ \rightarrow l^+ \nu$  candidate events after all cuts for electrons (left two plots) and muons (right two plots). The simulation is normalised to the data. The QCD multi-jet background is estimated via data-driven methods.**Fig. 21** CMS [133]: The  $E_T^{\text{miss}}$  and  $m_T$  distributions for the selected  $W^+ \rightarrow l^+ \nu$  candidate events. The points with the error bars represent the data. Superimposed are the contributions obtained with the fit for QCD multi-jet background (violet, dark histogram), all other backgrounds (orange, medium histogram), and signal plus background (yellow, light histogram). The orange dashed line is the signal contribution.**Table 10** Results of the production cross-section ratio  $\sigma(W^+)/\sigma(W^-)$  and  $\sigma(W^\pm)/\sigma(Z)$  from the ATLAS and CMS analyses, based on the 2010 data sample. The ATLAS measurement of  $\sigma(W^\pm)/\sigma(Z) = 10.89$  was extrapolated to the CMS mass-range definition of the Z-Boson. The expected theoretical value is also shown.

	ATLAS	CMS	Theory (NNLO)
$\sigma(W^+)/\sigma(W^-)$	1.454	1.421	1.43
Stat. Unc.	0.006	0.006	-
Sys. Unc.	0.012	0.014	-
Theo. Unc.	0.022	0.029	0.01
$\sigma(W^\pm)/\sigma(Z)$	10.73	10.54	10.74
Stat. Unc.	00.08	00.07	-
Sys. Unc.	00.11	00.08	-
Theo. Unc.	00.12	00.16	0.04

$$\begin{aligned} \sigma(W^+) + \sigma(W^-) &= u_v(x) + \bar{d}_s(x) + d_v(x) + \bar{u}_s(x) \\ \sigma(Z) &= (g_V(u)^2 + g_A(u)^2) \cdot u_q(x) \\ &\quad + (g_V(d)^2 + g_A(d)^2) \cdot \nu_q(x) \end{aligned} \quad (44)$$

with

$$u_q(x) = (u_v(x) + \bar{u}_s(x)), \quad \nu_q(x) = (d_v(x) + \bar{d}_s(x))$$

where  $u_v(x)$  and  $d_v(x)$  are the up- and down-valence quark distributions and  $u_s(x)$  and  $d_s(x)$  the respective sea-quark distributions. When assuming that the light sea and anti-quark distributions are the same for a given  $x$  and considering that  $(g_V(u)^2 + g_A(u)^2) \approx (g_V(d)^2 + g_A(d)^2)$ , this reduces to

**Table 9** Summary of the cross-section results of the inclusive  $W$  and  $Z$  analyses of ATLAS and CMS based on the 2010 data sample. The combined cross-sections are given with their respective statistical, systematic, acceptance and luminosity uncertainty, respectively.

ATLAS	$W^+ \rightarrow e^+ \nu$	$W^+ \rightarrow \mu^+ \nu$	$W^- \rightarrow e^- \nu$	$W^- \rightarrow \mu^- \nu$	$Z \rightarrow e^+ e^-$	$Z \rightarrow \mu^+ \mu^-$
Acceptance A	$0.479 \pm 0.008$	$0.4595 \pm 0.008$	$0.452 \pm 0.009$	$0.470 \pm 0.010$	$0.447 \pm 0.009$	$0.487 \pm 0.010$
Correction C	$0.693 \pm 0.012$	$0.796 \pm 0.016$	$0.706 \pm 0.014$	$0.779 \pm 0.015$	$0.618 \pm 0.016$	$0.782 \pm 0.007$
$\sigma_{incl.}$ [nb]	6.06	6.06	4.15	4.20	0.952	0.935
stat. unc. [nb]	0.02	0.02	0.02	0.02	0.010	0.009
sys. unc. [nb]	0.10	0.10	0.07	0.05	0.026	0.009
lumi. unc. [nb]	0.21	0.21	0.14	0.17	0.032	0.032
theo. unc. [nb]	0.10	0.10	0.09	0.07	0.019	0.019
$\sigma_{incl.}$ (comb.)	$6.05 \pm 0.02 \pm 0.07 \pm 0.10 \pm 0.21$		$4.16 \pm 0.01 \pm 0.06 \pm 0.08 \pm 0.14$		$0.937 \pm 0.006 \pm 0.009 \pm 0.016 \pm 0.032$	
CMS	$W^+ \rightarrow e^+ \nu$	$W^+ \rightarrow \mu^+ \nu$	$W^- \rightarrow e^- \nu$	$W^+ \rightarrow \mu^- \nu$	$Z \rightarrow e^+ e^-$	$Z \rightarrow \mu^+ \mu^-$
Acceptance A	0.5017	0.4594	0.4808	0.4471	0.3876	0.3978
Correction C	$0.737 \pm 0.01$	$0.854 \pm 0.008$	$0.732 \pm 0.01$	$0.841 \pm 0.008$	$0.609 \pm 0.011$	$0.871 \pm 0.011$
$\sigma_{incl.}$ [nb]	6.15	5.98	4.34	4.20	0.992	0.968
stat. unc. [nb]	0.02	0.02	0.02	0.02	0.011	0.008
sys. unc. [nb]	0.10	0.07	0.07	0.05	0.018	0.007
theo. unc. [nb]	0.07	0.08	0.06	0.07	0.016	0.018
lumi. unc. [nb]	0.25	0.25	0.17	0.17	0.040	0.049
$\sigma_{incl.}$ (comb.)	$6.04 \pm 0.02 \pm 0.06 \pm 0.08 \pm 0.24$		$4.26 \pm 0.01 \pm 0.04 \pm 0.07 \pm 0.17$		$0.974 \pm 0.007 \pm 0.007 \pm 0.018 \pm 0.039$	

$$\sigma(W^+) + \sigma(W^-) \sim \sigma(Z)$$

i.e. only a small dependence on PDFs is expected if the PDFs have been determined with the assumption of same light sea and antiquark distributions in the proton, i.e.  $\bar{q}(x) = q(x)$  for  $q = u, d, s$ . As this symmetry assumption is inherent for the main PDF fits,<sup>3</sup> no large difference in the theoretical predictions based on different PDF sets are observed. The good agreement between the measurements (Table 10) and the predictions are a remarkable confirmation of perturbative QCD calculations, but also support strongly the assumption of a flavour independent light quark sea at high scales, where  $x$  is small compared to 0.1, i.e.  $\bar{u} \approx \bar{d} \approx \bar{c} \approx \bar{s}$  at  $Q^2 \approx m_Z^2$ .

The above argument does not hold true for charge-dependent cross-section ratios, such as  $\sigma(W^+)/\sigma(Z)$ ,  $\sigma(W^-)/\sigma(Z)$  and  $\sigma(W^+)/\sigma(W^-)$ . They inhibit a significantly larger dependency on differences in the  $u$ - and  $d$ -quark distribution functions. However, the largest constraints on PDFs do not come from the inclusive cross-section measurements but from differential measurements, which are also discussed in the following section.

In summary, the inclusive cross-section measurements were one of the first published measurements at the LHC, that confirmed NNLO perturbative QCD predictions in a new energy regime. By now, also inclusive measurements of the  $W$  and  $Z$  cross-section at a center-of-mass energy of 8 TeV are available [137] which are also in very good agreement with the theoretical predictions.

<sup>3</sup>Small deviations are included to account for some light sea quark asymmetry near Bjorken  $x \approx 0.1$ .

## 6.2 Differential $W$ boson and $Z/\gamma^*$ measurements

In addition to the inclusive production cross-section, the large available statistics at the LHC also allows for measurements of differential production cross-sections with high precision. Of special importance here is the measurement of the rapidity distribution  $y_V$ <sup>4</sup> of the vector boson, as it allows for a direct determination of the momentum fractions  $x_{1/2}$  of the interaction partons, via

$$x_{1/2} = \frac{m_V}{\sqrt{s}} e^{\pm y_V},$$

where  $m_V$  is the mass of the vector boson. A center-of-mass energy of  $\sqrt{s} = 7$  TeV allows therefore to reach  $x$ -range from  $\approx 0.001$  to  $\approx 0.1$  for the study of  $W$  and  $Z$  bosons. The boson rapidity distributions are calculated up to NNLO in QCD theory [100] and are dominated by PDF uncertainties. Hence the measurement of the differential production cross-section of gauge bosons versus their rapidity distribution will provide additional constraints on the proton's PDFs. The results of deep inelastic scattering experiments provide constraints on the sea quark and gluon distributions at small and medium  $x$  values, while the studies of  $W$  and  $Z$  production at the Tevatron provided important information on the valence quark distributions. The additional information by measurements at the LHC on the valence quark distribution is therefore expected to be marginal. However, the LHC measurements have a significant impact on the strange-quark PDFs, as well as on the ratio of  $u/d$ -quark distributions as discussed below.

<sup>4</sup>The rapidity of a particle is defined as  $y = \frac{1}{2} \ln \frac{E+p_z}{E-p_z}$ , where  $E$  is the particle's energy and  $p_z$  is the longitudinal momentum w.r.t to proton direction.

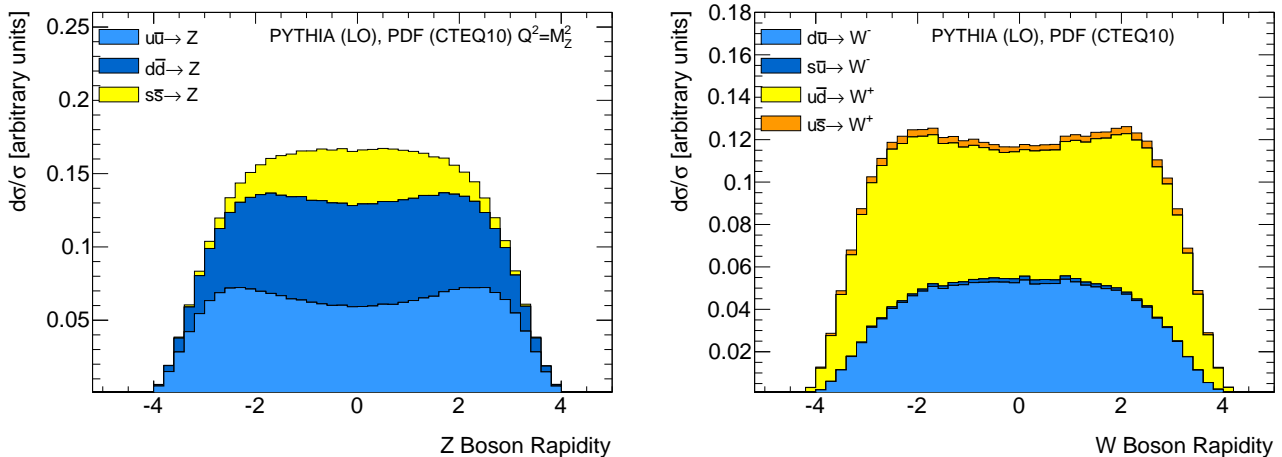


**Fig. 22** Rapidity Distribution for the leading-order production of Z (left) and W bosons (right) in 7 TeV pp collisions. The relative contribution of the different production channels is also shown.

The rapidity distribution of the  $Z/\gamma^* \rightarrow l^+l^-$  process can be directly inferred from data, since both four-momenta of its decay-leptons can be precisely measurement. Hence it will give new information on the  $u\bar{u}$ ,  $d\bar{d}$  and  $s\bar{s}$  PDFs. While the information on  $u$  and  $d$  quark distribution is already largely determined by previous experiments, in particular the uncertainty on the strange quark content can be improved. Figure 22 shows the contribution of the different quark/antiquark annihilation processes for different  $y_Z$  values. While the  $u\bar{u}$  annihilation is dominating in the central region, the  $d\bar{d}$  annihilation process is expected to have a larger influence for larger rapidity values. A precise measurement in the central rapidity region can also give additional constraints on the  $s\bar{s}$  PDFs. In addition, the study of  $y_Z/\gamma^*$  for different mass intervals can probe different  $x$ -regimes, e.g. low-mass Drell-Yan events will probe in general small values of  $x$  than high-mass Drell-Yan events. Such studies can be used to improve the knowledge on the ratio of  $u$ - and  $d$ -quark distributions.

ATLAS published a combined differential  $d\sigma/d|y_Z|$  cross-section in the fiducial region<sup>5</sup> for the electron and muon decay channel of  $Z/\gamma^* \rightarrow l^+l^-$  based on  $\int \mathcal{L} dt \approx 35 \text{ pb}^{-1}$  [132]. Figure 23 shows the results including NNLO theory predictions with various PDF sets. The largest rapidity reached is  $y_Z = 3.5$  which is due to the inclusion of forward electrons in this study. In addition, ATLAS published a differential cross-section of the Drell-Yan process in the electron decay channel versus the invariant mass of the di-electron pairs, based on the full 2011 data sample [138]. The comparison of data and NNLO predictions with various PDF sets is shown in Figure 24.

<sup>5</sup>defined by a cut on the invariant mass of the di-lepton system of  $66 \text{ GeV} < m_{ll} < 116 \text{ GeV}$  and a minimal requirement of  $p_T > 20 \text{ GeV}$  and  $\eta < 2.4$  for both decay leptons.

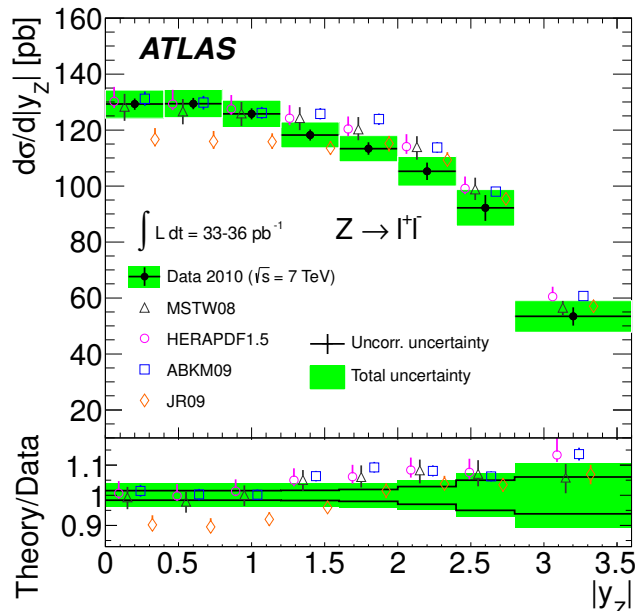


**Fig. 23** ATLAS [132]: The combined  $d\sigma/d|y_Z|$  cross-section measurement for  $Z/\gamma^* \rightarrow l^+l^-$  compared to NNLO theory predictions using various PDF sets. The kinematic requirements are  $66 \text{ GeV} < m_{ll} < 116 \text{ GeV}$  and  $p_T^l > 20 \text{ GeV}$ . The ratio of theoretical predictions to data is also shown. Theoretical points are displaced for clarity within each bin.

The latest CMS publication on  $Z \rightarrow l^+l^-$  [139] is also based on an integrated luminosity of  $\int \mathcal{L} dt \approx 4.5 \text{ fb}^{-1}$  and  $\int \mathcal{L} dt \approx 4.8 \text{ fb}^{-1}$  for the muon and electron channels, respectively. The measurement is performed in a double differential way over the mass range of  $20 \text{ GeV}$  to  $1500 \text{ GeV}$  and an absolute di-muon rapidity from  $0 < |\eta| < 2.4$ . The resulting rapidity distributions for three different mass regions are shown in Figure 25, together with the NNLO prediction for various PDF sets. The differential cross-sections have

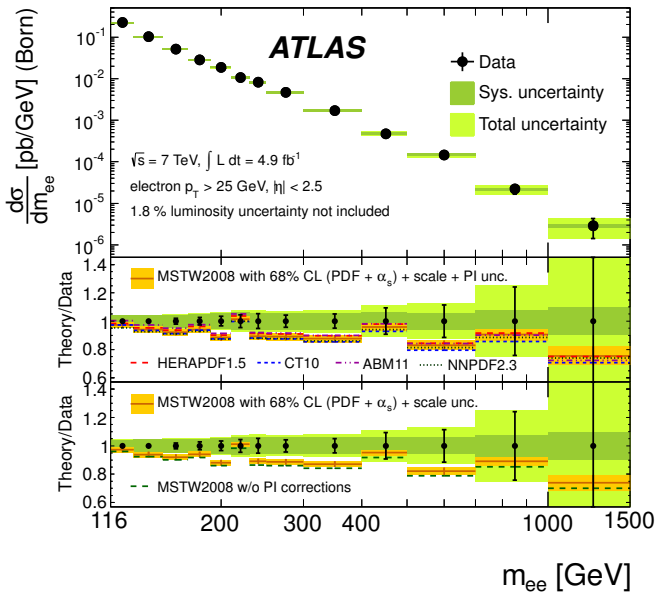


**Fig. 24** ATLAS [138]: Measured differential cross-section at the Born level within the fiducial region (electron  $p_T > 25$  GeV and  $|\eta| < 2.5$ ) with statistical, systematic, and combined statistical and systematic (total) uncertainties, excluding the 1.8% uncertainty on the luminosity. The measurement is compared to FEWZ 3.1 calculations at NNLO QCD with NLO electroweak corrections using the  $G_{mu}$  electroweak parameter scheme.

been extrapolated to the full phase space and normalised to the  $Z$  peak cross-section, which is defined in a mass region of 60 – 120 GeV. Hence many systematic uncertainties cancel in the ratio. The dominating remaining uncertainties are due to the efficiency corrections in the muon channel and energy scale uncertainties in the electron channel.

Especially in the low-mass region, sizeable differences between the different PDF sets can be seen. The uncertainties of the available data are small enough to provide sufficient sensitivity to allow for an improvement over the existing PDF sets. The uncertainty on the  $u/d$  ratio can be improved by more than 20%.

The  $W^\pm$  boson rapidity distribution is sensitive to the  $u\bar{d}$ - and  $d\bar{u}$ -quark distribution. Their respective contribution is shown in Figure 22. However, its rapidity distribution in the leptonic decay channel is not directly accessible as the longitudinal momentum of the neutrino not measured. Therefore only an indirect measurement is possible, which is achieved by the measurement of the pseudorapidity of the charged decay leptons  $\eta_l$  which are correlated to  $y_W$ . The production and decay of  $W$  boson is described by the V-A nature of the weak interaction. It is therefore expected that the spin of the  $W$  boson is aligned with the direction of the antiquark and the charged decay lepton is preferentially emitted opposite

to the boost of the decaying boson. The corresponding experimental quantity is the lepton charge asymmetry

$$A(\eta) = \frac{d\sigma(W^+ \rightarrow l^+ \nu)/d\eta - d\sigma(W^- \rightarrow l^- \nu)/d\eta}{d\sigma(W^+ \rightarrow l^+ \nu)/d\eta + d\sigma(W^- \rightarrow l^- \nu)/d\eta}, \quad (45)$$

where  $l$  denotes the lepton and  $d\sigma/d\eta$  the differential cross-section for charged leptons from the  $W$  events. The definition of  $A(\eta)$  has the advantage that several systematic uncertainties cancel in its ratio and can constrain the  $u/d$ -quark ratio and the corresponding sea-quark densities. Clearly, also the measurement of separate differential cross-sections  $d\sigma(W^\pm \rightarrow l^\pm \nu)/d\eta$  provides the same information when the correlation between the systematic uncertainties is known.

CMS published results on the lepton charge asymmetry in the electron and muon decay channels within a fiducial phase space defined by a  $p_T > 35$  GeV requirement for the charged decay leptons. Since the study of  $W \rightarrow e\nu$  [140] is based on only  $\int \mathcal{L} dt = 0.84 \text{ fb}^{-1}$  and the  $W \rightarrow \mu\nu$  analyses [141] uses the full available data sample at  $\sqrt{s} = 7$  TeV, we discuss here only the latter. The  $A(\eta)$  measurement after all corrections is shown in Figure 26 for a minimal muon requirement of  $p_T > 35$  GeV. The dominating systematic uncertainties are due to efficiencies and scale uncertainties, as well as uncertainties on the QCD multi-jet background. Statistical uncertainties are small compared to the systematic uncertainties, which range from 0.2% in the central region to 0.4% in the forward region. The correlations between different  $\eta$ -bins are small. The results are compared to NLO predictions for several PDF sets.

ATLAS has published similar results for the full 2010 data sample in both leptonic decay channels within a fiducial phase space, defined by  $p_T^{lep} > 20$  GeV,  $p_T^e > 25$  GeV and  $m_T > 40$  GeV. In addition to the lepton-charge asymmetry, which is shown in Figure 27, also the individual lepton charge distributions for  $W^+$  and  $W^-$  have been derived. Similar to the CMS results, statistical uncertainties are negligible compared to the systematic uncertainties.

While most PDF sets show good agreement with data, the MSTW2008 PDF parametrisation has a poor agreement especially in the region of small rapidities. This is due to a problem in  $d$ -valence distribution which was fixed in the MSTW2008CPdeutnlo set, which is also shown. Since the uncertainties of the measured  $A(\eta)$  values are smaller by a factor of 2-3 compared to the predicted uncertainties of the studied PDF sets, an improvement of future PDF sets is expected. Some preliminary results which make use if the currently published LHC data, can be found for example in [142].

Figure 28 and 29 show a comparison of the ATLAS and CMS results for the  $Z/\gamma^*$  and  $A_W(\eta)$  distributions, respectively. We extrapolate the results to a common fiducial volume, defined by  $60 \text{ GeV} < m_{ll} < 120 \text{ GeV}$  for the  $Z/\gamma^*$  pro-

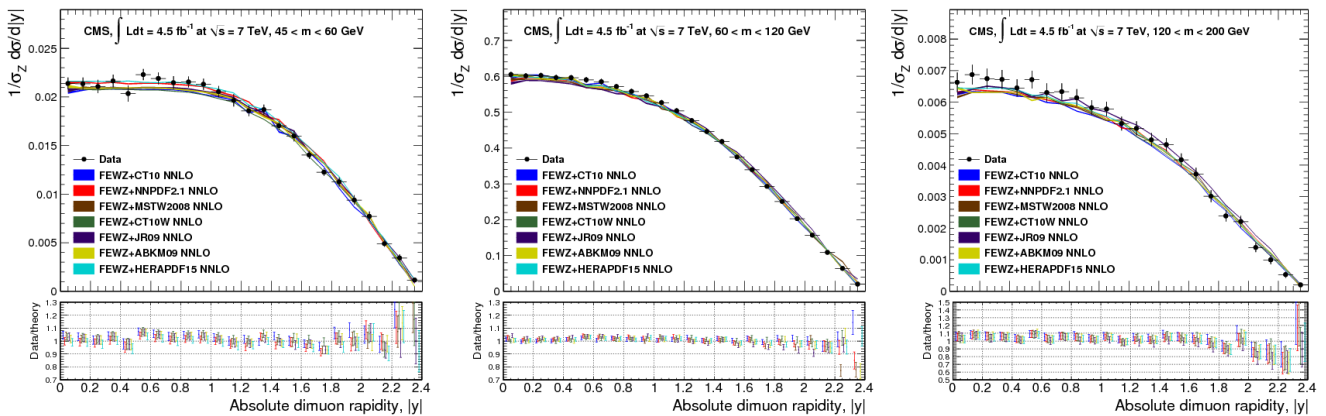


**Fig. 25** CMS [139]: Comparison with theory expectations with various NNLO PDF sets: CT10, HERA, NNPDF2.1, MSTW08, CT10W, JR09, ABKM. The error bands in the theory predictions indicates the statistical calculation error only. The bottom plots show the ratio of data to theory expectation. The error bar is the quadrature sum of experimental uncertainty on the data and statistical calculation error on theory expectation.

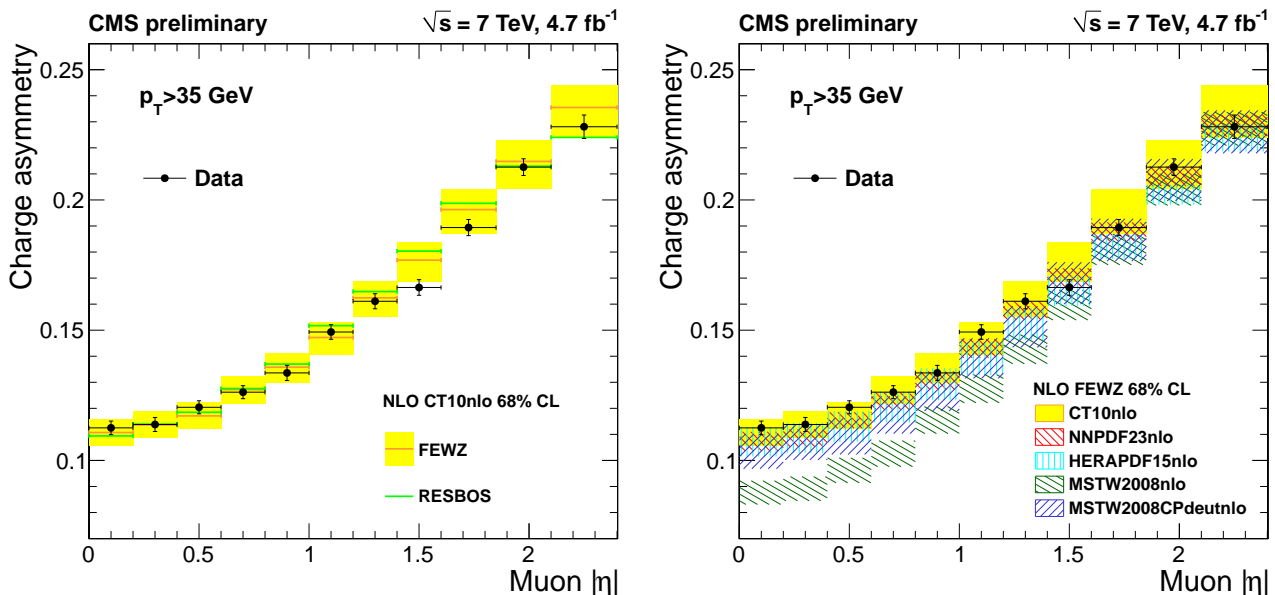


**Fig. 26** CMS [141]: Comparison of the measured muon charge asymmetry to theoretical predictions based on FEWZ 3.0 and RESBOS calculations, for muons with  $p_T > 35$  GeV (left). The CT10 NLO PDF is used in both predictions. A comparison of the measured muon charge asymmetries to predictions with CT10, NNPDF2.3, HERAPDF1.5, MSTW2008, and MSTW2008CPdeut NLO PDF models, for muons with  $p_T > 35$  GeV, is shown on the right.

cess and by  $p_T > 35$  GeV for the  $W^\pm$  boson. The extrapolation was performed with the POWHEGBOX generator and no additional systematic uncertainties have been added to the shown values. Both experiments show consistent results.

ATLAS has studied the impact of their data on the proton PDFs using the HERAFitter framework [143]. Here, especially the  $y_Z$  measurement has a large impact on the constraints of the strange-quark PDFs. Even with the limited data sample of 2010, the hypothesis of a symmetric composition of the light sea-quarks at low  $x$  [132] is supported. Specifically, the ratio of the strange sea-quark content to the down sea-quark content at  $x = 0.023$  was found to be  $1^{+0.25}_{-0.28}$  at  $Q^2 = 1.9$  GeV<sup>2</sup>. This is a remarkable results and

was confirmed in an improved analyses of the 2011 data sample [144]. So far it has been assumed in most PDF fitting approaches that  $s = \bar{s} = \frac{\bar{u}}{2} = \frac{\bar{d}}{2}$  due to the mass difference of the quarks at the starting scale, i.e. before the QCD evolution starts. At higher values of  $Q^2$ , the gluon splitting processes become dominant and lead to a symmetric distribution of sea-quarks. This new results suggests even an equal  $\bar{u}$ -,  $\bar{d}$ - and  $s$ -quark content at low  $Q^2$  values [132]. A visualisation of the impacts on the strange quark distributions is shown in Figure 30. The inclusion of electrons in the forward-region of the ATLAS detector extends the available  $y_Z$  regime and should therefore improve the information on



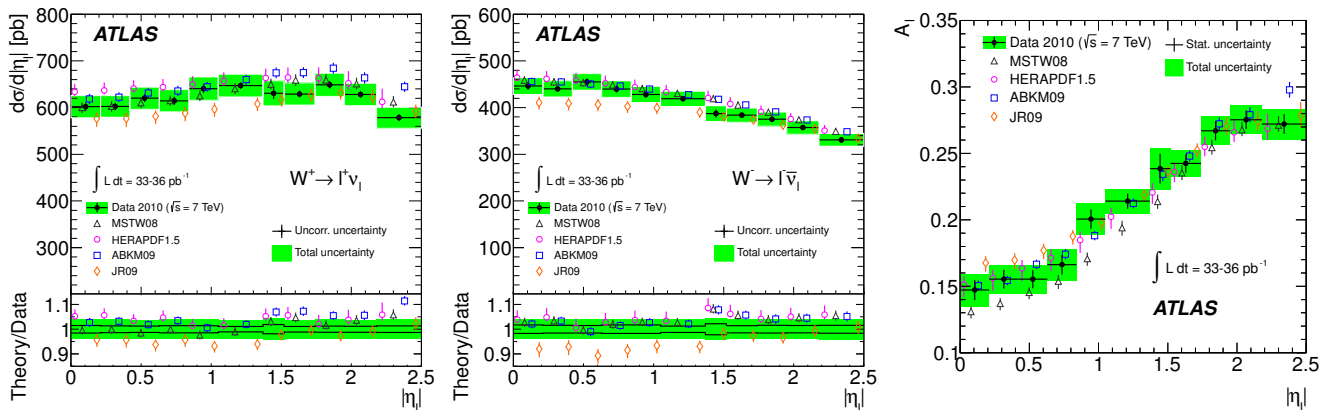


**Fig. 27** ATLAS [132]: Differential  $d\sigma/d|\eta|^{+}$  (left) and  $d\sigma/d|\eta|^{-}$  (middle) cross-section measurements within the fiducial volume for  $W \rightarrow l\nu$ . Measured  $W$  charge asymmetry as a function of lepton pseudorapidity  $|\eta|$  is shown on the right. All results are compared to the NNLO theory predictions using various PDF sets.

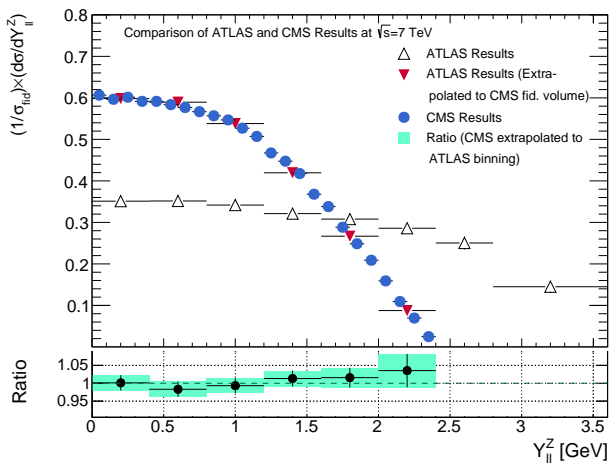


**Fig. 28** Comparison of the ATLAS and CMS: Measurements of the normalised differential cross-section of the Drell-Yan process as a function of the rapidity of the di-lepton system. The ATLAS results have been extrapolated to the CMS fiducial volume, as it is significantly reduced in  $Y_{ll}$ . For completeness, also the full normalised differential cross-section of the ATLAS experiment is shown.

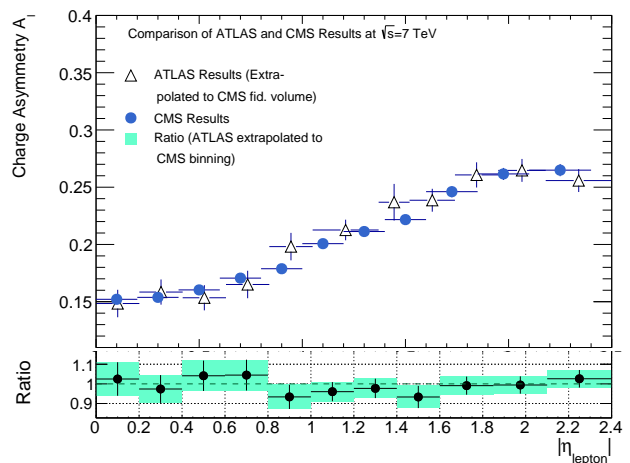


**Fig. 29** Comparison of the ATLAS and CMS: Measurements of the  $W$  charge asymmetry, where the ATLAS results have been extrapolated to the CMS fiducial volume.

the valence quark distributions. However, the current experimental uncertainties are too large for a significant effect.

The published results on the lepton charge asymmetry for the  $W$  boson production impacts moderately the valence quark distribution functions compared to the existing data that include Tevatron results. However, when only using measurements from HERA and LHC, an improvement on the valence quark distributions of more than 30% for the full  $x$ -range can be observed, compared to HERA measurements alone.

Also the LHCb experiment published a differential cross-section of the  $W^{\pm}$  and  $Z$  boson production in the forward rapidity region ( $2.0 < \eta < 4.0$ ), based on  $\int \mathcal{L} dt \approx 37 \text{ pb}^{-1}$ , which is consistent with the measurements of ATLAS and CMS. A detailed discussion can be found in [145].

In summary, the double-differential cross-section measurements of the  $W$  and  $Z$  bosons lead to important constraints to the PDFs of the proton. Figure 31 shows the improvement of the  $\bar{u}$  and  $\bar{s}$  parton density functions with and without including the current available LHC data based on the NNPDF group [146]. In particular the ATLAS analysis [132] suggests that the strange quark content is comparable to the  $\bar{u}$  and  $\bar{d}$  content even at low scales. With measurements using the full 2011 data set, the statistical and systematic uncertainties are expected to be decreased significantly and a further improvement  $> 20\%$  of the strange-quark PDFs and the  $u/d$ -quark ratio is anticipated. It is not clear how much improvement of a similar study of the full 2012 data set at a center-of-mass energy of  $\sqrt{s} = 8$  TeV can be expected. Even though the data set is larger by a factor of five, the 2011 re-

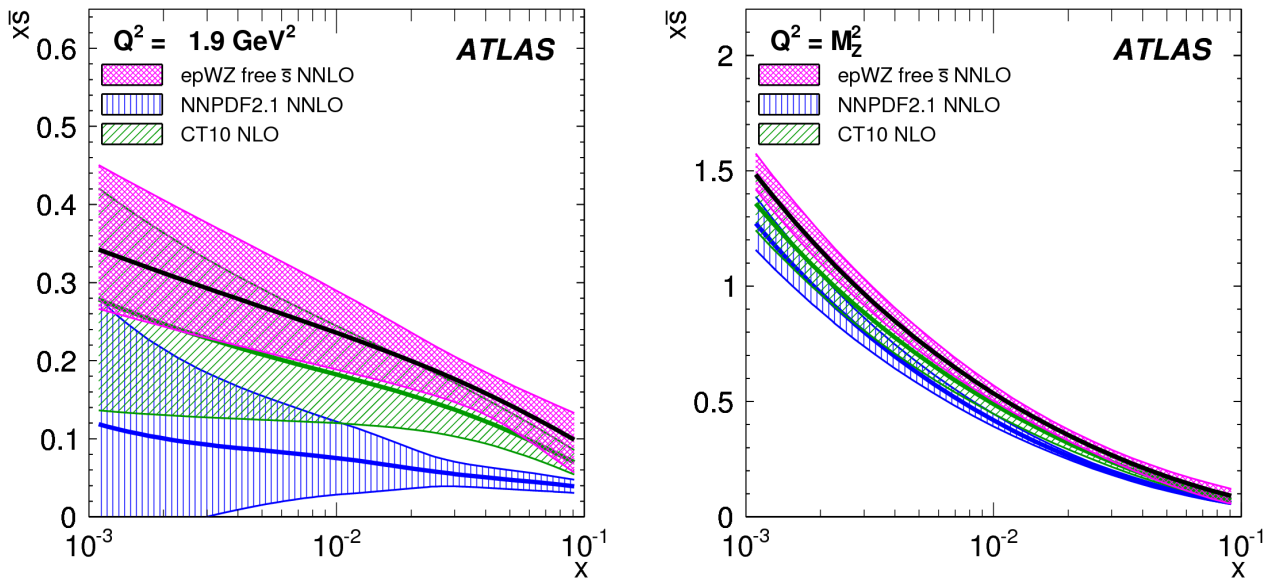


**Fig. 30** ATLAS [132]: The strange antiquark density vs  $x$  for the ATLAS (denoted as epWZ) free  $\bar{s}$  NNLO fit (magenta band) compared to predictions from NNPDF2.1 (blue hatched) and CT10 (green hatched) at  $Q^2 = 1.9 \text{ GeV}^2$  (left) and  $Q^2 = 91 \text{ GeV}^2$  (right).

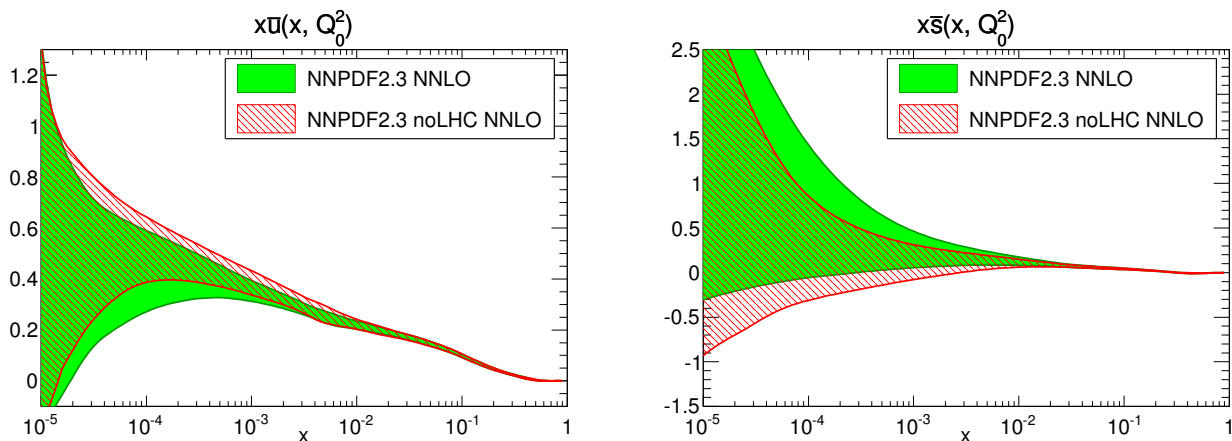


**Fig. 31** Comparison of  $\bar{u}$ -quark (left) and  $\bar{s}$ -quark (right) PDFs from the NNPDF2.3 NNLO sets with no LHC data and with LHC data used in the fit. Further comparison plots can be found in [146] and [142].

sults are not statistics limited and the increase of center-of-mass energy is only 10%.

### 6.3 Transverse momentum measurements of vector bosons

As discussed in Section 2.7.6, the transverse momentum distributions of vector bosons provides an important test of QCD corrections in the initial state of the production process due to the absence of colour flow between the initial and final state. In particular, predictions based on resummation techniques can be tested, which play an important role for the expected  $p_T$  spectra between 0 and  $\approx M_V/2 \text{ GeV}$ . Only a mild dependence on the proton PDFs is expected. Besides the test of QCD calculations, the accurate understanding of

the vector boson's  $p_T$  spectra is essential for the measurement of the  $W$  boson mass at the LHC, especially when the  $p_T$  spectrum of the decay leptons of  $W^\pm \rightarrow l^\pm \nu$  is used as a sensitive variable for  $m_W$ .

The transverse momentum distributions of electron and muon pairs from  $Z/\gamma^*$  events can be measured directly with the reconstructed four-momentum information of the decay leptons. The  $p_T(Z)$  momentum resolution for  $p_T(Z) < 40 \text{ GeV}$  is typically  $\approx 3 \text{ GeV}$  for ATLAS and CMS. A finite binning with a similar size leads therefore to resolution effects, i.e. bin migration, which make a dedicated unfolding procedure necessary (see Section 4).

CMS has published normalised transverse momentum distributions of the  $Z/\gamma^*$  process based on the 2010 data

sample [147]. The differential cross-section has been normalised to the cross-section integrated over the acceptance region, defined by  $p_T^\ell > 20$  GeV,  $|\eta| < 2.1$  and  $60$  GeV  $< m_{ll} < 120$  GeV. Both decay channels have been unfolded using an inverted response matrix and show consistent results, as seen in Figure 32.

ATLAS also published an analysis using the full 2010 data sample [148], also using both leptonic decay channels. The differential cross-sections have been normalised to the fiducial cross-section with  $66$  GeV  $< m_{ll} < 116$  GeV,  $p_T^\ell > 20$  GeV and  $|\eta| < 2.4$ . A Bayesian method has been used for the unfolding of the data, where the resulting distribution is shown in Figure 33 in comparison with different MC generator predictions<sup>6</sup>. The dominating systematic uncertainties are due to uncertainties of the momentum scale and resolution uncertainties as well as from the unfolding procedure.

The low  $p_T(Z)$  domain of the  $Z/\gamma^*$  production can be alternatively probed with the  $\Phi^*$  observable, defined as

$$\Phi^* = \tan\left(\frac{\pi - \Delta\Phi}{2}\right) \cdot \sin(\theta^*),$$

where  $\Delta\Phi$  is the azimuthal opening angle between the two decay leptons and

$$\cos(\theta^*) = \tanh\left(\frac{\eta^- - \eta^+}{2}\right)$$

as the measure of the scattering angle of the positive and negative leptons with respect to the beam [149]. The  $\Phi^*$  observable is highly correlated to  $p_T(Z)/m_{ll}$ ; a small  $p_T(Z)$  leads to a large opening angle and hence a small value of  $\Phi^*$ , while a large transverse momenta lead to small opening angles and therefore larger values of  $\Phi^*$ . A typical value of  $p_T(Z) \approx 100$  GeV leads to  $\Phi^* \approx 1$ . This variable has the advantage that it is solely constructed using track-based directions which are known to much higher precision than their transverse momenta. ATLAS has published unfolded normalised<sup>7</sup>  $\Phi^*$  distributions for three different regions  $Z$  boson rapidity regions ( $|y_Z| < 0.8$ ,  $0.8 < |y_Z| < 1.6$  and  $|y_Z| > 1.6$ ) [150]. The resulting distribution is shown in Figure 34 for both decay channels, together with the theoretical prediction based on the RESBOS generator. Both decay channels lead to consistent results and a clear deviation from the theoretical prediction can be observed; these are consistent with the published results on  $p_T(Z)$ . The systematic uncertainties are smaller than the associated statistical uncertainties for all bins. The statistical precision varies 0.3% for  $\Phi^* \approx 0$  to 1.6% for  $\Phi^* \approx 2.5$ .

<sup>6</sup>It should be noted that the differences in predictions of different generators could be due to different scale-parameter settings used.

<sup>7</sup>The results have been normalised to the same fiducial regime as the corresponding  $p_T(Z)$  analysis.

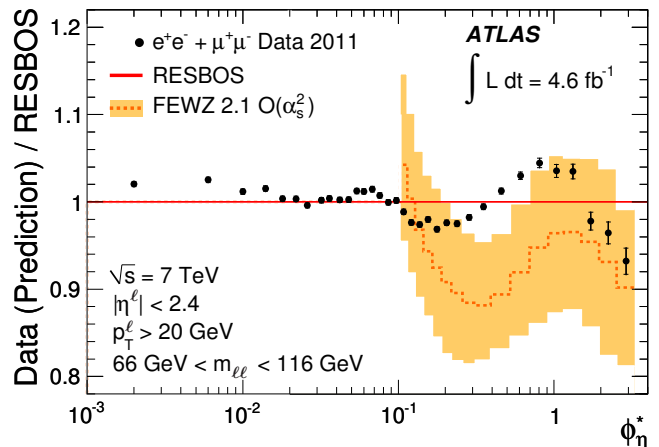


**Fig. 34** ATLAS: [150] The ratio of the combined normalised differential cross-section to RESBOS predictions as a function of  $\Phi^*$ . The inner and outer error bars on the data points represent the statistical and total uncertainties, respectively. The uncertainty due to QED FSR is included in the total uncertainties. The measurements are also compared to predictions, which are represented by a dashed line, from FEWZ 2.1. Uncertainties associated to this calculation are represented by a shaded band. The prediction from FEWZ 2.1 is only presented for  $\Phi^* > 0.1$ .

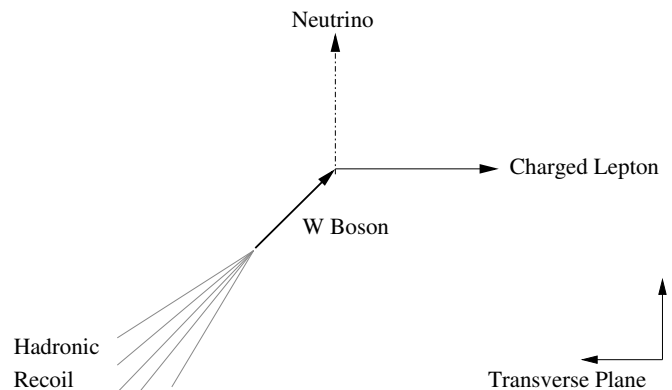


**Fig. 35** Illustration of the hadronic recoil in  $W^\pm \rightarrow l^\pm \nu$  events. While the transverse momenta of the  $Z$  boson can be directly interfered by its both decay leptons, the hadronic recoil has to be used in the leptonic decay modes of the  $W$  boson.

The measurements of the  $p_T(Z)$  distribution provides important information for the tuning of MC generators, which can then be indirectly transferred to the prediction of transverse momentum distribution of the  $W$  boson,  $\mathbf{p}_T(W)$ . However, an explicit measurement of  $\mathbf{p}_T(W)$  would allow to directly constrain the  $p_T$  spectrum of the  $W$  boson's decay leptons and therefore estimate uncertainties on an associated  $m_W$  measurement.

ATLAS also published a measurement of the transverse momentum distribution of the  $W$  boson  $\mathbf{p}_T(W)$  based on the 2010 data sample [151]. The  $\mathbf{p}_T(W)$  cannot be directly measured from its decay leptons due to the neutrino. However, the  $\mathbf{p}_T(W)$  must be balanced by the hadronic activity induced by QCD corrections in the initial and final state, i.e.

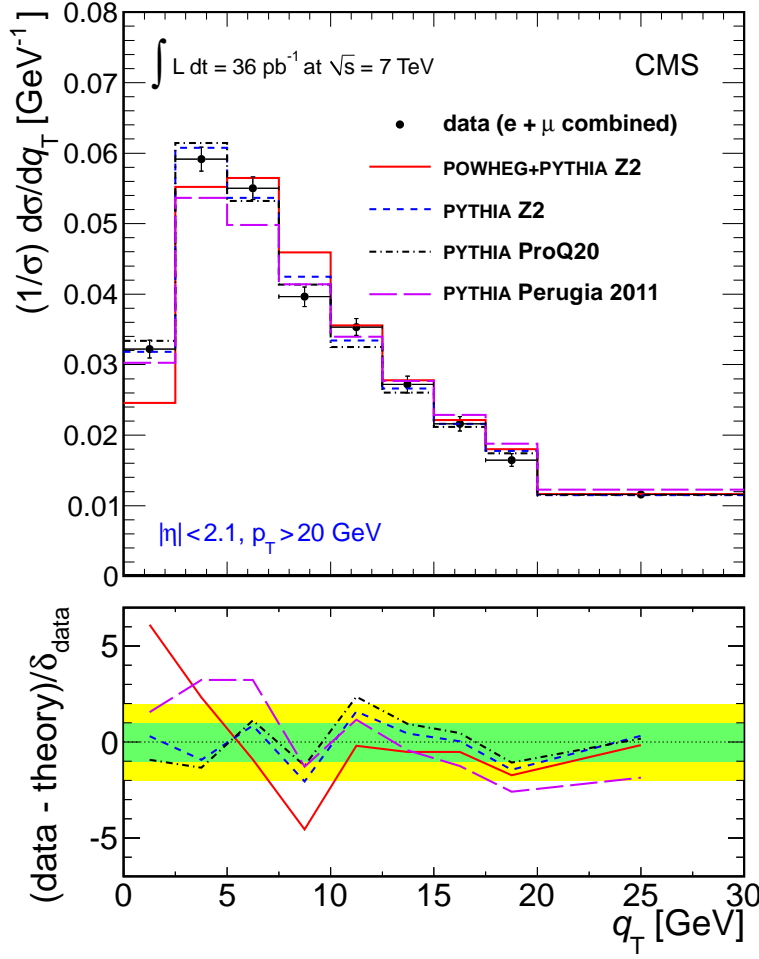


**Fig. 32** CMS [147]: The combined electron and muon measurement of the Z boson transverse momentum distribution (points) and the predictions of several PYTHIA tunes and POWHEG interfaced with PYTHIA using the Z2 tune (histograms). The error bars on the points represent the sum of the statistical and systematic uncertainties on the data. The lower portion of the figure shows the difference between the data and the simulation predictions divided by the uncertainty delta on the data. The green (inner) and yellow (outer) bands are the  $\pm 1\delta$  and  $\pm 2\delta$  experimental uncertainties.

$$\mathbf{p}_T(W) = -\mathbf{p}_T(had) = \mathbf{p}_T(l^\pm) + \mathbf{p}_T(\nu),$$

where  $p_T(had)$  denotes the hadronic recoil (Figure 35). Hence  $\mathbf{p}_T(had)$  can be used for the measurement of  $p_T(W)$ , since it reflects the underlying hadronic activity from the hard QCD interactions. The hadronic recoil has several experimental uncertainties (e.g. pile-up) and also a rather poor resolution compared to the reconstruction of leptons. Hence a data-driven model of the relation between  $\mathbf{p}_T(had)$  and  $p_T(W)$  has been used. This model is derived from Z boson events, where the  $p_T(Z)$  can be directly determined via the decay lepton measurements with a sufficiently good resolution. It is then assumed that the dependence of the hadronic

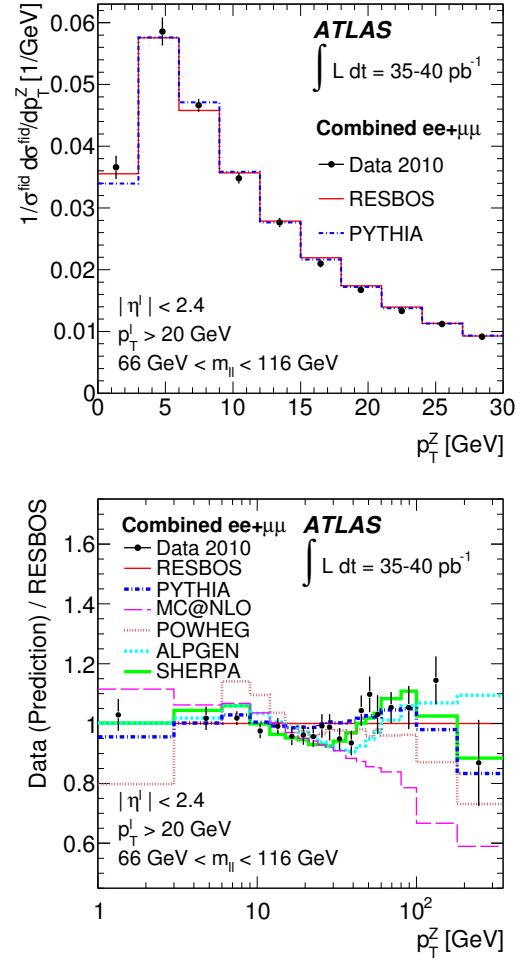


**Fig. 33** ATLAS [148]: The combined normalised differential cross-section as a function of  $p_T(Z)$  for the range  $p_T(Z) < 30$  GeV compared to the predictions of RESBOS and PYTHIA. Ratios of the combined data and predictions from different generators over the RESBOS prediction for the normalised differential cross-section are shown below.

recoil to the transverse momentum of the vector boson is the same in W and Z boson events. The unfolding is performed with a Bayesian approach. The resulting differential cross-section, which has been normalised to the fiducial cross-section measured in the phase space defined via  $p_T^l > 20$  GeV,  $|\eta_l| < 2.4$ ,  $p_T^\nu > 25$  GeV and  $m_T > 40$  GeV, is shown in Figure 36. It should be noted that the poor resolution of  $\mathbf{p}_T(had)$  implies a significantly larger binning to ensure a stable unfolding procedure. The systematic uncertainties of the data-driven modelling of  $\mathbf{p}_T(had)$  during the unfolding procedure dominate the overall uncertainties up to  $p_T(W) < 75$  GeV. Statistical uncertainties start to dominate for larger  $p_T(W)$  values. This measurement has not yet been repeated for the 2011 data sample, as the increase of

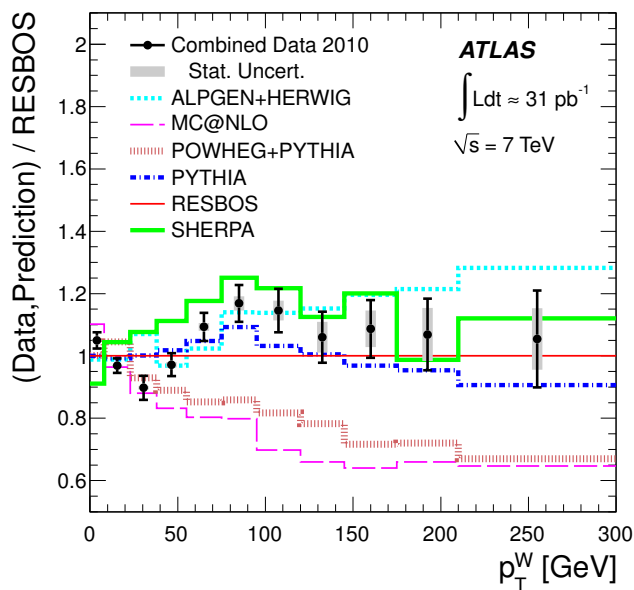


**Fig. 36** ATLAS [151]: Ratio of the combined measurement of  $p_T(W)$  and various predictions to the RESBOS prediction for the normalised differential cross-section from different generators.

pile-up further reduces the resolution of  $\mathbf{p}_T(had)$  and hence complicates the unfolding procedure when aiming at a similar binning for the low  $p_T(W)$  region. The comparison to the prediction based on RESBOS for both,  $p_T(W)$  and  $p_T(Z)$ , (Figure 33, 36), shows a significant disagreement and hence will allow for an improved tuning of the underlying MC generators.

A comparison of the published  $p_T(Z)$  distributions of ATLAS and CMS is shown in Figure 38. We extrapolated the ATLAS results to the CMS fiducial volume, while the CMS results have been corrected to the ATLAS binning to allow for a direct comparison. A slight tension can be observed for  $p_T(Z) < 10$  GeV which is not yet significant.

In summary, a new tune of generators like PYTHIA is needed in order to describe the deviations between measurement and simulations. First measurements of the Z boson transverse momentum distribution at  $\sqrt{s} = 8$  TeV based on a very reduced data set have also become available [152]. The expected measurements of the full 2012 data set at  $\sqrt{s} = 8$  TeV could also allow to test electroweak corrections which are predicted to become sizeable at large transverse momenta. In addition, the higher statistics will allow for the measurement of angular coefficients in the Drell-Yan production, as introduced in Section 2.8 (Equation 26), in up to three dimensions. Figure 37 shows the POWHEG and MC@NLO prediction of  $A_0$  vs. the transverse momentum of the Z boson. The observed discrepancy between both generators could be due to the difference in the matching scheme of NLO calculations and the underlying parton shower model (see Section 2.7.3). Therefore a precise measurement

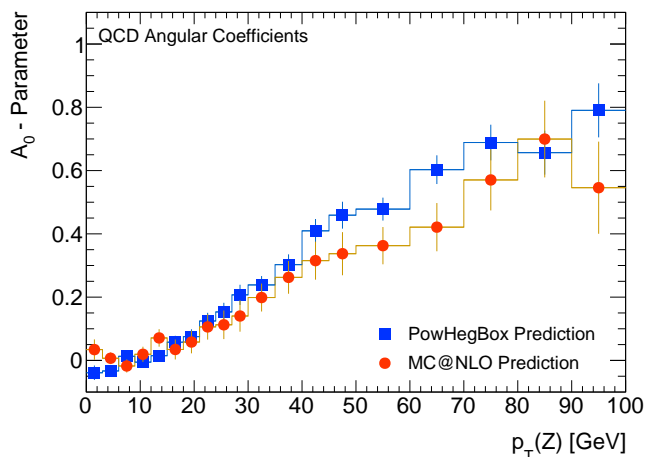


**Fig. 37** Predictions by MC@NLO and POWHEGBOX of the QCD angular parameters  $A_0$  (left) and  $A_2$  (right) in Z boson events vs. the transverse momentum of the Z boson.

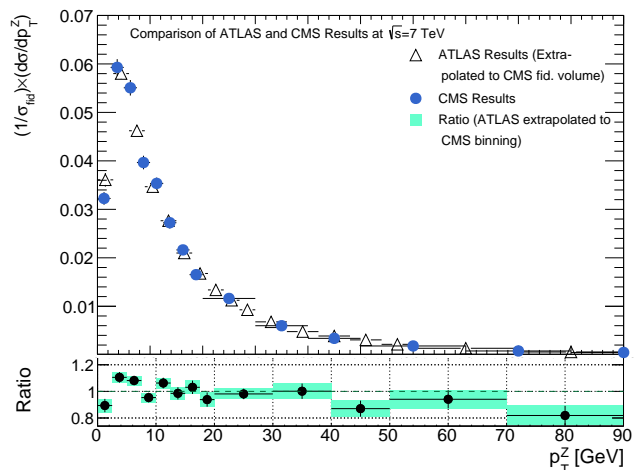


**Fig. 38** Comparison of the results of the transverse momentum measurement of the Z boson for ATLAS and CMS. The ATLAS results have been extrapolated to the CMS fiducial volume. The CMS results have been corrected to the ATLAS binning for the direct comparison.

of the angular correlations with the available  $\sqrt{s} = 8$  TeV data sample is mandatory to test this important aspect in modern QCD calculations.

#### 6.4 Determination of $\Gamma_W$

The measurement of the ratio  $R$  of leptonic rates for the inclusive production of W and Z bosons at the LHC, as discussed in the previous section, can be written as

$$R = \frac{\sigma(pp \rightarrow W + X)}{\sigma(pp \rightarrow Z + X)} \cdot \frac{\Gamma(Z)}{\Gamma(Z \rightarrow l^+l^-)} \cdot \frac{\Gamma(W^\pm \rightarrow l^\pm\nu)}{\Gamma(W)} \quad (46)$$

The inclusive cross-section ratio is known to NNLO in  $\alpha_s$  and has a numerical value of  $\sigma_W/\sigma_Z = 3.34 \pm 0.08$  [153]. The leptonic branching ratio for the Z boson  $BR(Z \rightarrow l^+l^-)$

is known to be  $(3.366 \pm 0.002)\%$  from the LEP and SLC experiments [35]. Hence, the measurement of  $R$  allows for an indirect determination of the leptonic  $W$  boson branching ratio  $BR(W \rightarrow l^\pm \nu) = \frac{\Gamma(W^\pm \rightarrow l^\pm \nu)}{\Gamma(W)}$ .

The CMS analysis [133] used the measured ratio  $R = \sigma(W^\pm \rightarrow l^\pm \nu)/\sigma(Z \rightarrow l^+ l^-) = 10.54 \pm 0.19$  leading to an indirect determination of

$$BR(W \rightarrow l^\pm \nu) = 0.106 \pm 0.003$$

In addition, the partial leptonic decay width of the  $W$  boson can be calculated within the Standard Model and is given by

$$\Gamma(W \rightarrow e \bar{\nu}_e) = \frac{G_F M_W^3}{6\pi\sqrt{2}} (1 + \delta_l^{SM}) = 226.2 \pm 0.2 \text{ MeV},$$

where corresponding electroweak corrections  $\delta_l^{SM}$  are small, since they are largely absorbed in  $G_F$  and  $m_W$  [154]. Therefore the  $W$  boson width can be extracted via  $BR(W \rightarrow l^\pm \nu)$  and results in

$$\Gamma_W = 2144 \pm 62 \text{ MeV},$$

which is consistent with the current world average  $\Gamma_W = 2085 \pm 42 \text{ MeV}$ .

A combination of the ATLAS and CMS results on the cross-section ratio could reduce the overall uncertainty by  $\approx 20\%$ , when assuming no correlations between the systematic uncertainties. This would lead to an uncertainty on  $\Gamma_W$  of 50 MeV and hence would lead to a significant reduction of the uncertainty on the current world average.

## 6.5 Forward-backward asymmetries of the $Z$ boson

The study of the Drell-Yan production at the LHC does also provide information on the weak mixing angle. This measurement is complementary to the  $Z$ -pole analyses of the LEP experiments [155], [156].

The differential cross-section for an  $f\bar{f} \rightarrow f'f'$  annihilation process<sup>8</sup> at lowest order for a  $Z$  boson exchange is given by

$$\frac{d\sigma}{d\cos\theta} = \frac{N_C^f G_F^2 m_Z^4}{16\pi} \frac{s}{(s - m_Z^2)^2 + \frac{s^2}{m_Z^2} \Gamma_Z^2} \cdot [(v_f^2 + a_f^2)(v_{f'}^2 + a_{f'}^2)(1 + \cos^2\theta) + 2v_f a_f v_{f'} a_{f'} \cdot \cos\theta] \quad (47)$$

$$\frac{d\sigma}{d\cos\theta} = \kappa[A \cdot (1 + \cos^2\theta) + B \cdot \cos\theta] \quad (48)$$

<sup>8</sup>with  $f \neq f'$  since no t-channel contributions should be allowed

where  $\cos\theta$  is the angle between the incoming and outgoing fermions<sup>9</sup>, and  $a_f$  and  $v_f = a_f \cdot (1 - 4|q_f| \sin^2\theta_W)$  are the axial and vector-axial couplings to the  $Z$  boson and  $q_f$  is the fractional charge of the fermion. Several things should be noted. First of all, the  $(1 + \cos^2\theta)$  dependence would also appear in a pure  $\gamma$  exchange diagram. However, the vector- and axial-vector couplings of the  $Z$  boson introduce an additional  $\cos\theta$  dependence. Secondly, the differential cross-section depends only on the weak mixing angle  $\sin^2\theta_W$ , when fixing the electric charges, the weak-hypercharges,  $m_Z$ , and  $\Gamma_Z$  for a given center-of-mass energy. By defining forward and background cross-sections in terms of the angle of the incoming fermions,

$$\sigma_F = \int_0^1 \frac{d\sigma}{d\cos\theta} d\cos\theta, \quad \sigma_B = \int_{-1}^0 \frac{d\sigma}{d\cos\theta} d\cos\theta,$$

where the angle  $\theta$  is defined in the CS frame as introduced in Section 2.8.1, a measure for the asymmetry at  $\cos\theta = 0$  can be defined as

$$A_{FB} = \frac{\sigma_F - \sigma_B}{\sigma_F + \sigma_B}$$

also known as the forward-backward asymmetry parameter  $A_{FB}$ . At tree level,  $A_{FB}$  is given by

$$A_{FB} = \frac{16}{3} \cdot \frac{(1 - 4|q_f| \sin^2\theta_W)}{1 + (1 - 4|q_f| \sin^2\theta_W)^2} \cdot \frac{(1 - 4|q_{f'}| \sin^2\theta_W)}{1 + (1 - 4|q_{f'}| \sin^2\theta_W)^2}.$$

The measurement at the  $Z$  pole provides the most sensitive measurement as  $Z$  exchange contributes roughly 100 times more than the  $\gamma$  exchange. Therefore, only small corrections from the interference and pure  $\gamma$  exchange terms are expected. It should be noted that electroweak corrections to  $\sin\theta_W$  can be absorbed by defining an effective weak mixing angle  $\sin\theta_{eff}$  which is therefore used in the actual measurements.

The advantage of the  $A_{FB}$  measurement is that it reduces to a good approximation to a pure counting experiment, e.g. by defining

$$A_{FB} = \frac{N_{\cos\theta>0} - N_{\cos\theta<0}}{N_{\cos\theta>0} + N_{\cos\theta<0}}$$

where the number of events in the forward and backward regions are labelled as  $N_{\cos\theta>0}$  and  $N_{\cos\theta<0}$ .

The measurement of  $A_{FB}$  can also be used for the search for new physics. While the  $A_{FB}$  at the  $Z$  boson mass is used for the determination of  $\sin^2\theta_W$ , large invariant masses are governed by virtual photon and  $Z$  interference terms. A direct search for a new resonance in the electroweak section

<sup>9</sup>or between incoming and outgoing anti-fermions

via the study of the invariant mass spectra of di-lepton events might not show an excess if the new resonance has a large width. However, such a new resonance would also interfere with the Standard Model amplitudes and hence introduce a structure in the measured asymmetries  $A_{FB}$  near its mass.

Both, ATLAS and CMS have published unfolded  $A_{FB}$  measurements and also a determination of the electroweak mixing angle. In addition to the backgrounds from other processes, the measured  $A_{FB}$  is diluted by a wrong assignment of the incoming quark and antiquark. This is accounted for in both analyses using simulations and hence relies on a precise knowledge of the PDFs.

The ATLAS analysis is based on the full 2011 data sample and uses the electron and muon decay channels [157]. Since a high acceptance of  $Z$  bosons with large rapidities reduces the dilution of falsely identified quark-directions, ATLAS also includes forward electrons in their analysis. By requiring one electron with  $|\eta| < 2.4$  and allowing a second electron within  $|\eta| < 4.9$ , an acceptance for  $Z$  boson events up to  $|y_Z| < 3.6$  is achieved. The  $A_{FB}$  is measured in the same fiducial region as the  $Z$  boson inclusive measurements. A Bayesian unfolding technique was used to transform the measured raw  $\cos \theta_{CS}^*$  distribution in a given mass region to the  $\cos \theta_{CS}^*$  at parton level. The unfolding does not only remove detector effects, but also effects from QED radiative corrections. The latter lead to deformations of the di-lepton invariant mass distribution. In order to account for these corrections, the results are unfolded to Born level, i.e. the state, before any emission of final-state radiation. The unfolding is based on a PYTHIA MC sample, where NLO corrections have been applied. QED final-state radiation was accounted for by interfacing the PHOTOS generator. The  $p_T$  and  $y$  distributions of the  $Z$  boson have been reweighted to NLO QCD predictions. NLO electroweak corrections have been estimated with HORACE [158]. The resulting  $A_{FB}$  distribution for the electron decay channel including one central and one forward electron, is shown in Figure 39, where the results including forward electrons are denoted as  $CF$ . Dominating systematic uncertainties arise from the limited knowledge of electron identification efficiencies in the forward region, NLO QCD effects and PDF uncertainties.

The effective electroweak mixing angle was not determined from the unfolded distributions but measured directly from the raw-data distributions. The measured  $A_{FB}$  spectra have been compared to MC predictions which have been produced by varying initial values for  $\sin^2 \theta_{eff}$ . Each prediction was compared to the measured distribution via a  $\chi^2$  test. The minimum of the resulting  $\chi^2$  distribution yields then the measured  $\sin^2 \theta_{eff}$  value. The combination for all channels results in

$$\begin{aligned} \sin^2 \theta_{eff} &= 0.2297 \pm 0.0004(stat) \pm 0.0009(syst.) \\ &= 0.2297 \pm 0.001, \end{aligned}$$

in agreement with the current world average of  $\sin^2 \theta_{eff} = 0.23153 \pm 0.00016$ .

The CMS study of the  $A_{FB}$  is also based on the full 2011 data sample [159] and the same fiducial volume as the inclusive measurement in both decay channels. The  $A_{FB}$  has been measured in four different rapidity regions (0 to 1, 1 to 1.25, 1.25 to 1.5 and 1.5 to 2.4) and ten mass regions ranging from 40 GeV to 400 GeV, leading to 40 measurements in total. The mass spectra of forward and backward events are unfolded independently for each rapidity region using an inverted response matrix approach. The response matrix is based on a NLO MC predictions from POWHEG and PYTHIA. Also the PYTHIA model for final-state radiation has been used. Similar to ATLAS, the unfolding procedure corrects not only for detector effects but also gives the number of forward and backward events on Born level. The resulting  $A_{FB}$  distribution for the combination of both decay channels in the most forward region is shown in Figure 40. Dominating systematic uncertainties are due PDFs in the central rapidity regions and due final state radiation modelling uncertainties in the forward region. Overall, a good agreement with the NLO prediction by POWHEG is observed for all kinematic regions.

The measurement of  $\sin^2 \theta_W$  by the CMS experiment is based exclusively on the muon decay channel with an integrated luminosity of  $1.1 \text{ fb}^{-1}$  [160]. CMS focuses on the muon decay channel because of the smaller background uncertainties and a better understanding of the corresponding detector performance. The actual methodology for the  $\sin^2 \theta_W$  measurement is different from ATLAS. CMS uses an unbinned extended maximum likelihood function which is fitted to data in order to extract the effective weak mixing angle. The likelihood function is evaluated on an event-by-event basis and depends on the number of signal and background events and the expected event the probability density functions for the signal and background processes. These probability densities are parameterised as a function of the di-lepton rapidity, the di-lepton invariant mass, their decay angle  $\cos \theta^*$  and the weak mixing angle and rely on leading order predictions of PYTHIA, leading order PDF set and a full detector simulation. The impact of NLO effects has been estimated. The minimisation of the likelihood functions leads to a measured value of

$$\begin{aligned} \sin^2 \theta_{eff} &= 0.2287 \pm 0.0020(stat) \pm 0.0025(syst.) \\ &= 0.2287 \pm 0.003, \end{aligned}$$

also in agreement with the current world average [155]. A summary of the systematic uncertainties of the ATLAS and

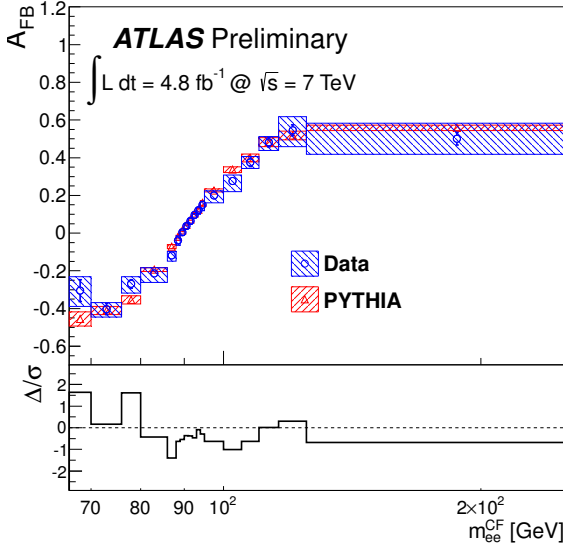


**Fig. 39** ATLAS [157]:  $A_{FB}$  unfolded to Born-level central-forward electrons. For the data, the boxed shaded region represents the total (statistical+systematic) uncertainty and the error bars represent the statistical uncertainty. The boxed shaded regions for the PYTHIA predictions represent the statistical uncertainty only. The ratio plots at the bottom display the distribution of pulls.

**Table 11** Summary of the ATLAS and CMS measurements of the weak mixing angle  $\sin^2\theta_{eff}$ , together with the associated uncertainties and the current world average

	ATLAS	CMS	World Average
$\sin^2\theta_{eff}$	0.2297	0.2287	0.23153
Total uncertainty	0.0010	0.0032	0.00016
Stat. uncertainty	0.0004	0.0020	-
Sys. uncertainty	0.0009	0.0025	-
PDF	0.0007	0.0013	-
Modelling+FSR	0.0005	0.0016	-
Detector effects	0.0005	0.0013	-

CMS measurements is shown in Table 11. The dominating uncertainty for ATLAS comes from PDF uncertainties. Also at CMS, theoretical uncertainties due to PDF, FSR and NLO corrections dominate. The remaining experimental uncertainties could be in principle reduced by future studies. Hence a competitive measurement of  $\sin^2\theta_W$  at the LHC relies on a significant improvement of the proton PDFs.

## 6.6 Polarisation measurement of $W$ bosons

The measurement of the angular distribution of  $W \rightarrow \mu\nu$  and  $W \rightarrow e\nu$  events allows for the determination of the  $W$  boson polarisation in proton-proton collisions. The theoretical basis of this measurement was introduced in Section 2.8 and relies on Equation 26. This can be rewritten in terms of the

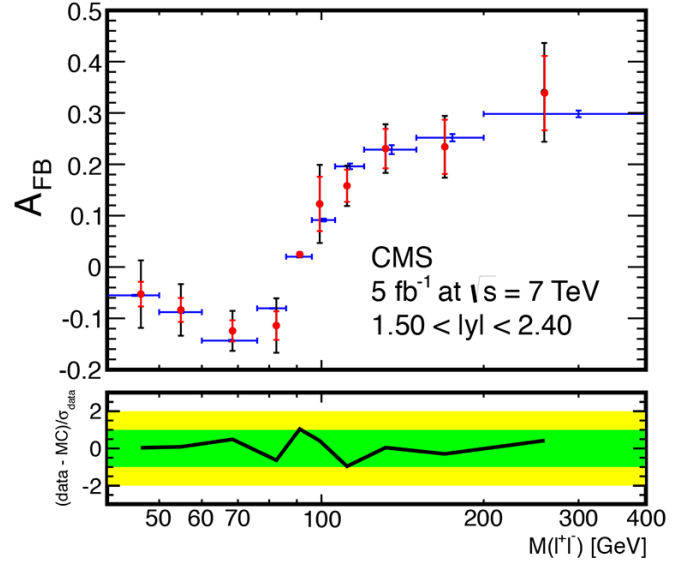


**Fig. 40** CMS [159]: The unfolded and combined measurement of  $A_{FB}$  at the Born level with  $1.5 < |y| < 2.4$  and  $p_T > 20$  GeV. The data points are shown with both statistical and combined statistical and systematic error bars. The error bars on the MC prediction points are due to PDF uncertainties. The MC prediction statistical errors are of the same order of magnitude as the PDF uncertainties.

fractions of left-handed, right-handed and longitudinal polarised  $W$  bosons,  $f_L$ ,  $f_R$  and  $f_0$ , which is given by

$$\frac{1}{\sigma} \frac{d\sigma}{d\cos\theta} = \frac{3}{8} f_L (1 \mp \cos\theta)^2 + \frac{3}{8} f_R (1 \pm \cos\theta)^2 + \frac{3}{4} f_0 \sin^2\theta$$

where the superscripts  $\pm$  relate to the charge of the  $W$  boson. By definition,  $f_i > 0$  and  $f_L + f_R + f_0 = 1$  must hold. The parameters  $f_i$  are not expected to be the same for  $W^+$  and  $W^-$  in proton-proton collisions, as the ratio of valence  $u$  quarks to sea quarks is higher than for valence  $d$  quarks. Hence different angular distributions are expected.

The choice of an appropriate reference frame is not trivial, as the  $W$  boson rest frame can be only defined by the full four-momentum information of both decay leptons. While the four-momentum information of the muon is present, only the transverse momentum of the neutrino can be measured. In principle, its longitudinal component can be determined through the  $W$  mass constraint. However, the corresponding equations lead to two possible solutions thus an unambiguous choice is not possible. Therefore, the measurement is based on a highly correlated variable  $\cos\theta_{2D}$ , defined as

$$\cos\theta_{2D} = \frac{\mathbf{p}_T^{l*} \cdot \mathbf{p}_T^W}{|\mathbf{p}_T^{l*}| \cdot |\mathbf{p}_T^W|},$$

where  $\mathbf{p}_T^{l*}$  is the transverse momentum of the lepton in the transverse  $W$  boson rest frame and  $\mathbf{p}_T^W$  is the transverse momentum of the  $W$  boson in the laboratory frame. The observ-



able  $\cos \theta_{2D}$  can be interpreted as the 2-dimensional projection of  $\cos \theta$  on the transverse plane. The helicity fractions can then be determined by fitting the measured  $\cos \theta_{2D}$  distributions with a weighted sum of templates obtained from the simulations. Each template corresponds to one helicity state and is weighted by the corresponding  $f_i$  value.

The ATLAS measurement of the polarisation of  $W$  bosons is based on  $\int \mathcal{L} dt = 35 \text{ pb}^{-1}$  of the 2010 data sample [161]. The selection of signal events and the background determination methods are similar to the inclusive measurement. In addition it is required that the transverse  $W$  boson mass is within a range of  $50 \text{ GeV} < m_{\text{T}}^W < 110 \text{ GeV}$ . The upper cut was chosen to reject badly reconstructed jets. In order to enhance the polarisation effects, two regions for events with a large transverse momentum of  $W$  boson have been defined as  $35 < p_{\text{T}}^W < 50 \text{ GeV}$  and  $p_{\text{T}}^W > 50 \text{ GeV}$ . The MC prediction of the  $\cos \theta_{2D}$  templates have been obtained independently from MC@NLO and POWHEG. The actual fit was performed using a binned maximum likelihood fit based on MC@NLO templates. The templates predicted by POWHEG have been used for estimating systematic uncertainties. Since only two of the three parameters  $f_i$  are independent, it was chosen to measure  $f_0$  and  $f_L - f_R$ . The results for  $p_{\text{T}}^W > 50 \text{ GeV}$  averaged over both decay channels and both charges are shown in Figure 41 together with the expectations from simulations, which agree with the measurement. The systematic uncertainties are dominated by experimental uncertainties on the measured  $p_{\text{T}}^W$ .

The CMS measurement is also based on the 2010 data sample [162] and relies on a binned maximum likelihood for the  $\cos \theta_{2D}$  variable. The fitting templates for the different helicity states are based on the MADGRAPH generator. In contrast to the inclusive measurements, CMS requires in this case a cut on the transverse mass of  $m_{\text{T}} > 50 \text{ GeV}$  for the electrons and of  $m_{\text{T}} > 30 \text{ GeV}$  for the muon channel, in order to reduce the QCD multi-jet background. In addition, also a minimal  $p_{\text{T}}^W > 50 \text{ GeV}$  is required, similar to the ATLAS analysis. The background from  $t\bar{t}$  is reduced by vetoing events with more than three reconstructed jets with a  $p_{\text{T}} > 30 \text{ GeV}$ . The resulting fit values for  $f_0$  and  $f_L - f_R$  are shown in Figure 42, independently for both  $W$  boson charges.

Both measurements show a clear difference between the left- and right-handed polarisation parameters in proton-proton collisions and are compatible with the Standard Model expectations.

## 7 Vector Boson Production in Association with Jets

The cross-sections of  $W$  and  $Z$  production for different jet multiplicities are an important measure for NLO and MC predictions but the exploratory power of measurements of  $W$ +jets and  $Z$ +jets production today lies in the precision

tests of differential distributions. The cross-section as a function of the jet  $p_{\text{T}}$  for example is a sensitive test of the scale used in  $\alpha_s$  calculations whereas the rapidity distributions of the jets is a sensitive test to different PDF sets. Studying the angular distributions between the jets, such as the rapidity differences between two jets, tests hard parton radiation at large angles. Previous publications from CDF and D0 have measured the differential cross-sections as a function of the jet  $p_{\text{T}}$ , the boson  $p_{\text{T}}$ , the angular separation between jets as well as other observables [15–17, 163, 164]. However, the kinematic reach of these measurements compared to that at the LHC is limited. For example, at the Tevatron using an integrated luminosity of  $\int \mathcal{L} dt \approx 1.7 \text{ fb}^{-1}$ , jets up to a  $p_{\text{T}}$  of 400 GeV can be measured in  $Z$ +jets events, while at the LHC using of integrated luminosity of  $\int \mathcal{L} dt \approx 4.6 \text{ fb}^{-1}$ , jets up to a  $p_{\text{T}}$  of 700 GeV can be studied. These large data samples at the LHC, allow us to make precision measurements over large regions of the phase space. In addition, we can measure in detail specific topologies, like  $Z$ +jets production where the  $p_{\text{T}}^Z$  is greater than 100 GeV or measure differential cross-sections for rare processes, like  $Z + b\bar{b}$  production.

In addition, the last five years have been an ‘NLO revolution’. At the time of the LHC turn-on, NLO calculations up to two associated jets were available, while today an NLO calculation up to six associated jets can be achieved [99]. In addition NLO calculations for  $W$  and  $Z$  production associated with heavy-flavour jets have also expanded greatly in recent years.

### 7.1 Measurements of $W$ +jets and $Z$ +jets cross-sections

At the LHC,  $W$ +jets and  $Z$ +jets production is dominated by quark-gluon interactions making these measurements different from measurements of the QCD multi-jet process, which is dominated by gluon-gluon interactions. In MC calculations, associated jets to  $W$  and  $Z$  production can arise either from the matrix-element calculation itself or from quarks or gluons in the parton showering. Jets from the matrix element tend to have a higher  $p_{\text{T}}$  compared to those from the parton shower and therefore not including multiple partons in the matrix element will result in an underestimate of the jet multiplicity cross-sections. For an excellent review on jets and their properties at hadron colliders, see [165].

Both ATLAS and CMS have performed measurements of  $Z$  production in association with jets. The ATLAS and CMS results are based on an integrated luminosity of  $\int \mathcal{L} dt \approx 4.6 \text{ fb}^{-1}$  [166] and  $\int \mathcal{L} dt \approx 4.9 \text{ fb}^{-1}$  [167], respectively. Both results measure the jet multiplicity cross-sections up to seven associated jets. Shown in Figure 43 for the ATLAS measurement, several theory predictions are compared to the data. The ALPGEN and SHERPA generators both include matrix-element calculations that cover up to five partons, with additional jets coming from the parton showering.

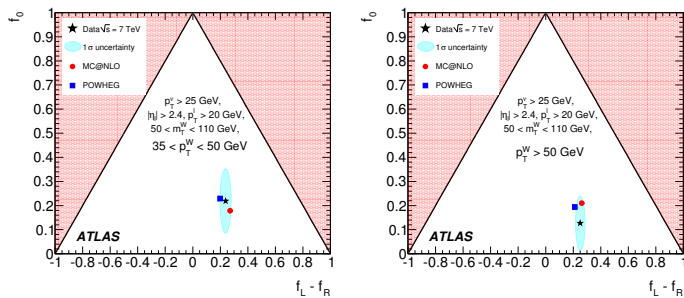


**Fig. 41** ATLAS [161]: Measured values of  $f_0$  and  $f_L - f_R$ , after corrections, within acceptance cuts for  $35 < p_T^W < 50$  GeV (left) and  $50 < p_T^W$  (right) compared with the predictions corresponding to MC@NLO and POWHEG. The ellipses around the data points correspond to one standard deviation, summing quadratically the statistical and systematic uncertainties. The forbidden region is hatched.

MC@NLO generates the Drell-Yan process at NLO and includes the real emission of one additional parton and any additional jets from the parton showering. The BLACKHAT-SHERPA results provide fixed-order calculations at NLO for up to four jets. The data is in excellent agreement with BLACKHAT-SHERPA and SHERPA predictions. ALPGEN tends to underestimate the data above five jets, as expected, since above five partons all additional jets in the predictions originate from the parton shower. While MC@NLO agrees with the data for zero-jet and one-jet events, its parton shower model underestimates the observed jet rate by a factor of two. The CMS results are also in good agreement with the BLACKHAT-SHERPA predictions as well as the MADGRAPH predictions, which includes matrix-element calculations up to four partons and the POWHEGBOX predictions, which is a NLO calculation for one jet. The dominant experimental uncertainty in both of these measurements is the uncertainty on the jet energy scale, while the dominant theory uncertainty is due to the scale uncertainties.

Taking the ratio of jet multiplicity cross-section allows for many of the experimental systematic uncertainties to cancel, thereby improving the precision of the measurement. The ratios,  $R_{(n+1)/n}$ , shown in Figure 44 for the ATLAS measurement, exhibit a constant or staircase scaling pattern, as derived in Equation 16. As described in Section 2.2.2, basic quantum field theory would predict a Poisson scaling of  $R_{(n+1)/n}$  due to successive gluon radiation from an energetic quark. At higher jet multiplicities, though, a constant value of  $R_{(n+1)/n}$  is expected due to the non-abelian nature of QCD final-state radiation, i.e. a final-state gluon can radiate an additional gluon. At low multiplicities this constant value is due to a combination of Poisson scaling and parton density suppression, where the emission of the first parton has a stronger suppression than any additional parton. This Poisson scaling can be recovered if the scale difference between the main process (such as Z+1-jet events) and the  $p_T$  of the second leading jet is large [168]. When requiring the

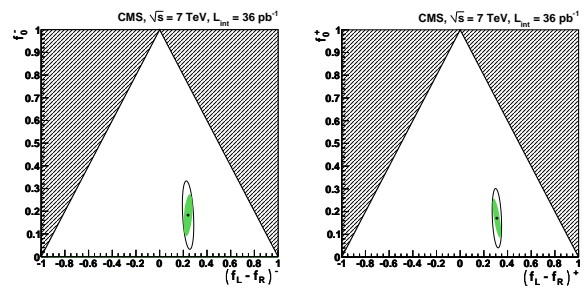


**Fig. 42** CMS [162]: The muon fit result (black dot) in the  $(f_L - f_R, f_0)$  plane for negatively charged leptons (left) and positively charged leptons (right). The 68% confidence level contours for the statistical and total uncertainties are shown by the green shaded region and the black contour, respectively. The forbidden region is hatched.

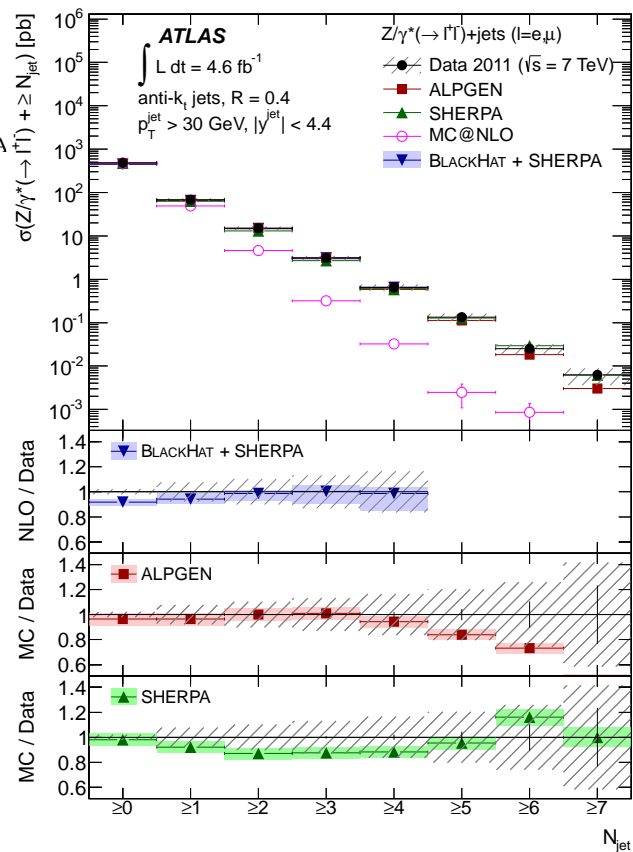


**Fig. 43** ATLAS [166]: Measured cross-section for Z+jets as a function of the number of jets. The data are compared to BLACKHAT-SHERPA, ALPGEN, SHERPA and MC@NLO.

leading jet to have  $p_T > 150$  GeV and all other additional jets to have a  $p_T > 30$  GeV, the ratio changes dramatically (Figure 44, right) and the Poisson scaling is clearly seen. The theory predictions track this trend and are all in good agreement with the data.

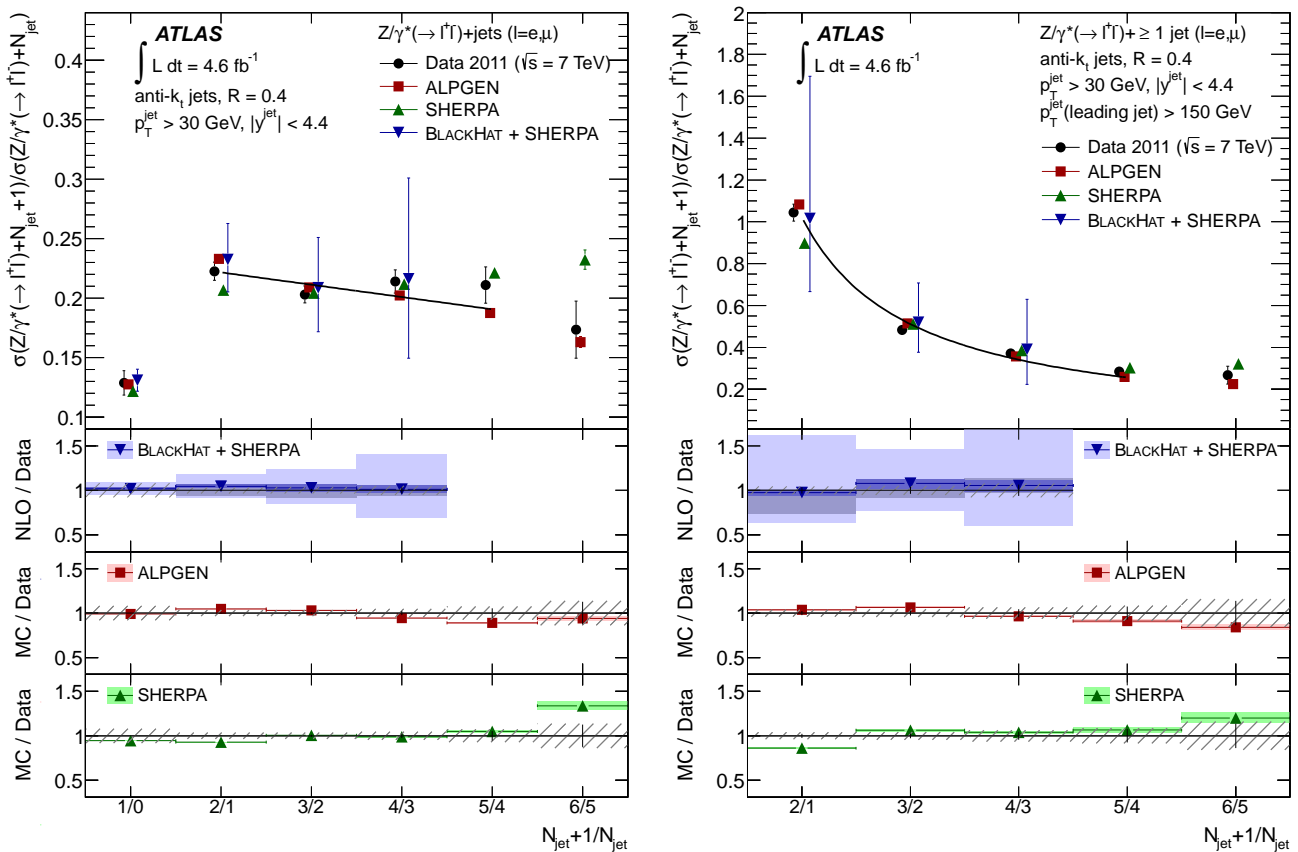


**Fig. 44** ATLAS [166]: Measurements of the ratio of cross-sections for successive exclusive jet multiplicities. The data are compared to BLACKHAT-SHERPA, ALPGEN and SHERPA predictions. Left: The standard jet selection of  $p_T > 30$  GeV is used. Right: The leading jet is required to have  $p_T > 150$  GeV while all other jets must have  $p_T > 30$  GeV.

Similarly, using a smaller data sample of  $\int \mathcal{L} dt \approx 35\text{pb}^{-1}$ , a CMS analysis [169] tested the Berends-Giele scaling hypothesis which similarly states that the ratio can be described as a constant. Since phase space effects can modify this ansatz slightly, a linear function is used  $C_n = \alpha + \beta n$ . The Berends-Giele scaling is confirmed to describe the data for events with up to four jets.

Measurements of  $W$  production in association with jets has also been performed by ATLAS [170] using an integrated luminosity of  $\int \mathcal{L} dt \approx 35\text{pb}^{-1}$  and by CMS [171] using an integrated luminosity of  $\int \mathcal{L} dt \approx 5.0\text{fb}^{-1}$ . The CMS results, performed using only  $W \rightarrow \mu\nu$  events, measured the cross-section with up to 6 associated jets (Figure 45). Similar to the  $Z$ +jets production, the data is in good agreement with the BLACKHAT-SHERPA, MADGRAPH and POWHEG predictions. The Berends-Giele scaling, measured by both ATLAS and CMS [169] at  $\int \mathcal{L} dt \approx 35\text{pb}^{-1}$ , also describes well the  $W$ +jets data up to 4-jets.

Using a common phase space, we summarise in Figure 46 the  $W$ +jets and  $Z$ +jets results from ATLAS and CMS. For the  $W$ +jets results the common phase space is one lepton with a  $p_T > 20$  GeV and  $|\eta| < 2.5$ , a neutrino from the  $W$  de-

cay with  $p_T > 25$  and the transverse mass of the  $W$  of greater than 40 GeV. For the  $Z$ +jets results the phase space is defined as two leptons each with a  $p_T > 20$  GeV and  $|\eta| < 2.5$  and invariant mass of  $66\text{ GeV} < m_{ll} < 116\text{ GeV}$ . For both  $W$  and  $Z$  production, the jets are defined using an anti- $k_T$  algorithm with a distance parameter of  $R = 0.5$ , a  $p_T > 30$  GeV and a rapidity less than 2.4. The correction factors applied to both the ATLAS and CMS results are derived from SHERPA and range from 1% to 23%. For all jet multiplicities, the correction factors are smaller than the experimental systematic uncertainties.

In summary measurements of the cross-sections of  $W$  and  $Z$  production in association with jets are in excellent agreement with the predictions. For measurements of the cross-section ratios of  $R_{(n+1)/n}$  the experimental uncertainties are much smaller compared to those from the theory predictions. Future measurements should therefore focus on differential measurements of the cross-section to further test perturbative QCD theory.

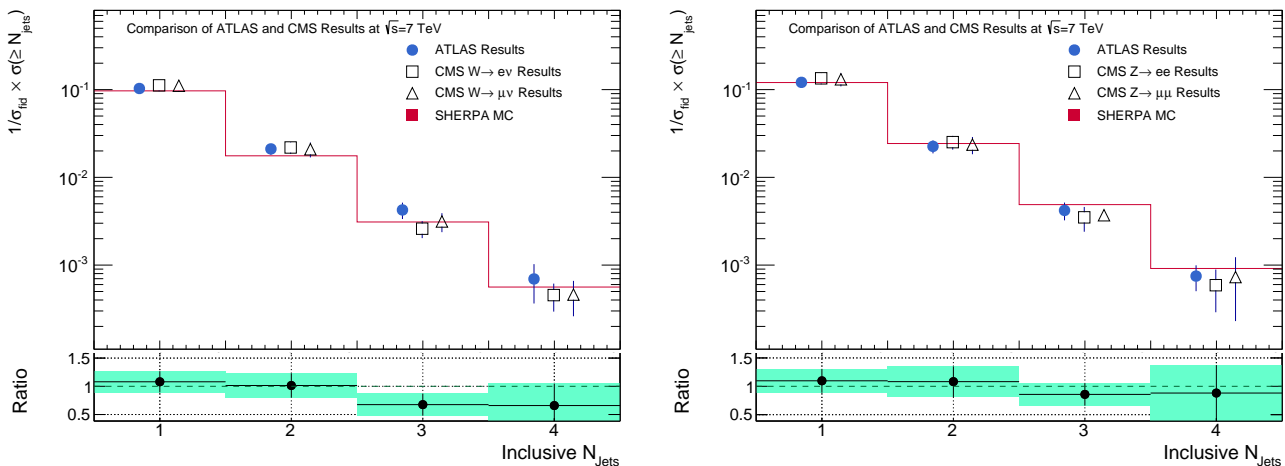


**Fig. 46** Summary of the  $W$ +jets (left) and  $Z$ +jets (right) cross-sections as a function of the number of jets. Both the ATLAS [166, 170] and CMS [169] results have been corrected to a common phase space as described in the text. The cross-sections for each jet multiplicity have been normalised by the inclusive  $W$  or  $Z$  cross-section. The CMS results shown here use an integrated luminosity of  $\int \mathcal{L} dt \approx 35 \text{pb}^{-1}$ , as the most recent CMS results are not yet published. The ratio between the ATLAS and combined CMS results are shown below. Predictions from SHERPA are also shown.

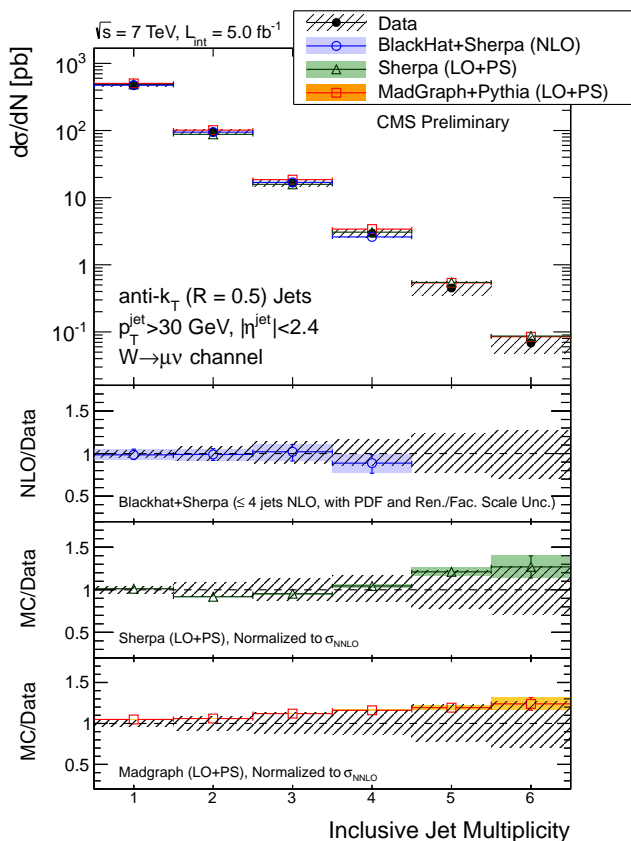


**Fig. 45** CMS [171]: Measured cross-section for  $W$ +jets as a function of the number of jets. The data are compared to BLACKHAT-SHERPA, SHERPA and MADGRAPH.

## 7.2 Differential $W$ +jets and $Z$ +jets measurements

Differential measurements of the properties of the jets in  $W$ +jets and  $Z$ +jets events probe not only perturbative QCD theory, but are also sensitive to renormalisation scales, PDFs and hard parton radiation at large angles. For these measurements, ATLAS and CMS have two major advantages. First, with large data samples very high jet  $p_T$  and scalar sum scales can be probed. Second, the detectors can measure jets at large rapidities. Both the high  $p_T$  and large rapidity jet phase spaces have not been extensively measured in the past.

The differential cross-section of both  $W$  or  $Z$  events as a function of  $H_T$  is of particular interest. In the CMS measurements  $H_T$  is defined as the scale sum of all jets passing the selection criteria. In many fixed-order calculations,  $H_T$  is often used as the value of the renormalisation and factorisation scales. It is also an observable that is very sensitive to missing higher-order terms in theoretical predictions as well as an observable which is often used in searches for new physics. The effect of missing higher-order terms in the predictions can readily be seen in Figure 47, which shows the differential cross-section as a function of  $H_T$  for  $W + \geq 1$ -jet events. At large values of  $H_T$ , the NLO BLACKHAT-SHERPA predictions underestimate the data. This is because of the limited order of the BLACKHAT-SHERPA calculations which do not include matrix-element calculations of three or more real emissions. Modifying BLACKHAT-SHERPA to include higher-order NLO terms to the  $N_{jet} \geq 1$  predictions yields good agreement to the data [170]. The SHERPA predictions shows better agreement to the data, compared to MADGRAPH.

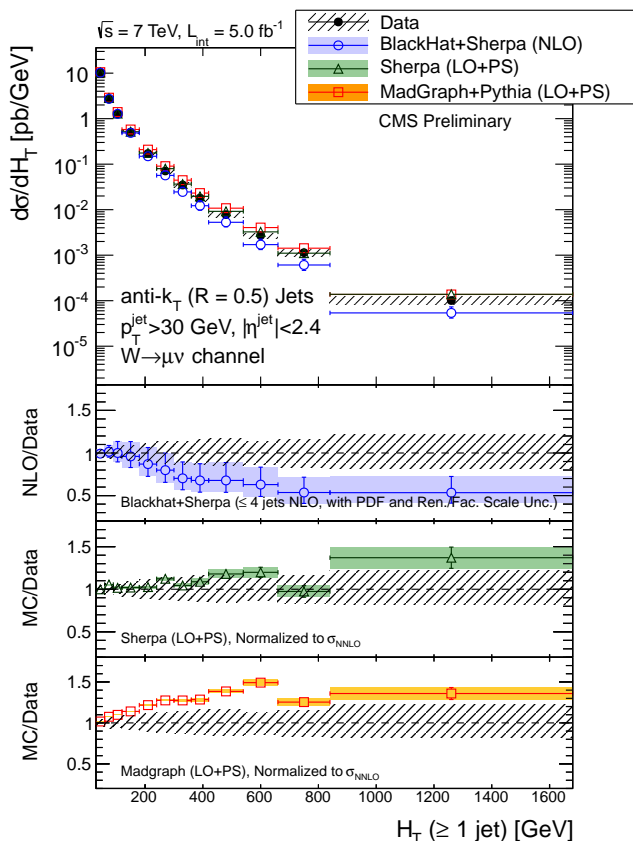


**Fig. 47** CMS [171]: Differential cross-section as a function of  $H_T$  for  $W + \geq 1$ -jet events. Predictions are shown for SHERPA, MADGRAPH and BLACKHAT-SHERPA.

The discrepancy between data and predictions in the  $H_T$  distribution, which is attributed to missing higher jet multiplicities in fixed-order calculations, can be further investigated by comparing the average jet multiplicity as a function of the  $H_T$ . Figure 48 shows that for higher values of  $H_T$ <sup>10</sup>, the average jet multiplicity increases. Therefore at large values of  $H_T$ , a fixed-order calculation for only  $N_{jet} = 1$ , will not model correctly the data and agreement to the data can only be restored when including higher jet multiplicities. This conclusion is especially important for searches for new physics which rely on simulations to predict the number of  $W$  and  $Z$  background events with large values of  $H_T$ . Using simulations with an insufficient number of partons in the final state will lead to an underestimate the number of  $W$  and  $Z$  events at high values of  $H_T$ .

When the  $p_T$  of the jet is larger than the mass of the  $Z$  or  $W$  boson, the NLO to leading-order correction factors become large due to QCD corrections, which are of the order  $\alpha_s \ln^2(p_T/m_Z)$ . Also at high values of the jet  $p_T$ , the electroweak corrections, which are usually small compared to QCD corrections, can also reduce the cross-section by 5-

<sup>10</sup>ATLAS measurements define  $H_T$  as the scalar sum of all jets and leptons in the event.

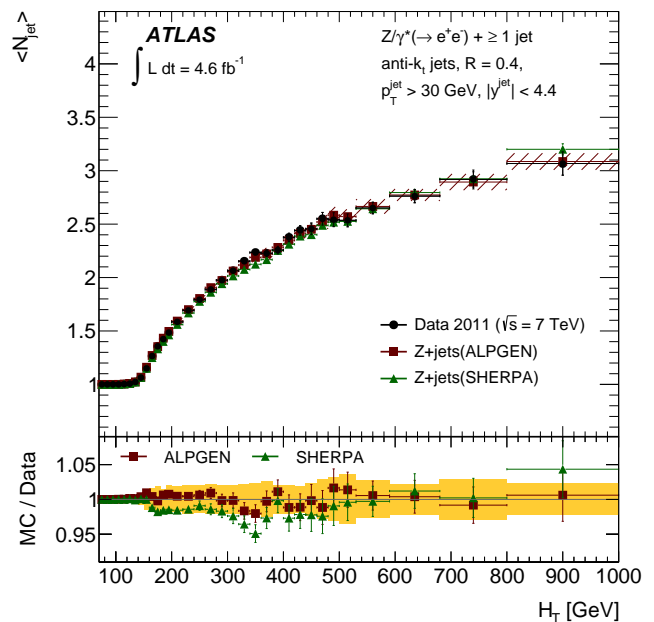


**Fig. 48** ATLAS [166]: The average number of jets,  $\langle N_{jet} \rangle$ , in  $Z \rightarrow ee$  events with jets as a function of the  $H_T$ . ALPGEN and SHERPA predictions are also shown.

20% for  $100 \text{ GeV} < p_T^H < 500 \text{ GeV}$  [172]. The differential cross-section as a function of the leading jet  $p_T$  for  $Z$  events with  $N_{jet} \geq 1$  measured by the CMS experiment is shown in Figure 49. The experimental systematic uncertainties are smaller than those of the theoretical predictions. The NLO predictions from BLACKHAT-SHERPA are consistent with the data, while POWHEG tends to predict slightly harder jet spectra. MADGRAPH also slightly models incorrectly the shape of the data.

The differential cross-sections as a function of the  $Z$  boson and jet rapidities for  $Z+1$  jet events was performed by the CMS collaboration [173]. Since  $Z$ +jets production involves a relatively high momentum valence quark and a low momentum gluon or quark, the  $Z$  boson and jet are usually produced in the same end of the detector, which implies that the rapidity of the jet and the  $Z$  boson in one-jet events is highly correlated. Measuring the rapidity sum,  $y_{sum} = |y_Z + y_{jet}|$ , between the jet and the  $Z$  boson is therefore sensitive to the PDFs while the rapidity difference  $y_{dif} = |y_Z - y_{jet}|$  is sensitive to the leading-order parton differential cross-section. These results are shown in Figure 50. SHERPA models the data well, whereas the MADGRAPH and MCFM predictions are less consistent with the data. The differences between the different predictions is most clearly seen in the  $y_{dif}$  distribution where SHERPA best models the data.

The large data samples of the LHC also allow for precision measurements at high scales. One topological observable of interest in many searches for new physics is the event thrust, which is defined as

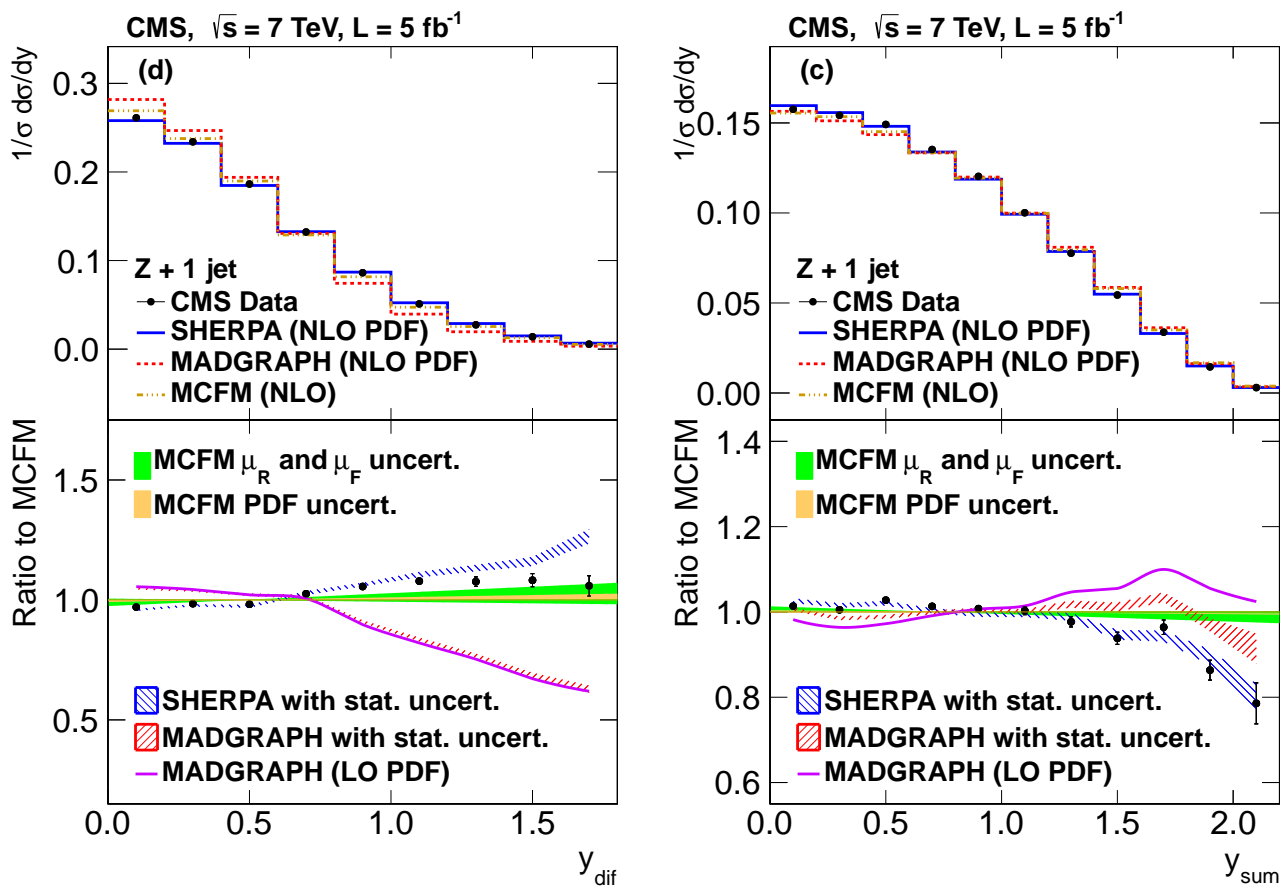


**Fig. 50** CMS [173]: Differential cross-sections as a function of rapidity sum,  $y_{sum}$  (right) and rapidity difference,  $y_{dif}$  between the Z boson and the leading jet. The distributions are normalised to unity. The lower panel gives the ratios of data and the SHERPA and MADGRAPH simulations to the MCFM predictions.

$$\tau_T \equiv 1 - \max \frac{\sum_i |\mathbf{p}_{T,i} \cdot \mathbf{n}_\tau|}{\sum_i p_{T,i}},$$

where the index  $i$  is over all jets and the Z boson,  $\mathbf{p}_{T,i}$  is the transverse momentum of object  $i$  and  $\mathbf{n}_\tau$  is the unit vector that maximises the sum. In events where the Z and the jet are back-to-back, the thrust is zero. For events with additional jets that are isotropically distributed, the value of the thrust becomes larger. Traditionally the results are presented as  $\ln \tau_T$ , so that back-to-back events have a value approaching infinite and isotropic events have a value of  $-1$ . CMS measured the differential cross-section as a function of the thrust in two different phase spaces [174]: an inclusive phase space with  $p_T^Z > 0$  GeV and a phase space region with  $p_T^Z > 150$  GeV. Similar to measurements of the jet  $p_T$ , applying a cut on the  $p_T^Z$  tests perturbative QCD theory in a region of phase space where the QCD corrections can be large. As seen in Figure 51, the predictions are within 10-15% of the data in the inclusive phase space, except for PYTHIA which shows large deviations. In the phase space

region with large  $p_T^Z$ , the agreement with PYTHIA improves but both PYTHIA and SHERPA tend to predict more events in back-to-back topologies compared to the data.

A measure of the hadronic activity accompanying  $W$  production can be investigated by studying the *splitting scales* in the  $k_T$  cluster sequence [175]. These splitting scales are determined by the clustering of objects, either calorimeter energy deposits or particle-level hadrons, according to their distance from each other. The final splitting scale in the clustering sequence, called  $d_0$ , is the hardest scale and corresponds to the  $p_T$  of the jet. Studying the hardest splitting scales is therefore like studying the  $k_T$  jet algorithm clustering in reverse. Since this algorithm clusters the soft and collinear branchings first, this clustering sequence is akin to studying the QCD evolution in reverse<sup>11</sup>. The results of the hardest splitting scale,  $d_0$  are shown in Figures 52 and compared to MC@NLO, ALPGEN, SHERPA and POWHEG predictions. Although there is reasonable agreement to the data, the NLO predictions do not describe well the high tail

<sup>11</sup>This is not case for the anti- $k_T$  algorithm which clusters the collinear branchings first but not the soft emissions.

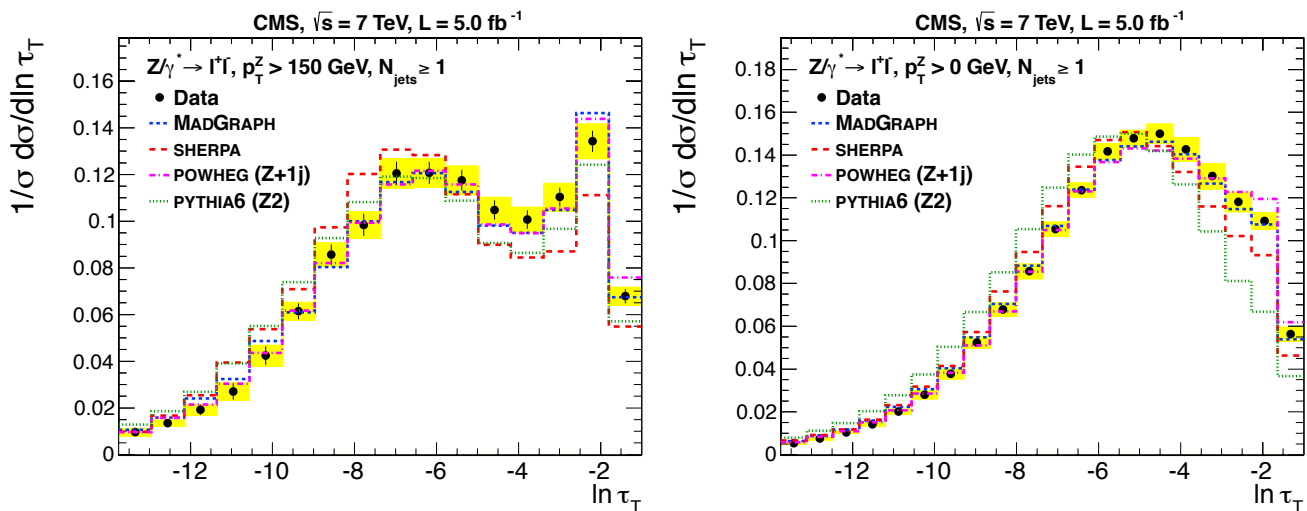


**Fig. 51** CMS [174]: Differential cross-sections as a function of the  $\ln \tau_T$  for Z+jets events. The distributions are normalised by the inclusive  $Z \rightarrow ll$  cross-section. MADGRAPH, SHERPA, POWHEG and PYTHIA predictions are shown.

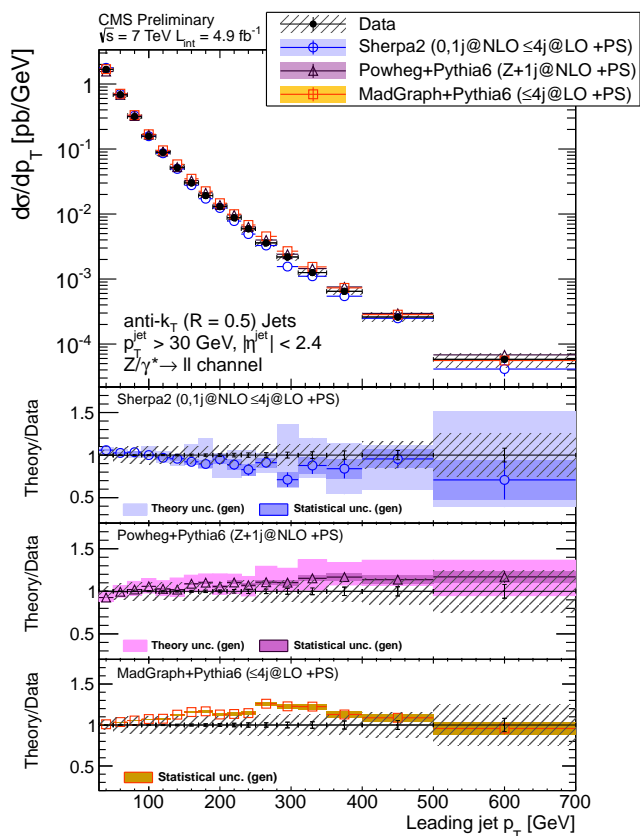


**Fig. 49** CMS [167]: Differential cross-section as a function of the leading jet  $p_T$  for Z+jets events. Predictions are shown for POWHEG, MADGRAPH and BLACKHAT-SHERPA.

even though the leading-order accuracy for all of these generators should be the same. This study, which also includes measurements that are sensitive to the hadronisation effects

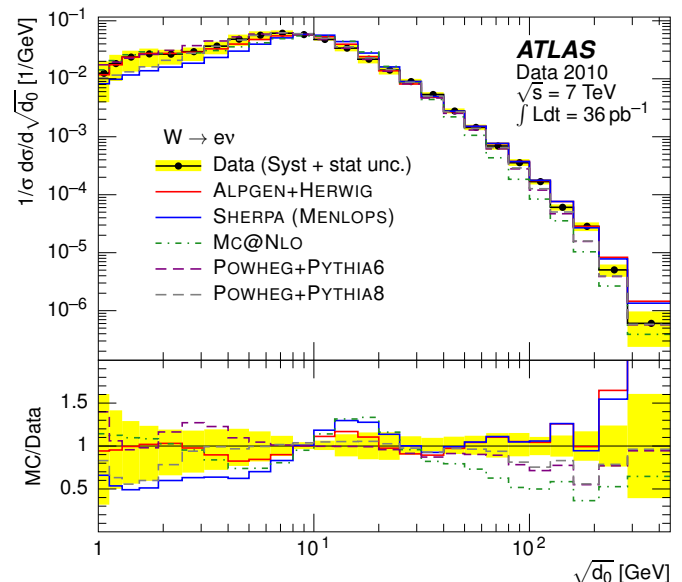


**Fig. 52** ATLAS [175]: Distribution of the hardest splitting scale ( $d_0$ ) in the  $k_T$  clustering sequence for  $W \rightarrow e\nu$  events. The data are compared to the MC@NLO, ALPGEN, SHERPA and POWHEG predictions. The yellow bands represent the combined statistical and systematic uncertainties. The histograms are normalised to unit area.

and multiple parton interactions, can be used to help tune these generators in the future.

With the large data sets available from the LHC, both the ATLAS and CMS collaborations have studied extensively differential cross-sections for  $W$  and  $Z$  production in association with jets. These measurements have highlighted a few features. First, at large values of  $H_T$  the predictions must include a sufficient number of partons in the matrix-element calculation in order to model the data correctly, even at low jet multiplicities. Second, the experimental precision of mea-

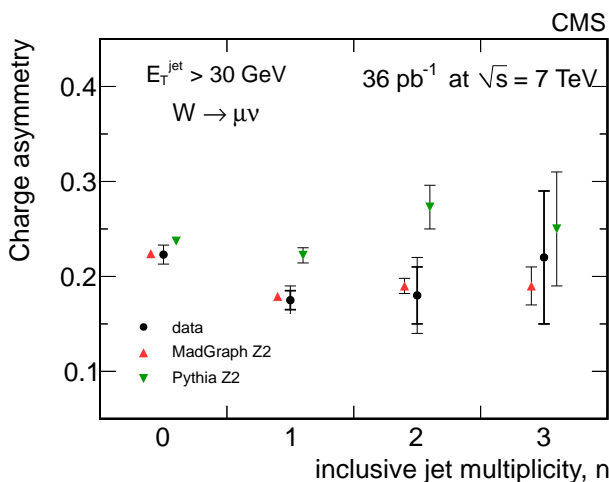


**Fig. 53** CMS [169]:  $W$  charge asymmetry  $A_W$  as a function of the jet multiplicity for  $W \rightarrow \mu\nu$  events. MADGRAPH and PYTHIA predictions are also included.

measurements such as the  $Z$  boson differential cross-section as a function of leading jet  $p_T$  can test not only QCD corrections but for the first time become sensitive to the QED corrections in one-jet events. Future measurements with higher transverse momenta of the jets and the boson will be able to better probe these large QCD corrections at these high values of  $p_T$  as well as be able to make qualitative statements about the accuracy of the QED corrections.

### 7.3 Measurements of the ratio of $W^+$ to $W^-$ in association with jets

As discussed in Section 6.2, the  $W^\pm$  rapidity distribution is sensitive to the  $u\bar{d}$  and  $d\bar{u}$  quark distributions. In addition the number of  $W^\pm$  events depends on the number of associated jets because the fraction of  $u$  and  $d$  quarks contributing to the different jet multiplicity processes changes. CMS measured the charge asymmetry defined as  $A_W = \frac{\sigma(W^+) - \sigma(W^-)}{\sigma(W^+) + \sigma(W^-)}$  for different numbers of associated jets [169]. Since many experimental systematic uncertainties especially the dominant uncertainties due to the jet energy scale cancel in this ratio, the charge asymmetry is a sensitive test even at large jet multiplicities. Figure 53 shows the charge asymmetry for  $W \rightarrow \mu\nu$  events. The MADGRAPH predictions agree well with the data, while PYTHIA fails to model the data even for one-jet events.

In order to place constraints on the PDFs, measurements of the  $W$  charge asymmetry as a function of the number of jets and as a function of the  $p_T$  of the  $W$  boson are needed. Such measurements at large values of the boson  $p_T$  could constrain the PDFs at larger momentum fractions  $x$  compared to inclusive measurements [176].

### 7.4 Measurements of the ratio of $W$ +jets to $Z$ +jets

Measurements of the  $W$  and  $Z$  cross-sections in association with jets are plagued by dominant uncertainties from the jet energy scale. Although both CMS and ATLAS have achieved excellent understanding of the jet energy scale, these uncertainties still dominate especially for jets at high rapidities. However, in other cases, such as the measurement of the jet  $p_T$  (Section 7.2), the experimental measurement is more precise than the theory predictions. Both the theory and experimental uncertainties can be reduced through a measurement of the cross-section ratio between  $W$ +jets and  $Z$ +jets processes. For example, when comparing ATLAS measurements of  $W$ +jets production to the ratio of  $W$ +jets to  $Z$ +jets production for events with one associated jet, the jet energy scale uncertainty is roughly a factor of two smaller in the ratio measurement.

CMS measured the ratio of  $W$ +jets to  $Z$ +jets for up to four associated jets [169]. In both the electron and muon channels, the data were in good agreement with the MADGRAPH and PYTHIA predictions. ATLAS measured the ratio for exactly one associated jet but for different thresholds of the jet  $p_T$  [177]. The combined results from the electron and muon channels are shown in Figures 54 and compared to predictions from PYTHIA, ALPGEN and NLO predictions from MCFM. The ratio, which is not constant as a function of the jet  $p_T$  threshold, decreases because at large jet momenta the difference in the boson masses is small compared to the effective scale of the interaction. All of the predictions model this trend well.

The measurement of the ratio of  $W$  to  $Z$  production in association with jets is one of the most precise measurements of perturbative QCD. Future measurements, using the full 2011 data set from the LHC will be able to measure this ratio for higher jet multiplicities and as a function of the  $p_T$  and rapidity of the jets and the  $H_T$ . This ratio is sensitive to new physics models, especially if the new particles decay preferentially either to the  $W$  vs. the  $Z$  final state.

### 7.5 Cross-section measurements of $W$ and $Z$ bosons in association with heavy-flavour quarks

The study of  $W$  and  $Z$  production in association with heavy-flavour quarks is of particular importance today. First, the theoretical predictions are less well known compared to the inclusive  $W$ +jets and  $Z$ +jets predictions. Second, precision measurements of these processes are critical since they are a dominant background in Higgs measurements of  $WH$  production with  $H \rightarrow b\bar{b}$  decays and new physics searches involving heavy-flavour production.

The production of  $W + b$ -jet events has two main diagrams at leading order (Figure 55):  $W$  plus a gluon in the final state where the gluon splits to a  $b\bar{b}$  pair, and  $b$ -quark in



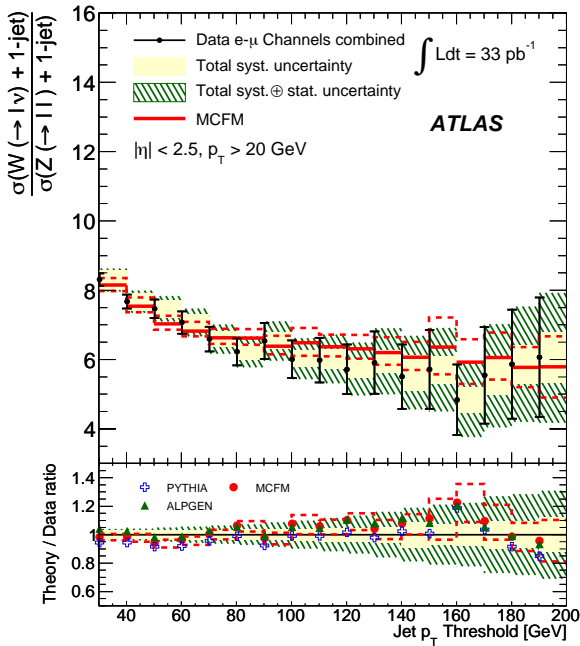


**Fig. 54** ATLAS [177]: Ratio of  $W$ +jets to  $Z$ +jets in  $N_{jet} = 1$  events for varying thresholds of the jet  $p_T$ . NLO predictions from MCFM and predictions from ALPGEN and PYTHIA are also shown.

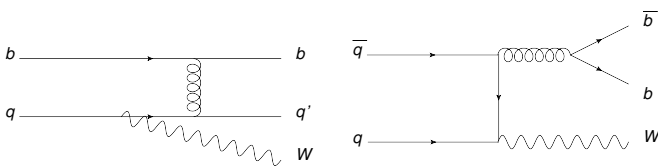


**Fig. 55** Leading-order Feynman diagram for the production of  $W$  bosons in association with a  $b$ -quark.

the initial state where the  $W$  is produced from radiation from a quark. The former can be produced both by the matrix-element calculation and by the parton showering model, whereas the latter diagram can only be modelled by including a  $b$ -quark in the initial state from the PDF.

The predictions and measurements of  $W + b$ -jet cross-section have a long history. The first measurements by CDF [21] indicated that the measured cross-section was too large by 2.8 standard deviations compared to the predictions. A measurement by ATLAS, using only an integrated luminosity of  $\int \mathcal{L} dt \approx 35 \text{ pb}^{-1}$ , also reported a larger cross-section by 1.5 standard deviations, while the D0 measurement was consistent with the predictions [24]. An updated ATLAS measurement [178] of the  $W + b$ -jet cross-section using an integrated luminosity of  $\int \mathcal{L} dt \approx 4.5 \text{ fb}^{-1}$  offers the statistical and systematic precision to definitively close this debate. The measurement presented cross-sections for the exclusive one-jet and two-jet final states with a fiducial phase space requirement of at least one  $b$ -jet, defined by the pres-

ence of a weakly decaying  $b$ -hadron with  $p_T > 5$  GeV and within a cone radius of  $\Delta R = 0.3$  of the jet axis. The cross-section results are summarised in Figure 56 and compared to calculations from MCFM, POWHEG and ALPGEN. The MCFM predictions are calculated using the 5-flavour scheme (5FNS) which accounts for the presence of  $b$ -quarks in the PDF. The ALPGEN and POWHEG predictions use the four-flavour scheme (4FNS). For one-jet events, the measured cross-section is consistent with 1.5 standard deviations to the NLO MCFM predictions, while for two-jet events the measured cross-section is in good agreement with the predictions. In the one-jet case, the difference between data and the predictions can be more clearly understood in the differential cross-section measurement as a function of the jet  $p_T$  shown in Figure 56. The MCFM and ALPGEN predict a softer jet  $p_T$  spectrum with respect to the data.

In a complementary result, the  $W + bb$  final state was measured by CMS [179], by requiring events with only two jets, both of which must originate from a  $b$ -hadron. The measured cross-section of

$$0.53 \pm 0.05(\text{stat}) \pm 0.09(\text{syst}) \pm 0.06(\text{th}) \pm 0.02(\text{lumi}) \text{ pb}$$

is in excellent agreement with the MCFM prediction of  $0.52 \pm 0.03 \text{ pb}$

Similar to measurements of  $W + b$ -jet, the  $Z + b$ -jet cross-section is much less studied compared to the inclusive  $Z$  measurements. Unlike  $W + b$ -jet which only has two main contributing diagrams at leading order,  $Z + b$ -jet production includes additional leading-order diagrams of  $Z$  radiation from an initial-state  $b$ -quark and  $Z$  radiation from a final-state  $b\bar{b}$  pair (Figure 57). Predictions which include diagrams with an initial-state  $b$  are therefore necessary. CMS presented a measurement of the  $Z + b$ -jet cross-section with exactly one  $b$ -jet, with at least one  $b$ -jet and with at least two  $b$ -jets, using an integrated luminosity of  $\int \mathcal{L} dt \approx 5 \text{ fb}^{-1}$  [180]. The results were compared to MADGRAPH, aMC@NLO and MCFM predictions. While the measured cross-sections were found to be in fair agreement with MADGRAPH and aMC@NLO, the MCFM results differ by approximately two standard deviations from the data. ATLAS also measured the  $Z + b$ -jet cross-section using a smaller data sample with an integrated luminosity of  $\int \mathcal{L} dt \approx 35 \text{ pb}^{-1}$  [181]. The NLO MCFM predictions as well as ALPGEN and SHERPA were found to be consistent with the data but there were signs of tension especially between the ALPGEN and SHERPA predictions themselves. These results are summarised in Figure 64. Updated results with better statistical precision and predictions with massive quark models are needed here to help resolve these differences.

In both  $W + b$ -jet and  $Z + b$ -jet production, diagrams with a gluon splitting to a  $b\bar{b}$  pair contribute to the matrix-element calculations and in the parton showering model. In a generator like ALPGEN, this overlap is removed by applying a  $\Delta R$  cut, so that at small values of  $\Delta R$  the gluon split-

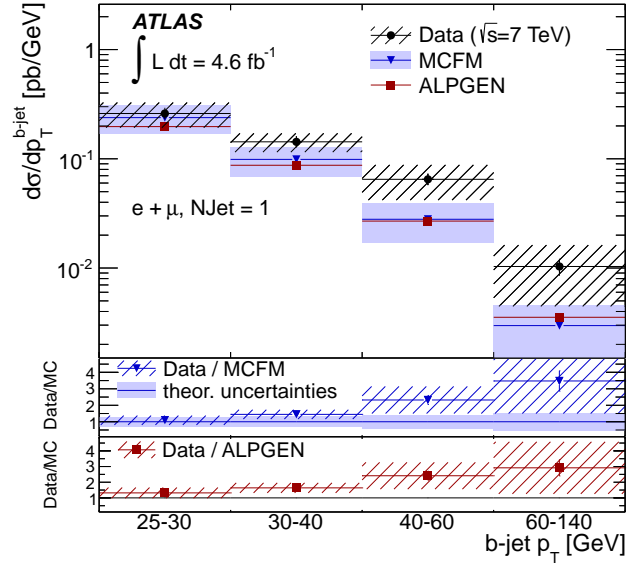
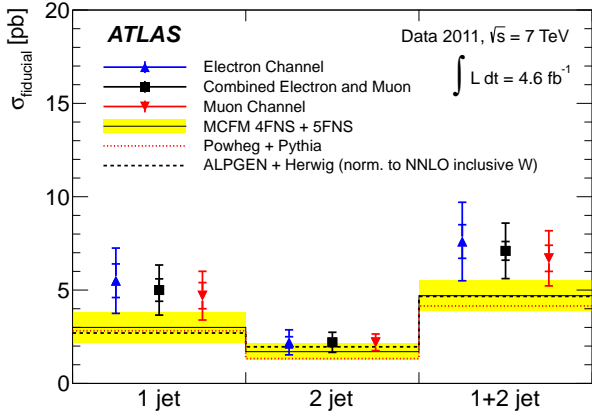


**Fig. 56** ATLAS [178]: Measurement of the cross-section for  $W + b$ -jet events for 1-jet, 2-jet, and 1+2-jet events (left). NLO MCFM predictions and ALPGEN and POWHEG predictions are also shown. Differential cross-section as a function of the  $b$ -jet  $p_T$  for 1-jet events (right). NLO MCFM predictions and ALPGEN predictions are also shown.

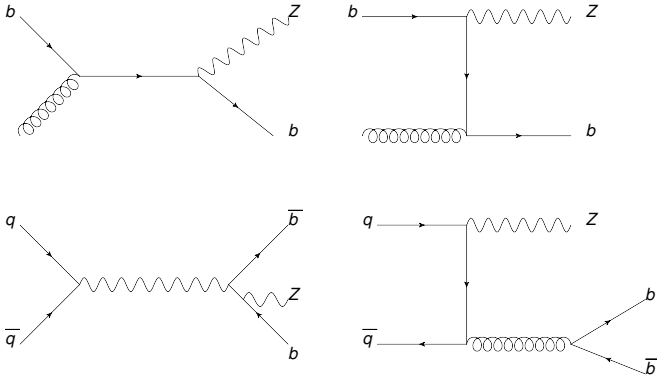


**Fig. 57** Leading-order Feynman diagrams for the production of  $Z$  bosons in association with a  $b$ -quark.

ting is handled by the parton shower, while at large values it is predicted from the matrix element. The theoretical uncertainties describing collinear  $b$ -quark production are large. To test this transition from parton shower to matrix-element calculations, measurements of the gluon splitting at small values of  $\Delta R$  is an important topic at the LHC today. This is especially important for new physics searches and Higgs measurements that select  $b$ -jets, since high  $p_T$   $b$ -jets tend to be produced via gluon splitting.

While measurements of gluon splitting at small values of  $\Delta R$  are interesting, it is experimentally challenging to measure since the two  $b$ -quarks are often reconstructed within the same jet. CMS presented a new approach for this measurement by measuring  $Z$  events with two  $b$ -hadrons [182]. As the  $b$ -hadrons can be reconstructed from displaced secondary vertices, only tracking information is needed and

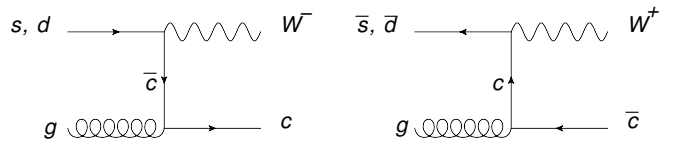


**Fig. 59** Leading-order Feynman diagrams for the production of the  $W$  boson in association with a  $c$ -quark.

there is no dependence on a jet algorithm. The angular resolution is  $\Delta R \approx 0.02$  between the two  $b$  hadrons. The differential cross-section measurement as a function of  $\Delta R$  of the two  $b$ -hadrons is shown in Figure 58. The collinear region ( $\Delta R < 0.5$ ) is best described by ALPGEN, while MADGRAPH and aMC@NLO predictions tend to underestimate the data. In addition, the differential cross-section was measured for a phase space region where  $p_T^Z > 50$  GeV (Figure 58). In this phase space, the relative fraction of events with collinear  $b$ -quarks increases. Again, ALPGEN gives the best description of the data.

The cross-section of the  $W$  boson in association with  $c$ -quarks, which have sensitivity to the  $s$ -quark contribution in PDFs, have not been experimentally well measured in the past. At the LHC, the dominant  $W+c$  production takes place via the reaction  $sg \rightarrow W^- + c$  and  $\bar{s}g \rightarrow W^+ + \bar{c}$ , as illustrated in Figure 59. Due to the high production rates at the LHC, measurements of the  $W + c$  cross-sections have for the first time, sufficient precision to constrain the  $s$ -quark in the PDFs at  $x \approx 0.01$ . In the future, measurements of  $W + c$  may also be able to help determine if there is a asymme-

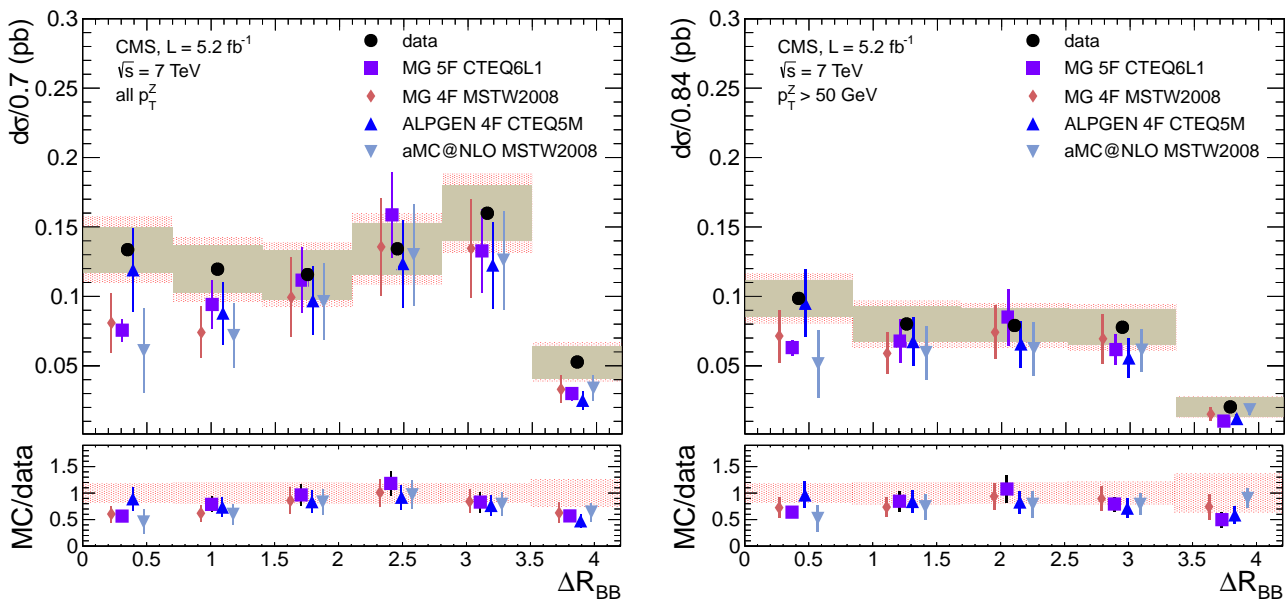


**Fig. 58** CMS [182]: Differential cross-section as a function of  $\Delta R$  of the two  $b$  hadrons for  $Z + b\bar{b}$  events. The right plot shows the inclusive phase space of  $p_T^Z > 0$  GeV. The left plot shows the phase space region of  $p_T^Z > 50$  GeV. Also shown are the predictions from MADGRAPH using the 5- and 4-flavour schemes, ALPGEN and MC@NLO.

try between the  $s$  and  $\bar{s}$  sea<sup>12</sup> as suggested by the NuTeV measurements [69, 183, 184]. Since the  $c$ -quark and the  $W$  have opposite charge, the  $W+c$  production can be measured by subtracting events with the same-sign charge from events with opposite-signed charge. This subtraction will have no effect on the  $W^- + c$  process, but all other background such as  $W^- + c\bar{c}$  and  $W^- + b\bar{b}$  are symmetric in same-sign and opposite-sign events and will be removed. In the CMS analysis [185], the jets originating from a  $c$ -quark are selected in one of three ways: a selection of a  $D^\pm \rightarrow K^\mp \pi^\pm \pi^\pm$  decay by requiring a displaced secondary vertex with three tracks and an invariant mass which is consistent with the  $D^\pm$ , a selection of a  $D^0 \rightarrow K^\mp \pi^\pm \pi^\pm$  decay by requiring a displaced secondary vertex with two tracks which is consistent with the  $D^0$ , and semileptonic  $c$ -quark decay by requiring a muon matched to a jet. The ATLAS analysis [186] selects  $W + c$  events by reconstructing the  $D^\pm \rightarrow K^\mp \pi^\pm \pi^\pm$  and  $D^{\pm\pm} \rightarrow D^0 \pi^\pm$  decay modes or by identifying jets with a semileptonic  $c$ -quark decay.

The ATLAS and CMS results both presented measurements of the  $W + c$  cross-sections, the cross-section ratio of  $W^+ + c$  to  $W^- + c$  as well as the cross-sections as a function of the lepton  $\eta$ . As summarised in Figure 60, the measured  $W + c$  cross-section in the ATLAS results is most consistent with PDF sets with a relatively higher  $s$ -quark density, while the CMS results are most consistent with PDF sets with a

relatively lower density. However, the precision of the measurements is not sufficient to make any definitive conclusions. Overall for both the ATLAS and CMS measurements, there is good agreement between the experimental results and the predictions.

In the ATLAS results, the ratio of the strange-to-down sea-quark distribution,  $r_s = 0.5(s + \bar{s})/\bar{d}$ , as a function of  $x$  is treated as free parameter in the HERAPDF1.5 PDF fits and all other eigenvectors in the fit are constrained within the uncertainties from the HERA data. As seen in Figure 61, the ATLAS results support the hypothesis of an SU(3)-symmetric light-quark sea and are consistent with the results from the ATLAS-epWZ12 PDF fits [144] where the ATLAS  $W$  and  $Z$  cross-section measurements are included in addition to the HERA data (see also Section 6.2).

In summary with the large LHC data sets, precision measurements of differential cross-sections of  $W$  and  $Z$  production in association with heavy-flavour quarks can be made for the first time. Measurements of the  $W + b$ -jet cross-sections have indicated that the jet  $p_T$  spectra is not well modelled by the predictions. In addition the predictions for the  $Z + b$ -jet cross-section are in tension both with the data and with each other. Future measurements of the differential cross-sections are needed to resolve this. Finally, both measurements of the  $W + c$ -jet production from ATLAS and CMS agree with a wide range of PDF sets. Although the ATLAS and CMS results tend to prefer PDFs with a different  $s$ -quark density, additional measurements with more data are needed to study this in greater detail.

<sup>12</sup>In practice this is challenging since the cross-section asymmetry in the ratio of  $W^+ + c$  to  $W^- + c$  production comes mainly from the  $d - \bar{d}$  PDF asymmetry.

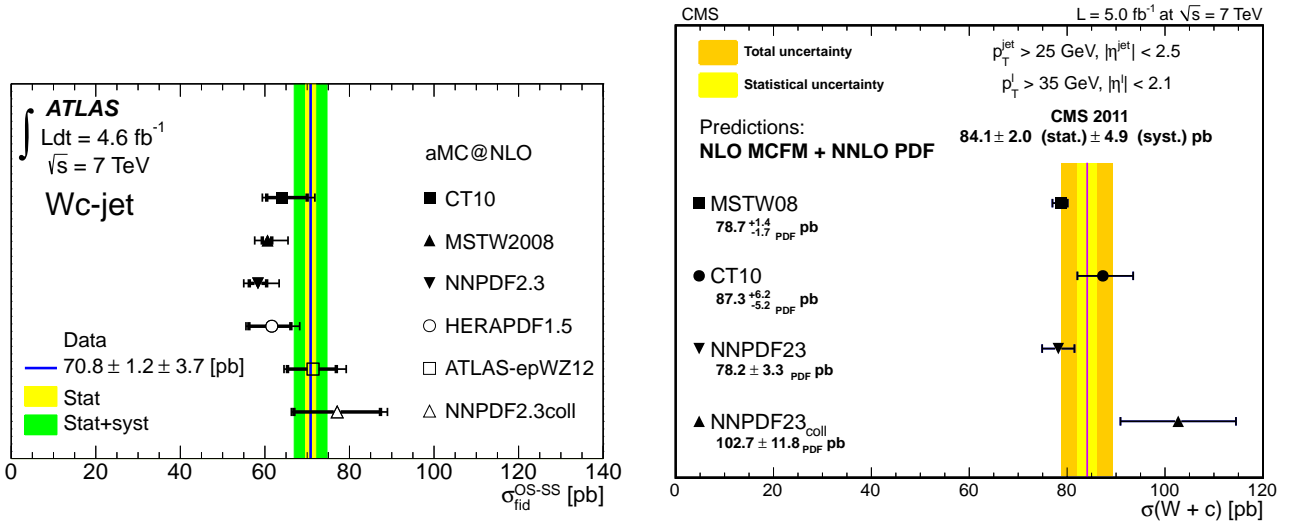


**Fig. 60** Cross-section of  $W + c$  for ATLAS [186] (left) and CMS [185] (right), compared to four different PDF sets: MSTW2008, CTEQ10, NNPDF23 and NNPDF23coll. The ATLAS results are also compared to HERAPDF1.5 and HERAPDF1.5 but including the ATLAS  $W$  and  $Z$  data, called ATLAS-EPWZ12. The NNPDF23coll PDF set is like NNPDF23 but excludes all fixed target data. In the ATLAS figure, "OS-SS" refers to the subtraction of events with opposite-signed charges and same-signed charges. The predictions in the ATLAS results are made using the aMC@NLO generator, while the predictions for the CMS results use the MCFM generator.

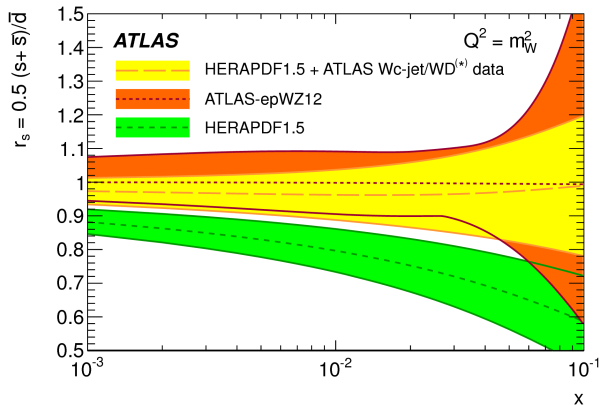


**Fig. 61** ATLAS [186]: Ratio of strange-to-down sea-quark distributions as a function of  $x$  as obtained from the ATLAS-epWZ12 PDF set, the ratio as assumed in the HERAPDF1.5 PDF set and the ratio obtained from the HERAPDF1.5 PDF set but including the ATLAS  $W + c$  measurements. The ATLAS-epWZ12 PDF set includes the ATLAS  $W$  and  $Z$  cross-section measurements in addition to the HERA data. The error band on the ratio including the ATLAS measurements represents the total uncertainty.

## 7.6 Electroweak production of $Z$ bosons

$Z$  bosons in associations with jets can be produced not only via the Drell-Yan process, but also via electroweak processes, as illustrated in Figure 62. Electroweak processes are here defined as all processes which lead to a final state of two leptons, two quarks and involve the exchange of electroweak bosons in the  $t$ -channel. Of special importance is the vector boson fusion process, shown in the first diagram, as it is an important input for Higgs boson studies and the study

of electroweak gauge couplings. In a full calculation of the production cross-section of process, which involves all diagrams, large negative interference exists between the pure vector boson fusion process, the bremsstrahlung and the non-resonant (or multi peripheral) processes.

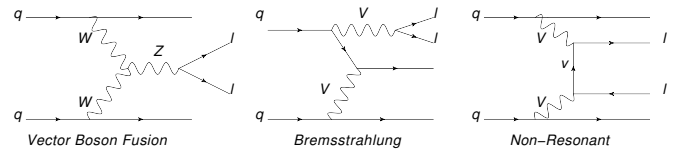


**Fig. 62** Three contribution Feynman diagrams for the electroweak production of an  $l^+ l^- q \bar{q}$  final state: Vector Boson Fusion (left), Bremsstrahlung (middle), non-resonant production (left)

The experimental signature of the electroweak production described above, is the typical  $Z$  boson topology of two oppositely charged leptons close to the  $Z$  boson mass and in addition two high energetic jets. As the momentum transfer to the interacting initial partons caused by the electroweak bosons in the  $t$ -channel is relatively small, these jets tend to be produced in the forward region of the detector. The dominant background is due to Drell-Yan production of the  $Z$  boson in association with jets. Significantly smaller background contributions are expected from the top-pair production and di-boson processes such as  $WW$ ,  $WZ$  and  $ZZ$ .

The CMS experiment has analysed the full 2011 data set to measure the cross-section of the electroweak production of  $Z$  bosons [187]. In addition to a standard  $Z$  boson selection in the electron and muon decay channels, further cuts on two reconstructed jets within  $|\eta| < 3.6$  are imposed

in order to reject the Drell-Yan background: The transverse momenta of the two jets are required to be  $p_T > 65$  GeV and  $p_T > 40$  GeV, respectively. In addition, the Z boson rapidity in the rest frame of the two jets has to fulfil  $|y^*| < 1.2$ . These requirements lead to a signal efficiency of 0.06 and to a signal over background ratio of  $S/B \approx 0.1$ . This low  $S/B$  ratio requires the usage of maximum likelihood fits or multivariate techniques for the cross-section determination. Both approaches have been used in [187]. The distribution of the invariant mass of both jets is shown in Figure 63 for the signal-and-background processes. It is the basis of a likelihood fit based on Poisson statistics where the normalisation of the background distributions and the signal distributions are kept as free parameters. The signal extraction via multivariate techniques uses a boosted decision tree approach, which is based on kinematic variables of the jets and leptons and their combinations. Both approaches lead to consistent results, where the multivariate approach provides lower uncertainties. The final measured cross-section within a fiducial phase space<sup>13</sup> is

$$\sigma_{EW,Z}^{meas.} = 154 \pm 24(stat) \pm 46(syst) \pm 26(th) \pm 3(lumi) \text{ fb}$$

and is in good agreement with the theoretical expectation of  $\sigma_{EW,Z} = 166\text{fb}$ . The dominating uncertainties are due to the modelling of the background distributions and the jet energy scale. A possible electroweak Z production can therefore be observed with a  $2.6\sigma$  significance already within the 2011 data set. The ATLAS experiment has also published a measurement with improved systematic uncertainties based on the 2012 data set at  $\sqrt{s} = 8$  TeV [188] which confirms the observation of the electroweak production of Z above a  $5\sigma$  confidence level. Measurements at a higher center-of-mass energy and even larger data samples than the  $\sqrt{s} = 8$  TeV sample will be needed to establish this cross-section measurement with higher precision.

## 8 Summary and Outlook

In the first two years of the LHC physics program, a new energy regime was investigated with high precision; in some measurements, the experimental systematic uncertainties are at the percent level and the statistical uncertainties are even smaller. A similar precision was reached at previous colliders usually after many years of running. Not only the highest available collision energies and large luminosities provided by the LHC, but also the remarkable performance of the two general purpose detectors, ATLAS and CMS, are the basis of this success.

This article is the first comprehensive review of all major results regarding the production of single heavy gauge bosons at a collision energy of  $\sqrt{s} = 7$  TeV. Summaries,

<sup>13</sup>defined by  $m_{ll} > 50$  GeV,  $p_{T,jet} > 25$  GeV,  $|\eta_{jet}| < 4.0$ ,  $m_{jj} > 120$  GeV

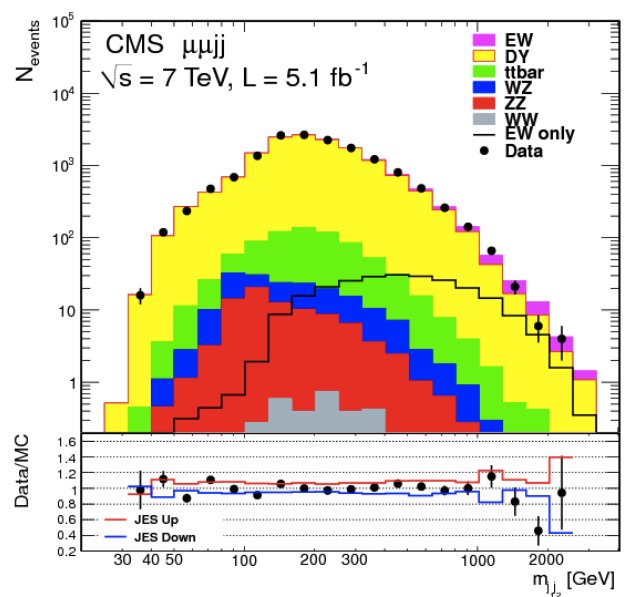


**Fig. 63** CMS [187]: The  $m_{jj}$  distribution after selection cuts. The expected contributions from the dominant Drell-Yan (labeled DY) background and the electroweak (labeled EW) signal processes are evaluated from a fit, while the contributions from the small  $t\bar{t}$  and di-boson backgrounds are estimated from simulation. The solid line with the label "EW only" shows the distribution for the signal alone.

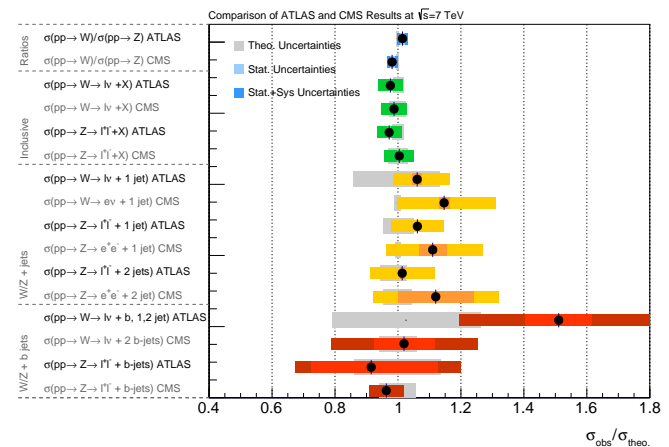


**Fig. 64** Summary of cross-sections for inclusive W and Z production and with associated jets. Shown is the ratio between data and predictions. The grey bands represent the theory uncertainties, the light coloured bands the statistical uncertainties and the dark coloured bands the combined statistical and systematic uncertainties. Note that the CMS W+jets and Z+jets results are compared to SHERPA predictions here.

comparisons and interpretations of the available results have been presented. All results are in agreement between the two main experiments at the LHC and are furthermore consistent with the presently available Standard Model predictions. This is illustrated in Figure 64, where the ratio between theoretical predictions and measured observables for both experiments are shown.

Among the numerous measurements which have been presented in this review article, a few should be emphasised.

The inclusive production cross-sections of  $W$  and  $Z$  bosons were among the first measurements of the LHC which made use of the full detector potential and built the basis for many subsequent physics analyses. By now, the experimental precision of the fully inclusive cross-sections of both experiments is below 2% and hence comparable to the NNLO QCD prediction uncertainties. The differential cross-section measurement led to an improved understanding of the proton structure functions. In particular, the strange-quark content appears to be comparable to the  $\bar{u}$  and  $\bar{d}$ -quark content even at low scales, i.e. before the QCD evolution.

Using the large data sets available from the LHC, our understanding of  $W$  and  $Z$  production in association with heavy-flavour jets, in particular, has greatly improved. Recent measurements of the  $W + b$ -jet cross-section, which indicate that generators such as MCFM and ALPGEN predict a jet  $p_T$  spectrum that is too soft compared to the data, are the first steps in resolving a long debate over the source of the disagreement between the measured and predicted cross-section. Measurements of  $W + c$  production have for the first time the precision to constrain the  $s$ -quark in the PDFs at  $x \approx 0.01$  and can help determine if there is an asymmetry between the  $s$  and  $\bar{s}$  sea.

With the proton-proton data recorded in the year 2012 at a center-of-mass energy of  $\sqrt{s} = 8$  TeV, the available statistics increased by a factor of four, corresponding to an integrated luminosity of  $\int \mathcal{L} dt \approx 20 - 25 \text{fb}^{-1}$ . While the increase in center-of-mass energy has only a mild effect on the expected cross-section,<sup>14</sup> the increased data sample allows for calibration of the detector to a higher precision. This opens the possibility for the precision measurement of electroweak observables such as the  $W$  boson mass. In addition, the measurements of multi-differential cross-sections and rare processes such as  $W$  and  $Z$  production in association with heavy flavour quarks will become available.

The next significant step forward will be the LHC run in the years 2015 to 2018 at a center-of-mass energy of  $\sqrt{s} = 13 - 14$  TeV. With this, the Standard Model predictions will once again be tested in a new energy regime with the ultimate hope to find signs of ‘new physics’.

## Acknowledgements

It is our privilege to participate as members of the ATLAS collaboration in the endeavour to investigate the new energy regime opened by the LHC and to present the work of a collaborative effort of both the ATLAS and CMS experiments. We thank Alessandro Tricoli for lively discussions over this text and Lutz Koepke and Joey Houston for the detailed feedback on the first drafts of this review article. In addition, we thank the ATLAS and CMS working group conveners, Sasha Glazov, Alessandro Tricoli, Jeffrey Berryhill and Maxime Gouzevitch for their input. Special thanks goes to Voica Radescu and Elzbieta Richter-Was, who helped us in the prospects of PDF Fits and the implementation of the studies regarding the QCD angular coefficients, respectively. Last, but not least, we would like to express our gratitude to Dieter Haidt for his guidance and comments during the writing of this review article. The contribution by Matthias Schott was supported by the Volkswagen Foundation and the German Research Foundation (DFG). The contribution by Monica Dunford was supported by the Bundesministerium für Bildung und Forschung (BMBF).

## References

1. UA1 Collaboration. Experimental Observation of Isolated Large Transverse Energy Electrons with Associated Missing Energy at  $\sqrt{s} = 540\text{-GeV}$ . *Phys.Lett.*, B122:103–116, 1983.
2. UA1 Collaboration. Experimental Observation of Lepton Pairs of Invariant Mass Around  $95\text{-GeV}/c^2$  at the CERN SPS Collider. *Phys.Lett.*, B126:398–410, 1983.
3. UA2 Collaboration. Observation of Single Isolated Electrons of High Transverse Momentum in Events with Missing Transverse Energy at the CERN anti-p p Collider. *Phys.Lett.*, B122:476–485, 1983.
4. UA2 Collaboration. Evidence for  $Z^0$  to  $e^+e^-$  at the CERN anti-p p Collider. *Phys.Lett.*, B129:130–140, 1983.
5. ALEPH Collaboration, DELPHI Collaboration, L3 Collaboration, OPAL Collaborations. LEP  $W$  branching fraction results for the PDG Review of Particle Physics. 2005.
6. ALEPH Collaboration, DELPHI Collaboration, L3 Collaboration, OPAL Collaborations. A Combination of Results on Charged Triple Gauge Boson Couplings by the LEP Experiments. 2005.
7. CDF Collaboration. A measurement of  $W$  boson production in  $1.8$  TeV  $\bar{p}p$  collisions. *Phys.Rev.Lett.*, 62:1005, 1989.

<sup>14</sup>The Standard Model production cross-sections for  $W$  and  $Z$  bosons are expected to increase by roughly 20%.

8. CDF Collaboration. Measurements of inclusive W and Z cross sections in p anti-p collisions at  $\sqrt{s} = 1.96$ -TeV. *J.Phys.*, G34:2457–2544, 2007.
9. D0 Collaboration. Measurement of W and Z boson production cross sections. *Phys.Rev.*, D60:052003, 1999.
10. D0 Collaboration. Measurement of the shape of the boson transverse momentum distribution in  $p\bar{p} \rightarrow Z/\gamma^* \rightarrow e^+e^- + X$  events produced at  $\sqrt{s} = 1.96$ -TeV. *Phys.Rev.Lett.*, 100:102002, 2008.
11. CDF Collaboration. Transverse momentum cross section of  $e^+e^-$  pairs in the Z-boson region from  $p\bar{p}$  collisions at  $\sqrt{s} = 1.96$  TeV. *Phys.Rev.*, D86:052010, 2012.
12. CDF Collaboration. Precise measurement of the W-boson mass with the CDF II detector. *Phys.Rev.Lett.*, 108:151803, 2012.
13. D0 Collaboration. Measurement of the W Boson Mass with the D0 Detector. *Phys.Rev.Lett.*, 108:151804, 2012.
14. CDF Collaboration. Measurement of jet multiplicity in W events produced in  $p\bar{p}$  collisions at  $\sqrt{s} = 1.8$ -TeV. *Phys.Rev.Lett.*, 70:4042–4046, 1993.
15. CDF Collaboration. Measurement of inclusive jet cross-sections in  $Z/\gamma^*(\rightarrow e^+e^-) + \text{jets}$  production in  $p\bar{p}$  collisions at  $\sqrt{s} = 1.96$ -TeV. *Phys.Rev.Lett.*, 100:102001, 2008.
16. CDF Collaboration. Measurement of the cross section for  $W^-$  boson production in association with jets in  $p\bar{p}$  collisions at  $\sqrt{s} = 1.96$ -TeV. *Phys.Rev.*, D77:011108, 2008.
17. D0 Collaboration. Studies of W boson plus jets production in  $p\bar{p}$  collisions at  $\sqrt{s} = 1.96$  TeV. *Phys.Rev.*, D88:092001, 2013.
18. D0 Collaboration. Measurements of inclusive W+jets production rates as a function of jet transverse momentum in  $p\bar{p}$  collisions at  $\sqrt{s} = 1.96$  TeV. *Phys.Lett.*, B705:200–207, 2011.
19. D0 Collaboration. Measurement of the ratios of the  $Z/\gamma^* + \geq n$  jet production cross sections to the total inclusive  $Z/\gamma^*$  cross section in p anti-p collisions at  $\sqrt{s} = 1.96$ -TeV. *Phys.Lett.*, B658:112–119, 2008.
20. CDF Collaboration. Observation of the Production of a W Boson in Association with a Single Charm Quark. *Phys.Rev.Lett.*, 110(7):071801, 2013.
21. CDF Collaboration. First Measurement of the b-jet Cross Section in Events with a W Boson in p anti-p Collisions at  $\sqrt{s} = 1.96$ -TeV. *Phys.Rev.Lett.*, 104:131801, 2010.
22. CDF Collaboration. Measurement of Cross Sections for b Jet Production in Events with a Z Boson in  $p^-$  anti-p Collisions at  $\sqrt{s} = 1.96$ -TeV. *Phys.Rev.*, D79:052008, 2009.
23. D0 Collaboration. Measurement of the ratio of the  $p\bar{p} \rightarrow W^+c^-$  jet cross section to the inclusive  $p\bar{p} \rightarrow W + \text{jets}$  cross section. *Phys.Lett.*, B666:23–30, 2008.
24. D0 Collaboration. Measurement of the  $p\bar{p} \rightarrow W + b + X$  production cross section at  $\sqrt{s} = 1.96$  TeV. *Phys.Lett.*, B718:1314–1320, 2013.
25. D0 Collaboration. Measurement of the ratio of differential cross sections  $\sigma(p\bar{p} \rightarrow Z + b \text{ jet})/\sigma(p\bar{p} \rightarrow Z + \text{jet})$  in  $p\bar{p}$  collisions at  $\sqrt{s} = 1.96$  TeV. *Phys.Rev.*, D87(9):092010, 2013.
26. STAR Collaboration. Measurement of the  $W \rightarrow e\nu$  and  $Z/\gamma^* \rightarrow e^+e^-$  Production Cross Sections at Mid-rapidity in Proton-Proton Collisions at  $\sqrt{s} = 500$  GeV. *Phys.Rev.*, D85:092010, 2012.
27. PHENIX Collaboration. Cross Section and Parity Violating Spin Asymmetries of  $W^\pm$  Boson Production in Polarized  $p + p$  Collisions at  $\sqrt{s} = 500$  GeV. *Phys.Rev.Lett.*, 106:062001, 2011.
28. CMS Collaboration. Study of W boson production in PbPb and  $pp$  collisions at  $\sqrt{s_{NN}} = 2.76$  TeV. *Phys.Lett.*, B715:66–87, 2012.
29. CMS Collaboration. Study of Z boson production in PbPb collisions at nucleon-nucleon centre of mass energy = 2.76 TeV. *Phys.Rev.Lett.*, 106:212301, 2011.
30. ATLAS Collaboration. Measurement of Z boson Production in Pb+Pb Collisions at  $\sqrt{s_{NN}} = 2.76$  TeV with the ATLAS Detector. *Phys.Rev.Lett.*, 110:022301, 2013.
31. J.R. Ellis, J. Gillies, M. Jacob, D.E. Plane, and D. Treille. CERN: The second 25 years. *Phys.Rept.*, 403-404:1–504, 2004.
32. G. Altarelli and L. Di Lella. PHYSICS OF THE INTERMEDIATE VECTOR BOSONS. *Adv.Ser.Direct.High Energy Phys.*, 4:177–224, 1989.
33. CDF Collaboration. Determination of the jet energy scale at the collider detector at Fermilab. *Nucl.Instrum.Meth.*, A566:375–412, 2006.
34. ATLAS Collaboration. Measurement of dijet cross sections in pp collisions at 7 TeV centre-of-mass energy using the ATLAS detector. *arXiv.1312.3524*, 2013.
35. J. Beringer et al. Review of Particle Physics (RPP). *Phys.Rev.*, D86:010001, 2012.
36. M. Kobayashi and T. Maskawa. CP Violation in the Renormalizable Theory of Weak Interaction. *Prog.Theor.Phys.*, 49:652–657, 1973.
37. T. Nunnemann. Vector bosons in new phenomena searches. *LMU Munich*, 2007.
38. A. Buckley, J. Butterworth, S. Gieseke, D. Grellscheid, S. Hoche, et al. General-purpose event generators for LHC physics. *Phys.Rept.*, 504:145–233, 2011.
39. T. Carli, D. Clements, A. Cooper-Sarkar, C. Gwenlan, G.P. Salam, et al. A posteriori inclusion of par-

- ton density functions in NLO QCD final-state calculations at hadron colliders: The APPLGRID Project. *Eur.Phys.J.*, C66:503–524, 2010.
40. T. Schorner-Sadenius. Jet physics in electron-proton scattering. *Eur.Phys.J.*, C72:2060, 2012.
  41. J.D. Bjorken and E.A. Paschos. Inelastic Electron Proton and gamma Proton Scattering, and the Structure of the Nucleon. *Phys.Rev.*, 185:1975–1982, 1969.
  42. J.C. Collins, D. Soper, and G.F. Sterman. Factorization for Short Distance Hadron - Hadron Scattering. *Nucl.Phys.*, B261:104, 1985.
  43. CDF Collaboration. Measurement of the  $Z$   $p_T$  distribution in  $\bar{p}p$  collisions at  $\sqrt{s} = 1.8$  TeV. *Phys.Rev.Lett.*, 67:2937–2941, 1991.
  44. CDF Collaboration. Measurement of the  $W$   $P(T)$  distribution in  $\bar{p}p$  collisions at  $\sqrt{s} = 1.8$  TeV. *Phys.Rev.Lett.*, 66:2951–2955, 1991.
  45. D0 Collaboration. Measurement of the shape of the transverse momentum distribution of  $W$  bosons produced in  $p\bar{p}$  collisions at  $\sqrt{s} = 1.8$  TeV. *Phys.Rev.Lett.*, 80:5498–5503, 1998.
  46. D0 Collaboration. Differential production cross section of  $Z$  bosons as a function of transverse momentum at  $\sqrt{s} = 1.8$  TeV. *Phys.Rev.Lett.*, 84:2792–2797, 2000.
  47. R.K. Ellis, W.J. Stirling, and B.R. Webber. QCD and collider physics. *Camb.Monogr.Part.Phys.Nucl.Phys.Cosmol.*, 8:1–435, 1996.
  48. E. Gerwick, T. Plehn, S. Schumann, and P. Schichtel. Scaling Patterns for QCD Jets. *JHEP*, 1210:162, 2012.
  49. M.L. Mangano, M. Moretti, F. Piccinini, R. Pittau, and A.D. Polosa. ALPGEN, a generator for hard multiparton processes in hadronic collisions. *JHEP*, 0307:001, 2003.
  50. F. Caravaglios, M.L. Mangano, M. Moretti, and R. Pittau. A New approach to multijet calculations in hadron collisions. *Nucl.Phys.*, B539:215–232, 1999.
  51. R. Hamberg, W.L. van Neerven, and T. Matsuura. A Complete calculation of the order  $\alpha - s^2$  correction to the Drell-Yan  $K$  factor. *Nucl.Phys.*, B359:343–405, 1991.
  52. W.L. van Neerven and E.B. Zijlstra. The  $O(\alpha - s^2)$  corrected Drell-Yan  $K$  factor in the DIS and MS scheme. *Nucl.Phys.*, B382:11–62, 1992.
  53. C. Anastasiou, L.J. Dixon, K. Melnikov, and F. Petriello. High precision QCD at hadron colliders: Electroweak gauge boson rapidity distributions at NNLO. *Phys.Rev.*, D69:094008, 2004.
  54. E. Laenen, J. Smith, and W.L. van Neerven. All order resummation of soft gluon contributions to heavy quark production in hadron hadron collisions. *Nucl.Phys.*, B369:543–599, 1992.
  55. U. Baur, O. Brein, W. Hollik, C. Schappacher, and D. Wackerth. Electroweak radiative corrections to neutral current Drell-Yan processes at hadron colliders. *Phys.Rev.*, D65:033007, 2002.
  56. G. Balossini, G. Montagna, C.M. Carloni Calame, M. Moretti, M. Treccani, et al. Electroweak QCD corrections to Drell Yan processes. *Acta Phys.Polon.*, B39:1675, 2008.
  57. A.B. Arbuzov, M. Awramik, M. Czakon, A. Freitas, M.W. Grunewald, et al. ZFITTER: A Semi-analytical program for fermion pair production in  $e^+e^-$  annihilation, from version 6.21 to version 6.42. *Comput.Phys.Commun.*, 174:728–758, 2006.
  58. D.Y. Bardin, P. Christova, M. Jack, L. Kalinovskaya, A. Olchevski, et al. ZFITTER v.6.21: A Semianalytical program for fermion pair production in  $e^+e^-$  annihilation. *Comput.Phys.Commun.*, 133:229–395, 2001.
  59. A.A. Akhundov, D.Y. Bardin, and T. Riemann. Electroweak One Loop Corrections to the Decay of the Neutral Vector Boson. *Nucl.Phys.*, B276:1, 1986.
  60. D.Y. Bardin, S. Riemann, and T. Riemann. Electroweak One Loop Corrections to the Decay of the Charged Vector Boson. *Z.Phys.*, C32:121–125, 1986.
  61. G. Degrossi, F. Feruglio, A. Vicini, S. Fanchiotti, and P. Gambino. Two loop corrections for electroweak processes. *arXiv*, hep-ph/9507286, 1995.
  62. S. Brensing, S. Dittmaier, M. Kramer, and A. Muck. Radiative corrections to  $W^-$  boson hadroproduction: Higher-order electroweak and supersymmetric effects. *Phys.Rev.*, D77:073006, 2008.
  63. Richard D. Ball et al. Parton distributions with QED corrections. *Nucl.Phys.*, B877:290–320, 2013.
  64. V.N. Gribov and L.N. Lipatov. Deep inelastic  $e p$  scattering in perturbation theory. *Sov.J.Nucl.Phys.*, 15:438–450, 1972.
  65. Y.L. Dokshitzer. Calculation of the Structure Functions for Deep Inelastic Scattering and  $e^+e^-$  Annihilation by Perturbation Theory in Quantum Chromodynamics. *Sov.Phys.JETP*, 46:641–653, 1977.
  66. G. Altarelli and G. Parisi. Asymptotic Freedom in Parton Language. *Nucl.Phys.*, B126:298, 1977.
  67. V.V. Sudakov. Vertex parts at very high-energies in quantum electrodynamics. *Sov.Phys.JETP*, 3:65–71, 1956.
  68. P.M. Nadolsky, H. Lai, Q. Cao, J. Huston, J. Pumplin, et al. Implications of CTEQ global analysis for collider observables. *Phys.Rev.*, D78:013004, 2008.
  69. A.D. Martin, W.J. Stirling, R.S. Thorne, and G. Watt. Parton distributions for the LHC. *Eur.Phys.J.*, C63:189–285, 2009.
  70. S. Alekhin, J. Blumlein, S. Klein, and S. Moch. The 3, 4, and 5-flavor NNLO Parton from Deep-Inelastic-Scattering Data and at Hadron Colliders. *Phys.Rev.*,



- D81:014032, 2010.
71. M. Gluck, P. Jimenez-Delgado, and E. Reya. Dynamical parton distributions of the nucleon and very small- $x$  physics. *Eur.Phys.J.*, C53:355–366, 2008.
  72. R.D. Ball, V. Bertone, L. Del Debbio, S. Forte, A. Guffanti, et al. Precision NNLO determination of  $\alpha_s(M_Z)$  using an unbiased global parton set. *Phys.Lett.*, B707:66–71, 2012.
  73. A.M. Cooper-Sarkar. PDF Fits at HERA. *PoS, EPS-HEP2011:320*, 2011.
  74. J. Pumplin, D. Stump, R. Brock, D. Casey, J. Huston, et al. Uncertainties of predictions from parton distribution functions. 2. The Hessian method. *Phys.Rev.*, D65:014013, 2001.
  75. T. Sjostrand and M. van Zijl. A Multiple Interaction Model for the Event Structure in Hadron Collisions. *Phys.Rev.*, D36:2019, 1987.
  76. R.D. Field and R.P. Feynman. A Parametrization of the Properties of Quark Jets. *Nucl.Phys.*, B136:1, 1978.
  77. B. Andersson, G. Gustafson, G. Ingelman, and T. Sjostrand. Parton Fragmentation and String Dynamics. *Phys.Rept.*, 97:31–145, 1983.
  78. R.D. Field and S. Wolfram. A QCD Model for  $e^+e^-$  Annihilation. *Nucl.Phys.*, B213:65, 1983.
  79. B.R. Webber. A QCD Model for Jet Fragmentation Including Soft Gluon Interference. *Nucl.Phys.*, B238:492, 1984.
  80. D. Amati and G. Veneziano. Preconfinement as a Property of Perturbative QCD. *Phys.Lett.*, B83:87, 1979.
  81. D.J. Lange. The EvtGen particle decay simulation package. *Nucl.Instrum.Meth.*, A462:152–155, 2001.
  82. S. Jadach, Z. Was, R. Decker, and J.H. Kuhn. The tau decay library TAUOLA: Version 2.4. *Comput.Phys.Commun.*, 76:361–380, 1993.
  83. P. Bartalini and L. Fano. Multiple partonic interactions at the LHC. Proceedings, 1st International Workshop, MPI’08, Perugia, Italy, October 27-31, 2008. *Proc.*, 2010.
  84. ATLAS Collaboration. Measurement of hard double-parton interactions in  $W(\rightarrow l\nu)+2$  jet events at  $\sqrt{s}=7$  TeV with the ATLAS detector. *New J.Phys.*, 15:033038, 2013.
  85. T. Sjostrand, S. Mrenna, and P.Z. Skands. PYTHIA 6.4 Physics and Manual. *JHEP*, 0605:026, 2006.
  86. T. Sjostrand, S. Mrenna, and P.Z. Skands. A Brief Introduction to PYTHIA 8.1. *Comput.Phys.Commun.*, 178:852–867, 2008.
  87. G. Corcella, I.G. Knowles, G. Marchesini, S. Moretti, K. Odagiri, et al. HERWIG 6: An Event generator for hadron emission reactions with interfering gluons (including supersymmetric processes). *JHEP*, 0101:010, 2001.
  88. M. Bahr, S. Gieseke, M.A. Gigg, D. Grellscheid, K. Hamilton, et al. Herwig++ Physics and Manual. *Eur.Phys.J.*, C58:639–707, 2008.
  89. T. Gleisberg, S. Hoeche, F. Krauss, M. Schonherr, S. Schumann, et al. Event generation with SHERPA 1.1. *JHEP*, 0902:007, 2009.
  90. J.M. Butterworth, J.R. Forshaw, and M.H. Seymour. Multiparton interactions in photoproduction at HERA. *Z.Phys.*, C72:637–646, 1996.
  91. J. Alwall, M. Herquet, F. Maltoni, O. Mattelaer, and T. Stelzer. MadGraph 5 : Going Beyond. *JHEP*, 1106:128, 2011.
  92. S. Catani, F. Krauss, R. Kuhn, and B.R. Webber. QCD matrix elements + parton showers. *JHEP*, 0111:063, 2001.
  93. F. Krauss. Matrix elements and parton showers in hadronic interactions. *JHEP*, 0208:015, 2002.
  94. M.L. Mangano, M. Moretti, and R. Pittau. Multijet matrix elements and shower evolution in hadronic collisions:  $Wb\bar{b} + n$  jets as a case study. *Nucl.Phys.*, B632:343–362, 2002.
  95. S. Frixione and B.R. Webber. Matching NLO QCD computations and parton shower simulations. *JHEP*, 0206:029, 2002.
  96. S. Frixione, P. Nason, and C. Oleari. Matching NLO QCD computations with Parton Shower simulations: the POWHEG method. *JHEP*, 0711:070, 2007.
  97. S. Alioli, P. Nason, C. Oleari, and E. Re. A general framework for implementing NLO calculations in shower Monte Carlo programs: the POWHEG BOX. *JHEP*, 1006:043, 2010.
  98. J.M. Campbell, R. K. Ellis, and D.L. Rainwater. Next-to-leading order QCD predictions for  $W + 2$  jet and  $Z + 2$  jet production at the CERN LHC. *Phys.Rev.*, D68:094021, 2003.
  99. C.F. Berger, Z. Bern, L.J. Dixon, F. Febres Cordero, D. Forde, et al. An Automated Implementation of On-Shell Methods for One-Loop Amplitudes. *Phys.Rev.*, D78:036003, 2008.
  100. R. Gavin, Y. Li, F. Petriello, and S. Quackenbush. FEWZ 2.0: A code for hadronic  $Z$  production at next-to-next-to-leading order. *Comput.Phys.Commun.*, 182:2388–2403, 2011.
  101. C. Balazs and C.P. Yuan. Soft gluon effects on lepton pairs at hadron colliders. *Phys.Rev.*, D56:5558–5583, 1997.
  102. J.C. Collins and D. Soper. Angular Distribution of Dileptons in High-Energy Hadron Collisions. *Phys.Rev.*, D16:2219, 1977.
  103. E. Mirkes and J. Ohnemus.  $W$  and  $Z$  polarization effects in hadronic collisions. *Phys.Rev.*, D50:5692–5703, 1994.

104. E. Mirkes and J. Ohnemus. Angular distributions of Drell-Yan lepton pairs at the Tevatron: Order  $\alpha - s^2$  corrections and Monte Carlo studies. *Phys.Rev.*, D51:4891–4904, 1995.
105. E. Mirkes. Angular decay distribution of leptons from W bosons at NLO in hadronic collisions. *Nucl.Phys.*, B387:3–85, 1992.
106. C.S. Lam and W. Tung. A Parton Model Relation Sans QCD Modifications in Lepton Pair Productions. *Phys.Rev.*, D21:2712, 1980.
107. M. Chaichian, M. Hayashi, and K. Yamagishi. Angular Distributions of High Mass Dileptons With Finite Transverse Momentum in High-energy Hadronic Collisions. *Phys.Rev.*, D25:130, 1982.
108. J. Lindfors. Angular Distribution of Large  $q$ -transverse Muon Pairs in Different Reference Frames. *Phys.Scripta*, 20:19–22, 1979.
109. C.S. Lam and W. Tung. Structure Function Relations at Large Transverse Momenta in Lepton Pair Production Processes. *Phys.Lett.*, B80:228, 1979.
110. L. Evans and P. Bryant. LHC Machine. *JINST*, 3:S08001, 2008.
111. ATLAS Collaboration. The ATLAS Experiment at the CERN Large Hadron Collider. *JINST*, 3:S08003, 2008.
112. CMS Collaboration. The CMS experiment at the CERN LHC. *JINST*, 3:S08004, 2008.
113. LHCb Collaboration. The LHCb Detector at the LHC. *JINST*, 3:S08005, 2008.
114. ALICE Collaboration. The ALICE experiment at the CERN LHC. *JINST*, 3:S08002, 2008.
115. D. Fournier. Performance of the LHC, ATLAS and CMS in 2011. *EPJ Web Conf.*, 28:01003, 2012.
116. S. van der Meer. Calibration of the effective beamheight in the ISR. *CERN CDS*, CERN-ISR-PO-68-31, 1968.
117. C. Rubbia. Measurement of the luminosity of pp collider with a (generalized) van der Meer method. *Eur.Phys.J.*, CERN-pp-Note-38, 1977.
118. ATLAS Collaboration. Performance of the ATLAS Trigger System in 2010. *Eur.Phys.J.*, C72:1849, 2012.
119. ATLAS Collaboration. Electron performance measurements with the ATLAS detector using the 2010 LHC proton-proton collision data. *Eur.Phys.J.*, C72:1909, 2012.
120. CMS Collaboration. Energy calibration and resolution of the CMS electromagnetic calorimeter in pp collisions at  $\sqrt{s} = 7$  TeV. *JINST*, 8:P09009, 2013.
121. CMS Collaboration. Performance of CMS muon reconstruction in  $pp$  collision events at  $\sqrt{s} = 7$  TeV. *JINST*, 7:P10002, 2012.
122. ATLAS Collaboration. Preliminary results on the muon reconstruction efficiency, momentum resolution, and momentum scale in ATLAS 2012 pp collision data. *ATLAS CONF Note*, ATLAS-CONF-2013-088, 2013.
123. S. Catani, Y.L. Dokshitzer, M.H. Seymour, and B.R. Webber. Longitudinally invariant  $K_T$  clustering algorithms for hadron hadron collisions. *Nucl.Phys.*, B406:187–224, 1993.
124. ATLAS Collaboration. Jet energy measurement with the ATLAS detector in proton-proton collisions at  $\sqrt{s} = 7$  TeV. *Eur.Phys.J.*, C73:2304, 2013.
125. CMS Collaboration. Particle-Flow Event Reconstruction in CMS and Performance for Jets, Taus, and MET. *CMS Analysis Summary*, CMS-PAS-PFT-09-001, 2009.
126. CMS Collaboration. Determination of Jet Energy Calibration and Transverse Momentum Resolution in CMS. *JINST*, 6:P11002, 2011.
127. CMS Collaboration. Identification of b-quark jets with the CMS experiment. *JINST*, 8:P04013, 2013.
128. CMS Collaboration. CMS Preliminary Electron Performance Results. *TWIKI-Site*, 2013.
129. S. Agostinelli et al. GEANT4: A Simulation toolkit. *Nucl.Instrum.Meth.*, A506:250–303, 2003.
130. G. D’Agostini. A Multidimensional unfolding method based on Bayes’ theorem. *Nucl.Instrum.Meth.*, A362:487–498, 1995.
131. A. Hocker and V. Kartvelishvili. SVD approach to data unfolding. *Nucl.Instrum.Meth.*, A372:469–481, 1996.
132. ATLAS Collaboration. Measurement of the inclusive  $W^\pm$  and  $Z/\gamma$  cross sections in the electron and muon decay channels in  $pp$  collisions at  $\sqrt{s} = 7$  TeV with the ATLAS detector. *Phys.Rev.*, D85:072004, 2012.
133. CMS Collaboration. Measurement of the Inclusive W and Z Production Cross Sections in  $pp$  Collisions at  $\sqrt{s} = 7$  TeV. *JHEP*, 1110:132, 2011.
134. L. Vacavant and I. Hinchliffe. Signals of models with large extra dimensions in ATLAS. *J.Phys.*, G27:1839–1850, 2001.
135. A. Leike. The Phenomenology of extra neutral gauge bosons. *Phys.Rept.*, 317:143–250, 1999.
136. J.R. Espinosa, C. Grojean, and M. Muhlleitner. Composite Higgs Search at the LHC. *JHEP*, 1005:065, 2010.
137. CMS Collaboration. Measurement of inclusive W and Z boson production cross sections in pp collisions at  $\sqrt{s} = 8$  TeV. *arXiv*, hep-ex/1402.0923, 2014.
138. ATLAS Collaboration. Measurement of the high-mass Drell-Yan differential cross-section in pp collisions at  $\sqrt{s} = 7$  TeV with the ATLAS detector. *Phys.Lett.*, B725:223–242, 2013.
139. CMS Collaboration. Measurement of the differential and double-differential Drell-Yan cross sections

- in proton-proton collisions at  $\sqrt{s} = 7$  TeV. *JHEP*, 1312:030, 2013.
140. CMS Collaboration. Measurement of the electron charge asymmetry in inclusive  $W$  production in  $pp$  collisions at  $\sqrt{s} = 7$  TeV. *Phys.Rev.Lett.*, 109:111806, 2012.
  141. CMS Collaboration. Muon charge asymmetry in inclusive  $W$  production at  $\sqrt{s} = 7$  TeV. *CMS Analysis Summary*, CMS-PAS-SMP-12-021, 2012.
  142. R.D. Ball, S. Carrazza, L. Del Debbio, S. Forte, J. Gao, et al. Parton Distribution Benchmarking with LHC Data. *JHEP*, 1304:125, 2013.
  143. HERAFitter. <http://projects.hepforge.org/hera>. 2013.
  144. ATLAS Collaboration. Determination of the strange quark density of the proton from ATLAS measurements of the  $W \rightarrow \ell\nu$  and  $Z \rightarrow \ell\ell$  cross sections. *Phys.Rev.Lett.*, 109:012001, 2012.
  145. LHCb Collaboration. Inclusive  $W$  and  $Z$  production in the forward region at  $\sqrt{s} = 7$  TeV. *JHEP*, 1206:058, 2012.
  146. R.D. Ball, V. Bertone, S. Carrazza, C.S. Deans, L. Del Debbio, et al. Parton distributions with LHC data. *Nucl.Phys.*, B867:244–289, 2013.
  147. CMS Collaboration. Measurement of the Rapidity and Transverse Momentum Distributions of  $Z$  Bosons in  $pp$  Collisions at  $\sqrt{s} = 7$  TeV. *Phys.Rev.*, D85:032002, 2012.
  148. ATLAS Collaboration. Measurement of the transverse momentum distribution of  $Z/\gamma^*$  bosons in proton-proton collisions at  $\sqrt{s} = 7$  TeV with the ATLAS detector. *Phys.Lett.*, B705:415–434, 2011.
  149. A. Banfi, S. Redford, M. Vesterinen, P. Waller, and T.R. Wyatt. Optimisation of variables for studying dilepton transverse momentum distributions at hadron colliders. *Eur.Phys.J.*, C71:1600, 2011.
  150. ATLAS Collaboration. Measurement of angular correlations in Drell-Yan lepton pairs to probe  $Z/\gamma^*$  boson transverse momentum at  $\sqrt{s}=7$  TeV with the ATLAS detector. *Phys.Lett.*, B720:32–51, 2013.
  151. ATLAS Collaboration. Measurement of the Transverse Momentum Distribution of  $W$  Bosons in  $pp$  Collisions at  $\sqrt{s} = 7$  TeV with the ATLAS Detector. *Phys.Rev.*, D85:012005, 2012.
  152. CMS Collaboration. Measurement of the transverse momentum distributions of  $Z$  Bosons decaying to dimuons in  $pp$  collisions at  $\sqrt{s}=8$  TeV. *CMS Analysis Summary*, CMS-PAS-SMP-12-025, 2013.
  153. S. Alekhin, J. Blumlein, P. Jimenez-Delgado, S. Moch, and E. Reya. NNLO Benchmarks for Gauge and Higgs Boson Production at TeV Hadron Colliders. *Phys.Lett.*, B697:127–135, 2011.
  154. P. Renton. Updated SM calculations of  $\sigma_W / \sigma_Z$  at the Tevatron and the  $W$  boson width. *arXiv*, hep-ph/0804.4779, 2008.
  155. S. Schael et al. Precision electroweak measurements on the  $Z$  resonance. *Phys.Rept.*, 427:257–454, 2006.
  156. D. Haidt and A. Pullia. The weak neutral current - discovery and impact. *Riv.Nuovo Cim.*, 036(08):335–395, 2013.
  157. ATLAS Collaboration. Measurement of the forward-backward asymmetry of  $Z/\gamma$  bosons decaying into electron and muon pairs with the ATLAS detector at  $\sqrt{s}=7$  TeV. *ATLAS CONF Note*, ATLAS-CONF-2013-043, 2013.
  158. C.M. Carloni Calame, G. Montagna, O. Nicrosini, and M. Treccani. Higher order QED corrections to  $W$  boson mass determination at hadron colliders. *Phys.Rev.*, D69:037301, 2004.
  159. CMS Collaboration. Forward-backward asymmetry of Drell-Yan lepton pairs in  $pp$  collisions at  $\sqrt{s} = 7$  TeV. *Phys.Lett.*, B718:752–772, 2013.
  160. CMS Collaboration. Measurement of the weak mixing angle with the Drell-Yan process in proton-proton collisions at the LHC. *Phys.Rev.*, D84:112002, 2011.
  161. ATLAS Collaboration. Measurement of the polarisation of  $W$  bosons produced with large transverse momentum in  $pp$  collisions at  $\sqrt{s} = 7$  TeV with the ATLAS experiment. *Eur.Phys.J.*, C72:2001, 2012.
  162. CMS Collaboration. Measurement of the Polarization of  $W$  Bosons with Large Transverse Momenta in  $W$ +Jets Events at the LHC. *Phys.Rev.Lett.*, 107:021802, 2011.
  163. D0 Collaboration. Measurements of differential cross sections of  $Z/\gamma^*+\text{jets}+X$  events in proton anti-proton collisions at  $\sqrt{s} = 1.96$ -TeV. *Phys.Lett.*, B678:45–54, 2009.
  164. D0 Collaboration. Measurement of  $Z/\gamma^*+\text{jet}+X$  angular distributions in  $p$  anti- $p$  collisions at  $\sqrt{s} = 1.96$ -TeV. *Phys.Lett.*, B682:370–380, 2010.
  165. G.P. Salam. Towards Jetography. *Eur.Phys.J.*, C67:637–686, 2010.
  166. ATLAS Collaboration. Measurement of the production cross section of jets in association with a  $Z$  boson in  $pp$  collisions at  $\sqrt{s} = 7$  TeV with the ATLAS detector. *JHEP*, 1307:032, 2013.
  167. CMS Collaboration. Jet multiplicity and differential production cross sections of  $Z$ +jets events in proton-proton collisions at 7 TeV. *CMS Analysis Summary*, CMS-PAS-12-017, 2014.
  168. C. Englert, T. Plehn, P. Schichtel, and S. Schumann. Establishing Jet Scaling Patterns with a Photon. *JHEP*, 1202:030, 2012.
  169. CMS Collaboration. Jet Production Rates in Association with  $W$  and  $Z$  Bosons in  $pp$  Collisions at  $\sqrt{s} = 7$  TeV. *JHEP*, 1201:010, 2012.

- 
170. ATLAS Collaboration. Study of jets produced in association with a  $W$  boson in  $pp$  collisions at  $\sqrt{s} = 7$  TeV with the ATLAS detector. *Phys.Rev.*, D85:092002, 2012.
171. CMS Collaboration. Measurement of the Differential Cross Section of  $W$ -Bosons Produced in Association with Jets in  $pp$  collisions at 7 TeV. *CMS Analysis Summary*, CMS-PAS-12-023, 2014.
172. A. Denner, S. Dittmaier, T. Kasprzik, and A. Muck. Electroweak corrections to dilepton + jet production at hadron colliders. *JHEP*, 1106:069, 2011.
173. CMS Collaboration. Rapidity distributions in exclusive  $Z$  + jet and  $\gamma$  + jet events in  $pp$  collisions at  $\sqrt{s}=7$  TeV. *Phys.Rev.*, D88:112009, 2013.
174. CMS Collaboration. Event shapes and azimuthal correlations in  $Z$  + jets events in  $pp$  collisions at  $\sqrt{s} = 7$  TeV. *Phys.Lett.*, B722:238–261, 2013.
175. ATLAS Collaboration. Measurement of  $k_T$  splitting scales in  $W(\rightarrow l\nu)$  events at  $\sqrt{s}=7$  TeV with the ATLAS detector. *Eur.Phys.J.*, C73:2432, 2013.
176. S.A. Malik and G. Watt. Ratios of  $W$  and  $Z$  cross sections at large boson  $p_T$  as a constraint on PDFs and background to new physics. *JHEP*, 1402:025, 2014.
177. ATLAS Collaboration. A measurement of the ratio of the  $W$  and  $Z$  cross sections with exactly one associated jet in  $pp$  collisions at  $\sqrt{s} = 7$  TeV with ATLAS. *Phys.Lett.*, B708:221–240, 2012.
178. ATLAS Collaboration. Measurement of the cross-section for  $W$  boson production in association with  $b$ -jets in  $pp$  collisions at  $\sqrt{s} = 7$  TeV with the ATLAS detector. *JHEP*, 1306:084, 2013.
179. CMS Collaboration. Measurement of the production cross section for a  $W$  boson and two  $b$  jets in  $pp$  collisions at  $\sqrt{s} = 7$  TeV. *arXiv*, hep-ex/1312.6608, 2013.
180. CMS Collaboration. Measurement of the production cross sections for a  $Z$  boson and one or more  $b$  jets in  $pp$  collisions at  $\sqrt{s} = 7$  TeV. *arXiv*, hep-ex/1402.1521, 2014.
181. ATLAS Collaboration. Measurement of the cross-section for  $b^-$  jets produced in association with a  $Z$  boson at  $\sqrt{s} = 7$  TeV with the ATLAS detector. *Phys.Lett.*, B706:295–313, 2012.
182. CMS Collaboration. Measurement of the cross section and angular correlations for associated production of a  $Z$  boson with  $b$  hadrons in  $pp$  collisions at  $\sqrt{s} = 7$  TeV. *JHEP*, 1312:039, 2013.
183. M. Goncharov et al. Precise measurement of dimuon production cross-sections in muon neutrino Fe and muon anti-neutrino Fe deep inelastic scattering at the Tevatron. *Phys.Rev.*, D64:112006, 2001.
184. R.D. Ball et al. Precision determination of electroweak parameters and the strange content of the proton from neutrino deep-inelastic scattering. *Nucl.Phys.*, B823:195–233, 2009.
185. CMS Collaboration. Measurement of associated  $W$  + charm production in  $pp$  collisions at  $\sqrt{s} = 7$  TeV. *JHEP*, 1402:013, 2014.
186. ATLAS Collaboration. Measurement of the production of a  $W$  boson in association with a charm quark in  $pp$  collisions at  $\sqrt{s}=7$  TeV with the ATLAS detector. 2014.
187. CMS Collaboration. Measurement of the hadronic activity in events with a  $Z$  and two jets and extraction of the cross section for the electroweak production of a  $Z$  with two jets in  $pp$  collisions at  $\sqrt{s} = 7$  TeV. *JHEP*, 1310:101, 2013.
188. ATLAS Collaboration. Measurement of the electroweak production of dijets in association with a  $Z$ -boson and distributions sensitive to vector boson fusion in proton-proton collisions at  $\sqrt{s} = 8$  TeV using the ATLAS detector. *JHEP*, 2014(4):1–56, 2014.